FINAL REPORT

Predictive Chemical and Statistical Modeling of Particulate Matter Formation in Turbulent Combustion with Application to Aircraft Engines

SERDP Project WP-1574

MARCH 2012

Heinz Pitsch
Stanford University

SERDP
DOD · EPA · DOE

REPORT DOCUMENTATION PAGE

Form Approved
OMB No. 0704–0188

1. REPORT DATE (DD–MM–YYYY)	2. REPORT TYPE	3. DATES COVERED (From — To)
07–03–2012	Final	Jul 2007 – Jan 2012

4. TITLE AND SUBTITLE

Predictive Chemical and Statistical Modeling of Particulate Matter Formation in Turbulent Combustion with Application to Aircraft Engines

5a. CONTRACT NUMBER

W912HQ-07-C-0044

5b. GRANT NUMBER

5c. PROGRAM ELEMENT NUMBER

6. AUTHOR(S)

Pitsch, Heinz
Frenklach, Michael
Raman, Venkat

5d. PROJECT NUMBER

1574

5e. TASK NUMBER

5f. WORK UNIT NUMBER

7. PERFORMING ORGANIZATION NAME(S) AND ADDRESS(ES)
Heinz Pitsch
Dept. of Mechanical Engineering, MC 3035
488 Escondido Mall
Stanford University
Stanford, CA 94305

8. PERFORMING ORGANIZATION REPORT NUMBER

9. SPONSORING / MONITORING AGENCY NAME(S) AND ADDRESS(ES)

Strategic Environmental Research and Development Program
901 North Stuart Street, Suite 303
Arlington, VA 22203

10. SPONSOR/MONITOR'S ACRONYM(S)

SERDP

11. SPONSOR/MONITOR'S REPORT NUMBER(S)

12. DISTRIBUTION / AVAILABILITY STATEMENT

Approved for public release; distribution is unlimited

13. SUPPLEMENTARY NOTES

14. ABSTRACT
Soot formation in gas turbine engines is a major concern in the design of modern aircraft propulsion systems. Accurate modeling of soot formation is extremely difficult due to the complex underlying chemical and physical processes. A set of critical modeling requirements for soot prediction were identified and investigated under a comprehensive program covering three different research areas–chemical modeling, statistical modeling, and soot modeling in turbulent combustion. The chemical modeling aspect of the project includes further improvements of the gas-phase kinetics and the heterogeneous reactions on the particle surface leading to further soot mass growth or oxidation. In this project, we developed a new method for statistical modeling of the particle size distribution based on particle volume and surface area. The chemical and statistical methods were incorporated into turbulent combustion models for large-eddy simulation. In addition, the complex interactions of molecular and turbulent transport with the flame chemistry and particle formation and oxidation was studied in direct numerical simulations.

15. SUBJECT TERMS

Soot, Oxidation, Large Eddy Simulation, Direct Numerical Simulation, Hybrid Method of Moments, Extended Flamelet/Progress Variable Model

16. SECURITY CLASSIFICATION OF:			17. LIMITATION OF ABSTRACT	18. NUMBER OF PAGES	19a. NAME OF RESPONSIBLE PERSON
a. REPORT	b. ABSTRACT	c. THIS PAGE			Colleen Kaul
U	U	U	UU	96	19b. TELEPHONE NUMBER (include area code) (815)354-1536

Standard Form 298 (Rev. 8–98)
Prescribed by ANSI Std. Z39.18

Contents

List of Figures

List of Tables

List of Acronyms

DFT Density Functional Theory

DNS Direct Numerical Simulation

DQMOM Direct Quadrature Method of Moments

FPV Flamelet/Progress Variable

GGA Generalized Gradient Approximation

HACA Hydrogen Abstraction/Carbon Addition

HMOM Hybrid Method of Moments

HOMA Harmonic Oscillator Model of Aromaticity

IEM Interaction by Exchange with the Mean

KMC Kinetic Monte Carlo

LDA Laser Doppler Anemometry

LEM Linear Eddy Model

LES Large Eddy Simulation

LIF Laser Induced Fluorescence

LII Laser Induced Incandescence

MC Monte Carlo

MOMIC Method of Moments with Interpolative Closure

MPI Message Passing Interface

NDF Number Density Function

PAH Polycyclic Aromatic Hydrocarbon

PBE Population Balance Equation

PDF Probability Density Function

QMOM Quadrature Method of Moments

RANS Reynolds-averaged Navier Stokes

RFPV Radiation Flamelet/Progressive Variable

RMS Root Mean Square

RQL Rich-Quench-Lean

RRKM RiceRamspergerKasselMarcus

SM Sectional Method

ZPE Zero Point Energies

Acknowledgments

Abstract

Objectives Soot formation in aircraft engines is of great concern due to the health and environmental impacts of soot. The design of aircraft propulsion systems would greatly benefit from a computational methodology that can accurately predict soot emissions. This project has sought to develop these simulation capabilities in the framework of large eddy simulation (LES). The complexity of the soot formation process and its strong interactions with gas-phase combustion chemistry and turbulence necessitated a comprehensive approach involving three key research areas: chemical modeling of soot surface reactions, especially oxidation, statistical modeling of soot particle distributions, and soot modeling in LES of turbulent combustion.

Technical Approach Soot growth and oxidation processes were investigated using theoretical approaches applicable to large reaction systems. The work focused on the thermodynamics and kinetics of aromatic oxyradicals, the key intermediates in oxidation of soot.

A novel moment method called the hybrid method of moments (HMOM) was developed for predicting moments of the soot particle number density function. This formulation described soot particle size using both volume and surface area and is able to account for bimodal distributions of soot particles sizes.

An integrated LES model for soot evolution in turbulent nonpremixed flames was developed. The model components include a soot model based on HMOM, an extended flamelet/progress variable gas-phase combustion model, and a model to account for the slow chemistry of soot precursors. The development of these modeling approaches was aided by the results of a first-of-its-kind direct numerical simulation (DNS) study of soot nucleation and growth using a polycyclic aromatic hydrocarbon (PAH) based model for soot inception.

Results The principal conclusion of the soot oxidation study is that only the outer rings of aromatic oxyradicals are able to undergo oxidation, whereas the inner rings resist oxidation in combustion environments. We also found that the variability of both thermodynamic stability and decomposition rate of aromatic oxyradicals can be explained and correlated with substrate aromaticity. These findings will support the development of practical rules for predicting oxidation rate coefficients for aromatics, thereby enhancing models of soot oxidation.

The LES soot model was validated in a laboratory scale natural gas jet diffusion flame. Compared to experimental measurements, the LES provided a reasonable prediction of the maximum soot volume fraction. Factors extrinsic to the soot model formulation were found to be major sources of error and uncertainty in soot prediction. These factors include modeling of small scale gas-phase mixing rates and specification of the kinetic mechanism for PAH formation and growth.

Benefits The overall outcome of this project is a significant advancement in the sophistication of soot modeling approaches for LES. Using these approaches, the superiority of LES to Reynolds-averaged Navier Stokes (RANS) methods for soot modeling was demonstrated. The LES model permits the effects of turbulence and gas-phase chemistry on soot formation to be assessed qualitatively. Sources of error in soot prediction were clearly identified, allowing future modeling studies to be targeted to these areas.

1 Objectives

Soot formation in aircraft engines is a major concern for all aircraft engine manufacturers. While current emission requirements are based only on smoke visibility, quantitative requirements on soot emissions from aircraft engines will be established soon due to the many negative impacts of soot on human health and the environment. These regulations will not only stipulate the total soot emission levels but other soot characteristics as well. For instance, it has been realized that small particles are much more carcinogenic than larger particles indicating that the size distribution is a critical factor. Soot particles also act as condensation nuclei for ice crystals forming cirrus clouds, which influence the earth's climate through radiative forcing effects. The cloud nucleation rate is linked to both the number of soot particles and their structure. From these examples, it is evident that future regulations will specify detailed characteristics of permissible soot emissions including both the allowable size distribution and particle number density.

Novel techniques, such as lean direct injection, have been proposed to reduce soot emissions from aircraft engines. Although it is known that such techniques might reduce the soot volume fraction, little is known about the effect on particle size distribution and the particle number density.

Accurate modeling of soot formation is very difficult due to the complex underlying chemical and physical processes, including a large sequence of gas phase reactions forming polycyclic aromatic hydrocarbons (PAH) followed by particle inception, particle/particle interactions, condensation of PAH on the particle surface, and soot particle growth and oxidation by heterogeneous reaction with different gas phase species. In turbulent flows, moreover, we have shown in the past that the very subtle interaction of turbulent transport and molecular differential diffusion effects can strongly influence predicted soot concentrations. Although the effects of turbulence are very important for the evolution of particulates, limited prior work has been done in this area. Several empirical or semi-empirical models for soot formation have been proposed in the past, but they are far from being predictive. The development of more predictive models for soot emissions and soot particle size distribution will enable the computational optimization of present engine designs and the development of new low-emissions combustion concepts.

The major objective of this project has been the formulation of a comprehensive simulation methodology to enable accurate and detailed prediction of soot formation in aircraft engines, especially military-type aircraft engines. These simulation methods will provide a valuable tool for engineering design and the enable the development of strategies to mitigate soot formation.

Large eddy simulation (LES) is the most advanced approach available for simulating turbulent reacting fluid flows of the scale and complexity of the flow with in an aircraft combustor. Three main issues were identified in the development of predictively accurate LES soot modeling capabilities.

First, the soot particle population evolves under the effects of several complex physical and chemical processes, including particle nucleation, particle growth through particle-particle collisions and surface reactions, and particle erosion through oxidative reactions. While the underlying phenomena of the nucleation and growth processes are comparatively well established, soot oxidation process are less completely understood. Fundamental chem-

ical modeling studies of soot oxidation were carried out under the project. The results of these studies can be used to create simplified representations of the oxidation process for inclusion in LES computations.

Second, a statistical description of the soot population must be developed. Mathematically, this description is available in the form of the soot particle number density function (NDF). However, the NDF must be approximated for compatibility with the LES numerical discretization. Moment methods are commonly used to approximate such density functions. Due to the characteristically bimodal distribution of soot particle sizes, special care is required in applying moment methods to the soot NDF to ensure that the resulting statistical description is numerically robust and physically accurate. A novel moment method was developed under the program to meet these requirements.

Third, the small scale interactions of soot, turbulence, and gas-phase chemistry are unresolved in LES and must be modeled. It must be recognized that soot formation inside turbulent aircraft combustors is a highly intermittent and unsteady process. In practical combustor designs such as the rich-quench-lean (RQL) operating mode, soot is generated in fuel-rich high temperature regions and is subsequently oxidized after dilution with air. The amount of soot actually emitted is the result of the differences between these generation and oxidation processes. More importantly, the generation and oxidation processes occur with very high intermittency, indicating that the temporal history of soot precursors, turbulence-related strain, and combustion processes are critical in determining emission levels. All of these processes are highly complex and interact nonlinearly. Therefore, accurate modeling of unresolved soot/flame/turbulence interaction is essential to achieving quantitative predictions of soot formation. Under this project, new modeling methods for capturing these interactions were developed and validated.

Under the project, significant advances were made in each of the three areas of (i) chemical modeling, (ii) statistical modeling , and (iii) simulation and modeling of soot/flame/turbulence interaction. The remainder of this Report is organized as follows: Section 2 provides the relevant background information and characterizes the outstanding issues for accurate simulation of soot formation. Section 3 describes the computational methods used to investigate these issues and reports on the new models developed. Section 4 discusses the results of the simulations performed and discusses the significance of their findings. Finally, Section 5 summarizes the achievements of the research and indicates areas for ongoing work.

2 Background

In this section, we will first provide an overview of the present understanding of soot formation and evolution in relation to our own work in this field.

2.1 Oxidation of Soot

Chemical evolution of graphene edges is one of the key processes in the formation, growth, and oxidation of soot and its aromatic precursors [4–6]. Assuming that the soot particle surface is comprised of molecular aromatic sites (i.e., graphene edges) and invoking chemical similarity, it was postulated that soot surface reactions can be thought of as chemically analogous reactions of polycyclic aromatic hydrocarbons (PAHs) [7, 8]. Growth reactions, those increasing PAH size by reactions with gaseous species, primarily acetylene, received immediate and continuing attention (see, e.g., [4–6] and references therein). However, it was also recognized that the chemical analogy was not sufficient to describe reactions taking place at the surface and steric effects, neighboring sites, and substrate size must also be considered [9]. The latter realization increased substantially the number of possible elementary reactions; for instance, the latest detailed graphene-edge growth mechanism is composed of 42 elementary reactions [10].

The oxidation of PAHs and soot surfaces has received lesser attention. The initial detailed models of soot oxidation invoked two principal steps: an elementary reaction of a surface radical with O_2 and an atomistically-unresolved attack of OH on a generic surface site [8, 11]. Both reactions were assumed to remove one C atom per O atom of the gaseous reactant and both assumed to form a "pristine" surface site ($C_{surface}$–H or $C_{surface}$–) as the substrate product of oxidation. The former reaction was modeled following the postulate of chemical similarity by phenyl + O_2. The oxidation by OH was described using the collision efficiency determined in flame studies [12]. This oxidation model has been widely adopted in modeling studies, recently with different values of the rate coefficients [13].

Considering the knowledge gained with growth reactions, where the reaction chemistry of larger aromatic edges turned out to be much richer than that of the analogous small aromatic species, there is clearly a need for similar exploration of possible pathways for oxidation. This was set to be the objective of the present work. We began this process with the examination of the thermodynamic stability of the key intermediates, graphene-edge oxyradicals, located at both zigzag and armchair sites, and then proceeded with the kinetics of graphene oxyradical decomposition.

2.2 Statistical Soot Modeling

Modeling of the statistics of the soot particle population is critical for the accurate description of soot evolution and prediction of the particle size distribution in the exhaust of an engine. Two prominent characteristics of typical soot particle populations must be considered to develop an appropriate statistical description of the soot number density function (NDF). First, the size distribution of soot particles is frequently observed to be bimodal in experimental studies [14, 15]. The first mode consists of small particles formed by persistent nucleation from PAH, and the second mode consists of larger particles which have grown by

collision and surface reactions. Second, while particles in the first mode are overwhelmingly spherical in form, the shape of particles in the second mode is highly variable, including both spherical particles [14, 15] and fractal aggregates [16], which are particles composed of many small spheres called primary particles. These complexities in shape generally require the NDF to be parametrized by multiple quantities such as volume and surface area [17–19] to obtain an accurate description of the particle population.

The evolution of this complex bimodal NDF is governed by the Population Balance Equation (PBE). However, the high dimensionality of the PBE (including spatial, temporal, and two or more particle size coordinates) makes its direction solution intractable. Therefore, alternative methods are used to obtain an approximate description of the soot particle population. The available methods can be divided into two classes: those that solve for an approximate form of the NDF and those that solve for a set of mean quantities.

There are two basic methods for solving for an approximate form of the NDF. The most accurate statistical modeling method is Monte Carlo (MC) simulation. In these simulations, stochastic processes govern the evolution of a representative population. The benefit of MC simulations is a very accurate prediction of the complete NDF. However, this accuracy comes at a cost, and the application of MC simulations is limited to simple configurations such as homogeneous reactors and one-dimensional laminar premixed flames. A second approach is to use a sectional method (SM). For these methods, the NDF is discretized in bins. An equation for the number of particles in the bin is solved for each bin. Like MC simulations, accurate predictions of the complete (discretized) NDF can be obtained but at significant computational cost since many bins are required for each NDF coordinate to obtain good accuracy. Unlike MC simulations, sectional methods are deterministic and can be explicitly coupled to gas-phase chemistry.

The second approach to the statistical modeling of soot is generally described as one of several moment methods. In these methods, equations are solved that yield information about mean quantities rather than the NDF itself. Moment methods are superior in terms of computational cost compared to SM and MC simulations, but complete information about the population is lost. An additional shortcoming is that the equations for the moments are unclosed. Moments that are not directly solved for are required to compute the source terms for the moments that are solved for, thus requiring further modeling. At the outset of the project two options in moment methods, each with a different closure model, were available: the Method of Moments with Interpolative Closure (MOMIC) [20, 21] and the Direct Quadrature Method of Moments (DQMOM) [17].

In MOMIC [20, 21], the equations for the moments are closed by logarithmic polynomial interpolation. The widely used simplified version of MOMIC, which interpolates based on positive moments only, was found to be unable to represent the bimodal nature of the soot NDF under some conditions[18]. However, more comprehensive formulations of MOMIC [20], based on positive and negative moments, should offer better accuracy in these circumstances [21].

In the original Quadrature Method of Moments (QMOM) [22], the NDF is approximated by a series of delta functions, and the moments are approximated by Gauss quadrature. DQMOM [17] is the generalization of QMOM to multivariate distributions. In DQMOM, transport equations are solved directly for the weights and locations of the delta functions. The inherent multi-modality of DQMOM is well suited to capturing the persistent nucleation

mode [18]. However, in order to obtain the source terms for the transport equations for the weights and locations of the delta functions from the source terms of the moment transport equations, a linear system must be inverted. Depending on the shape of the NDF at any given point and the choice of moments solved for, this inversion may be ill-conditioned.

In light of these findings, a new moment method was developed in this project. The Hybrid Method of Moments (HMOM) [23] combines the inherent multi-modality of DQMOM with the numerical ease of MOMIC. HMOM uses the approach of DQMOM for the first mode (small spherical particles) and the approach of MOMIC for the second mode (large fractal aggregates) in order to capture the influence of the persistent nucleation mode. Details of the formulation of HMOM are provided in Sec. 3.2.1. HMOM has been successfully used to predict soot formation in a variety of laminar and turbulent, premixed and nonpremixed flames in LES and DNS [23–25].

2.3 Simulation and Modeling of Soot/Flame/Turbulence Interaction

The small-scale interactions between turbulence, gas-phase chemistry, and soot have a profound effect on the soot formation, growth, and destruction processes in turbulent reacting flows. Turbulence affects the soot field in two ways. First, due to a very large Schmidt number, soot is confined to very thin structures which are subsequently stretched into long filaments by the turbulent eddies. Second, soot is formed from Polycyclic Aromatic Hydrocarbons (PAH), which are formed only in regions of low scalar dissipation rate. The result of these properties is a both spatially and temporally intermittent soot field.

The use of large eddy simulation (LES) is emerging as a standard practice for turbulent combustion in practical devices [26]. Since LES resolves only large-scale features of the flow, combustion and soot formation which occur exclusively at the small scales must be modeled. In particular, the small-scale correlations between gas-phase species and soot precursor evolution need to be described.

The first three-dimensional LES of soot evolution in nonpremixed turbulent combustion was performed by El-Asrag and Menon [27]. Their modeling approach was based on the inclusion of a moment method for soot within the Linear Eddy Model (LEM) for the subfilter combustion processes. The model was shown to reasonably predict the soot volume fraction in an ethylene jet flame. However, while successful in the case considered, the modeling strategy relied on a simplistic soot model and a semi-empirical acetylene based soot inception model.

Recently, the small-scale interactions between soot, turbulence, and chemistry have been investigated using DNS. The works of Lignell and coworkers [28, 29] highlighted the role of transport and found that, while soot had roughly the same probability of moving towards or away from the flame, the soot concentration was highest when soot moved toward the flame. However, a semi-empirical acetylene based soot inception model was used in their work. More recently, Bisetti *et al.* [24] performed the first DNS of soot evolution with a PAH based soot inception model under this project. Results from this study are provided in Sec. 4.2, but some key findings are summarized here. In contrast to previous DNS studies, Bisetti *et al.* found that soot concentrations were highest when soot moved away from the flame. The data showed that soot moving toward the flame was oxidized quickly before appreciable

soot growth could occur, while soot moving away from the flame had long residences time during which significant growth by PAH condensation occurred. In addition, PAH was found not only to be very sensitive the scalar dissipation rate, which is partially responsible for soot intermittency, but also to exhibit significant unsteady kinetic effects due to relatively slow chemistry. This work highlighted not only the important role of PAH in turbulent nonpremixed combustion but also its difficulty in modeling.

As discussed in Sec. 2.2, the soot population is described using a set of moments of the underlying number density function. In this context, small-scale correlations between soot, turbulence, and gas-phase chemistry are best represented by a one-point one-time joint probability density function (PDF) of gas-phase species and soot moments. Options for modeling this joint PDF fall into two basic categories, presumed PDF modeling approaches and transported PDF modeling approaches. Computational details of these approaches are provided in Sec. 3.2.3.

Due to the inherent challenges in describing soot precursor chemistry, turbulence, and combustion processes, not much focus has been given to the modeling of this joint PDF. In LES, the subfilter correlations are often neglected. In this case, the PDF could be written as the product of the marginal PDFs of gas phase scalars and soot moments. However, given the high sensitivity to soot location with respect to the flame, this approximation is bound to introduce large errors. Recently, Mueller [30] have developed a presumed PDF approach, where the independence of the variables is still assumed but the marginal PDFs of the moments are modeled using an intermittency related term. In the Reynolds-averaged Navier Stokes (RANS) formulation, Lindstedt et al. [31] have directly solved the joint-PDF using a high-dimensional transport equation. It was found that accounting for the correlations between gas-phase scalars and soot moments introduced large differences in the soot profiles. Chandy et al. [32] have used the PDF approach in the context of LES, but with a simplified model for the soot chemistry.

3   Methods and Models

This section presents the methods used to study soot growth and oxidation processes (Sec. 3.1) and the models developed for simulation of soot evolution in LES (Sec. 3.2). The LES modeling discussion focuses on the novel closures developed in this project, which constitute the state-of-the-art in LES-based soot prediction.

3.1   Computational Methodology for Chemical Modeling of Soot Oxidation

For the present purpose we relied on theoretical approaches that are applicable to the study of large systems.

3.1.1   Energetics of Oxyradicals

To ensure consistency of results, geometry optimization of oxyradicals was performed at two levels of theory. One was the generalized gradient approximation (GGA) with the Perdew-Burke-Ernzerhof [33] exchange-correlation functional and double-zeta quality pseudo-atomic orbital basis set [34] as implemented in the SIESTA software [35]. The force tolerance in conjugate gradient optimization was set to 0.005 eV/AÅ. The other approach was the PM6 semi-empirical level of theory [36] in its restricted open-shell form as implemented in MOPAC2009 software.

   The harmonic oscillator model of aromaticity (HOMA) [37] was used to assess local electronic structure of individual six-membered rings in oxyradicals in order to explain observed trends in relative energies. HOMA is a geometry-based criterion that connects energetic descriptions of aromaticity to the geometry of the system that does not become prohibitively expensive with system size. The HOMA model focuses on the carbon-carbon bond lengths of the rings contained in the molecule, and is defined by,

$$\text{HOMA} = 1 - \frac{a}{n} \sum_{i=1}^{N} \left(r_{\text{CC}} - r_{\text{CC}-\text{benzene}} \right)^2 \tag{1}$$

where a was chosen to be 98.89 so that HOMA = 0 for a Kekule form of benzene and HOMA = 1 for the aromatic form of benzene, n is the number of bond lengths in the ring, r_{CC} is the carbon-carbon bond length in the system under consideration, and $r_{\text{CC}-\text{benzene}}$ is set to the experimental carbon-carbon bond length of benzene. Deviation of HOMA from 1 is a signature of deviation of the aromatic character of the ring from that of benzene. The sum of the HOMA values for individual rings in the PAH (cumulative HOMA) can be used to characterize aromaticity of a set of conjugated rings. In PM6 calculations, C-C bonds can be shorter than the values used to parametrize Eq. 1, so that negative values of HOMA are encountered. Technically, this indicates a ring being "less aromatic" than a Kekule form of benzene. For the practical purposes, negative values of HOMA at PM6 level were treated as zero.

   It should be noted that a certain ambiguity is encountered in optimization of oxyradical geometries. Relaxation of the carbon-carbon framework upon oxidation in a given position

7

at the edge may result in several alternative arrangements of carbon-carbon bonds and, therefore, different isomers with respect to location of π-aromatic fragments. It is impossible to guarantee that the most stable isomers of oxyradicals are found.

3.1.2   Potential Energy Surfaces

Density functional theory (DFT) was employed to calculate potential energy surfaces of all stable species and transition states for the oxyradical systems. Geometry optimization and vibrational frequency calculations were performed to identify all stationary points on the reaction pathways using the B3LYP hybrid functional [38] and a 6-311G(d,p) basis set. Zero-point energies (ZPE) and vibrational frequencies were scaled by a factor of 0.967 [39]. Transition states were confirmed to connect the reactant and product species by inspection of the normal mode for the single imaginary frequency of each saddle point. All the quantum-chemical calculations were carried out using the Gaussian 03 and the Gaussian 09 program packages.

3.1.3   Reaction Rate Coefficients

The rate coefficients of the thermally activated reaction systems were computed using the MultiWell suite of codes (MultiWell-2011.3) [40]. MultiWell solves the one-dimensional time-dependent energy-transfer master equations for a multi-well and multi-channel unimolecular reaction system using the Monte Carlo stochastic method. Microcanonical rate coefficients for the elementary reactions of these systems were calculated with MultiWell at the Rice–Ramsperger–Kassel–Marcus (RRKM) level of theory. This approach is estimated to produce rate coefficients to within an order-of-magnitude accuracy.

The key inputs to MultiWell—reaction barriers, frequencies, and moments of inertia—were determined from the DFT calculations. Following Gilbert and Smith [41], the real frequencies below 150 cm^{-1} were examined by graphically visualizing the associated normal mode vibrations to identify internal rotational modes. All internal rotors were treated as 1-D hindered rotors with rotational potential energy barriers calculated at the B3LYP/3-21G level.

Reaction rates were computed at temperatures ranging from 1500 to 2500 K and pressures from 0.01 to 10 atm. Argon was chosen as the bath gas collider. The exponential-down model with $\langle \Delta E_{\text{down}} \rangle = 260$ cm^{-1} was used to describe the collisional energy transfer. Lennard-Jones parameters were estimated from an empirical correlation [42]. The exact count, with an energy grain size of 10 cm^{-1} for the first segment of the double array and a maximum energy of 500,000 cm^{-1}, was employed to determine the density and sum of states. The maximum energy was increased to 2,000,000 cm^{-1} for the largest 11-ring structure. For each set of initial conditions, the number of stochastic trials was varied from 4×10^4 to 1×10^9 to keep statistical error below 5 %.

The thermal decomposition rate coefficients were derived from the exponential decay of the reactant molecule after a period of initial relaxation, as outlined and tested recently by Golden [43]. Following this procedure, a MultiWell simulation was started with either a monoenergetic or thermally activated initial energy distribution. After a period of initial relaxation, the average value of the internal energy approached a constant value, and a

fraction of the reactant molecule began to decompose exponentially. The slope of the decay on a semilog plot yielded the rate coefficient of interest.

3.2 LES Model for Soot Formation

The LES soot model has four major components: a statistical model for evolution of the soot particle size distribution (Sec. 3.2.1), a gas-phase combustion model (Sec. 3.2.2), a closure for subfilter correlations of soot and gas-phase chemistry (Sec. 3.2.3), and a model for PAH mass fraction (Sec. 3.2.4). Additionally, Sec. 3.3 discusses the chemical mechanism used for the LES simulations presented in Sec. 4.3.

3.2.1 Statistical Soot Modeling with HMOM

Soot particles are too numerous to track directly, so the population is described statistically with the Number Density Function (NDF) N_i. Typically, due to persistent nucleation of soot particles from PAH, the NDF is bimodal with one mode containing the smaller incipient spherical particles and the other mode containing larger, more mature fractal aggregates composed of smaller spherical primary particles. In order to describe the morphology of these aggregates, the NDF is defined over two internal dimensions: the volume V and the surface area S. Due to the high-dimensionality of the NDF (three spatial dimensions and two internal coordinates), it cannot be solved for directly, and a statistical model is required. For application to LES, due to cost constraints, the only tractable model is the Method of Moments, in which moments of the NDF are solved for rather than the NDF itself. The moments of the NDF of order x and y in volume and surface area, respectively, $M_{x,y}$ are given by

$$M_{x,y} = \sum_i V_i^x S_i^y N_i \ , \tag{2}$$

where summation over i implies summation over all particle sizes (written here in a discrete sense). While the Method of Moments does not provide the distribution directly, the moments of the NDF, that is, the soot volume fraction, total number density, average primary particle diameter, etc., are usually the quantities of interest, particularly in engineering applications.

The evolution of the NDF is governed by the Population Balance Equation (PBE), and the transport equation governing the evolution of the moments, obtained by taking the moment of the PBE, is given by

$$\frac{\partial M_{x,y}}{\partial t} + \frac{\partial u_i M_{x,y}}{\partial x_i} = \frac{\partial}{\partial x_i} \left(0.55 \frac{\nu}{T} \frac{\partial T}{\partial x_i} M_{x,y} \right) + \dot{M}_{x,y} \ , \tag{3}$$

where the first term on the right hand side is the thermophoresis of soot particles. Subsequently, this term will be combined with the convective term, and the total velocity will be denoted by

$$u_i^* = u_i - 0.55 \frac{\nu}{T} \frac{\partial T}{\partial x_i} \ . \tag{4}$$

The source term in Eq. 3 contains contributions from the formation, growth, and destruction processes that govern the internal evolution of the soot population. These processes include

particle nucleation from PAH dimers, PAH dimer condensation, particle coagulation, surface growth by the hydrogen abstraction/carbon addition (HACA) mechanism, oxidation, and oxidation-induced fragmentation. Details regarding the modeling of these processes can be found in Mueller *et al.* [18, 23, 25] and the references therein.

The major challenge with Method of Moments is that, in general, the source terms are unclosed. In other words, the source terms for the moment equations depend on moments which are not solved for. In this work, closure is obtained with the Hybrid Method of Moments (HMOM) [23]. Briefly, in HMOM, the contribution to the moments from the smaller incipient particles is described with a delta function as in the Direct Quadrature Method of Moments (DQMOM) [44], and the contribution to the moments from the larger particles is described with polynomial interpolation as in the Method of Moments with Interpolative Closure (MOMIC) [20]. An arbitrary moment is then given by

$$M_{x,y} = V_0^x S_0^y N_0 + \exp \sum_{r=0}^{R} \sum_{k=0}^{r} a_{r,k} x^k y^{r-k} \; , \tag{5}$$

where the location of the delta function (V_0, S_0) is fixed and R is the order of the polynomial interpolation. Given the weight of the delta function N_0, the polynomial interpolation coefficients are obtained from a set of moments which are solved for. In this work, $R = 1$, so three moment equations are solved: the total number density $M_{0,0}$, the total soot volume $M_{1,0}$, and the total soot surface area $M_{0,1}$. In diffusion flames, the primary soot growth mechanisms are nucleation and condensation [24], and the soot volume fraction is not sensitive to the number of moments. In addition, a transport equation is solved for the weight of the delta function N_0. The transport equation for this quantity is the same as Eq. 3 with the source term given by

$$\dot{N}_0 = \lim_{\alpha,\beta \to \infty} \frac{\dot{M}_{-\alpha,-\beta}}{V_0^{-\alpha} S_0^{-\beta}} \; . \tag{6}$$

Additional details regarding HMOM including the modeling of the formation, growth, and destruction processes can be found in Mueller *et al.* [23, 25].

3.2.2 Combustion Model

For sooting flames, the combustion model must be able to predict accurately not only the oxidation of the fuel but also the formation of soot precursors such as acetylene and PAH. However, at the same time, the model must be tractable in terms of both cost and closure. Therefore, the thermochemical state will be described with the Flamelet/Progress Variable (FPV) model of Pierce and Moin [45]. In the FPV model, the local thermochemical equation of state is obtained from the solutions of the steady flamelet equations [46], which are parameterized by the mixture fraction Z and a reaction progress variable C:

$$\xi = \mathcal{F}(Z, C) \; , \tag{7}$$

where ξ is any thermochemical variable (density, temperature, mass fractions, etc.) and $\mathcal{F}$ is the functional relationship obtained from the solution of the steady flamelet equations.

Due to the long time scales on which soot evolves combined with the sensitivity of soot evolution to temperature (and the thermochemical state in general), radiation losses must be

accounted for. Ihme and Pitsch [47] extended the FPV model to account for heat losses due to radiation (RFPV). The steady flamelet database is augmented with specific solutions of the unsteady flamelet equations, and a heat loss parameter H is added to the parameterization. The thermochemical equation of state is then given by

$$\xi = \mathcal{G}\left(Z, C, H\right) \ , \tag{8}$$

where $\mathcal{G}$ is the functional relationship obtained from the augmented flamelet database.

For sooting flames, some quantities, such as the source terms in Eq. 3, are functions of the both thermochemical quantities and the soot scalars. Therefore, the equation of state is generalized to allow for a dependence on both sets of quantities:

$$\phi = \mathcal{J}\left(\mathcal{G}\left(Z, C, H\right), \mathcal{M}_i\right) \ , \tag{9}$$

where ϕ is now any quantity that could depend on not only the thermochemical state but also the soot scalars and $\mathcal{M}_i$ is the vector of soot scalars, that is, the moments $M_{x,y}$ and the weight of the delta function N_0. For all of the quantities needed in the soot model, the general equation of state $\mathcal{J}$ can be written as the product of a function that depends only on the thermochemical state and one that depends only on the soot scalars:

$$\phi = \mathcal{G}\left(Z, C, H\right) \mathcal{K}\left(\mathcal{M}_i\right) \ , \tag{10}$$

where $\mathcal{K}$ is unity if ϕ is a strictly thermochemical quantity.

A convenient definition of the mixture fraction is a conserved scalar that is defined to be zero in the oxidizer stream and one in the fuel stream [48]. A major benefit of this definition is that the mixture fraction transport equation is independent of the transport model used for individual species. However, in sooting flames, the conserved scalar definition is inappropriate. In order to form soot, PAH are removed from the gas-phase, and the mixture is locally leaned. Therefore, the mixture fraction will be defined by the following transport equation:

$$\frac{\partial \rho Z}{\partial t} + \frac{\partial \rho u_i Z}{\partial x_i} = \frac{\partial}{\partial x_i}\left(\rho D_Z \frac{\partial Z}{\partial x_i}\right) + \dot{m}_Z \ , \tag{11}$$

where the mixture fraction Lewis number Le_Z is unity. The mixture fraction source term $\dot{m}_Z$ is defined analogously to the element mass fraction based mixture fraction of Bilger [49]:

$$\dot{m}_Z = \frac{\frac{\dot{m}_C - \dot{\rho} Z_{C,O}}{\nu_C W_C} + \frac{\dot{m}_H - \dot{\rho} Z_{H,O}}{\nu_H W_H} + 2\frac{\dot{\rho} Z_{O,O} - \dot{m}_O}{\nu_{O_2} W_{O_2}}}{\frac{Z_{C,F} - Z_{C,O}}{\nu_C W_C} + \frac{Z_{H,F} - Z_{H,O}}{\nu_H W_H} + 2\frac{Z_{O,O} - Z_{O,F}}{\nu_{O_2} W_{O_2}}} \ , \tag{12}$$

where $\dot{m}_i$ are element mass source terms, $\dot{\rho}$ is the source term in the continuity equation due to the removal of PAH from the gas-phase, Z_i are the element mass fractions with a second subscript indicating the value in the fuel or oxidizer stream, ν_i are the stoichiometric coefficients, and W_i are the molar masses. With the source term defined in this way, in the limit of unity Lewis numbers for all species, this mixture fraction definition would be equivalent to the element mass fraction based mixture fraction of Bilger [49]. With the mixture fraction defined as in Eq. 11, additional terms appear in the flamelet equations. These will be discussed below.

In previous works utilizing the FPV model [45, 47], the progress variable is defined as the sum of the mass fractions of the major products of combustion. However, in sooting flames, this conventional definition is again not appropriate. The PAH that are removed from the gas-phase have a much smaller H/C ratio than typical aliphatic fuels (less than one compared to greater than two). As a result of removing PAH from the gas-phase, the local H/C ratio increases, and the local effective fuel composition is changed. To account for this effect, the progress variable is defined by the following transport equation:

$$\frac{\partial \rho C}{\partial t} + \frac{\partial \rho u_i C}{\partial x_i} = \frac{\partial}{\partial x_i}\left(\rho D_C \frac{\partial C}{\partial x_i}\right) + \frac{\dot{m}_{\Sigma Y_i^C}}{C^*} \ , \tag{13}$$

where the progress variable Lewis number Le_C is unity, $\dot{m}_{\Sigma Y_i^C}$ is the conventional progress variable source term, that is, the sum of the source terms of the major productions of combustion, and C^* is a normalizing factor that accounts for the change in stoichiometry due to the removal of PAH. In addition, the progress variable is defined to be zero in both the fuel and oxidizer streams, irrespective of composition. The normalizing factor C^* is defined as the sum of the mass fractions of CO_2 and H_2O based on an idealized one-step reaction

$$C_aH_b + cO_2 + dN_2 \rightarrow eCO_2 + fH_2O + gO_2 + hN_2 \ , \tag{14}$$
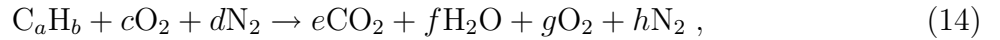
where the fuel composition and stoichiometric coefficients are determined from the local H/C ratio, a constant reference (element mass fraction based) mixture fraction at the nominal H/C ratio, and the local N/O ratio. As the local H/C ratio increases, c increases, and, therefore, C^* decreases. The progress variable defined in this way ensures that the equation of state (Eqs. 7-10) is unique. In non-sooting flames, the H/C ratio is constant; C^* is therefore a constant; and the progress variable as defined here is a linear function of the conventional progress variable.

Finally, the role of the third coordinate in the flamelet tabulation is to distinguish between states on which radiation has had little effect and states for which radiation has lowered the enthalpy. One possible choice for this coordinate is the enthalpy itself or the corresponding enthalpy deficit. The latter quantity has the benefit of a well defined adiabatic boundary (zero) for the simplest cases. However, when a detailed transport model is used or when soot is present (affects the adiabatic boundary for the enthalpy deficit), a transport equation definition is more convenient. This quantity, which will be called the heat loss parameter H, is defined by the transport equation

$$\frac{\partial \rho H}{\partial t} + \frac{\partial \rho u_i H}{\partial x_i} = \frac{\partial}{\partial x_i}\left(\rho D_H \frac{\partial H}{\partial x_i}\right) + \dot{\rho}H + \dot{q}_{\mathrm{RAD}} \ , \tag{15}$$

where the heat loss parameter Lewis number Le_H is unity and $\dot{q}_{\mathrm{RAD}}$ is the radiation source term. The heat loss parameter H is defined to be initially zero and becomes increasingly negative as the cumulative effect of radiation becomes stronger. The second term on the right hand side ensures that H is identically zero everywhere if the radiation source term is zero. The radiation model used in this work is an optically thin gray gas approach [50]. In the validation case considered in the next section, the soot volume fraction is sufficiently small that soot radiation can be neglected.

As mentioned previously, the flamelet equations contain additional terms other than those found in Peters [46] due to the source terms in the mixture fraction and continuity equations For unity Lewis numbers, which is the transport model considered in this work, the flamelet equations for the species mass fractions are

$$\rho\frac{\partial Y_i}{\partial \tau} = \frac{\rho\chi}{2}\frac{\partial^2 Y_i}{\partial Z^2} + \dot{m}_i - \dot{\rho}Y_i + (\dot{\rho}Z - \dot{m}_Z)\frac{\partial Y_i}{\partial Z} \ . \tag{16}$$

The final two terms on the right hand side are the new terms consisting of a source term due to the density source term and a convective term in mixture fraction space due to both the density and mixture fraction source terms. The primary role of these terms is to ensure that mass is conserved, and they do not play a substantial role in the dynamics of the flamelet equations. The flamelet equation for the temperature is

$$\rho c_p\frac{\partial T}{\partial \tau} = \frac{\rho c_p\chi}{2}\frac{\partial^2 T}{\partial Z^2} + \frac{\rho\chi}{2}\frac{\partial T}{\partial Z}\frac{\partial c_p}{\partial Z} + \sum_i \frac{\rho c_{p_i}\chi}{2}\frac{\partial Y_i}{\partial Z}\frac{\partial T}{\partial Z} + \dot{H} - \sum_i h_i\dot{m}_i + \dot{\rho}c_p Z\frac{\partial T}{\partial Z} - c_p\dot{m}_Z\frac{\partial T}{\partial Z} + \dot{q}_{\mathrm{RAD}} \ , \tag{17}$$

where $\dot{H}$ is the enthalpy source term due to the removal of PAH from the gas-phase. In addition to these quantities, flamelet equations are also solved for the progress variable C and the heat loss parameter H. From the transport equation for C (Eq. 13), the flamelet equation is

$$\rho\frac{\partial C}{\partial \tau} = \frac{\rho\chi}{2}\frac{\partial^2 C}{\partial Z^2} + \frac{\dot{m}_{\Sigma Y_i^C}}{C^*} - \dot{\rho}C + (\dot{\rho}Z - \dot{m}_Z)\frac{\partial C}{\partial Z} \ , \tag{18}$$

and, from the transport equation for H (Eq. 15), the flamelet equation is

$$\rho\frac{\partial H}{\partial \tau} = \frac{\rho\chi}{2}\frac{\partial^2 H}{\partial Z^2} + (\dot{\rho}Z - \dot{m}_Z)\frac{\partial H}{\partial Z} + \dot{q}_{\mathrm{RAD}} \ . \tag{19}$$

The values of C and H obtained from the solutions of these flamelet equations are then used to parametrize the solutions of Eqs. 16, 17 with the RFPV combustion model.

3.2.3 Closure of the joint subfilter PDF

In LES, spatially Favre filtered quantities are evolved for the velocity and scalars (Z, C, H, and $\mathcal{M}_i$), and spatially Favre filtered quantities are needed from the equation of state to evolve these equations (density, source terms, etc.). These Favre filtered quantities are obtained from the equation of state by convolution with the joint subfilter PDF $\widetilde{P}$:

$$\widetilde{\phi}(Z, C, H, \mathcal{M}_i) = \int\int\int\int \mathcal{J}(Z, C, H, \mathcal{M}_i)\widetilde{P}(Z, C, H, \mathcal{M}_i)\,d\mathcal{M}_i dH dC dZ \ . \tag{20}$$

Two basic options exist for specifying this joint PDF, the presumed shape PDF approach and the transported PDF approach, both of which are considered in this project.

3.2.3.1 Presumed Shape PDF Approach The model for the joint subfilter PDF is developed and validated *a priori* by Mueller and Pitsch [30] for any general combustion model. In the remainder of this section, a brief overview of this model is given including details specific to the RFPV combustion model considered.

As a first step in modeling the joint subfilter PDF, Eq. 10 and conditional distributions are used to split the subfilter PDF into a thermochemical component and a soot distribution conditioned on the thermochemical variables:

$$\widetilde{\phi}\left(Z,C,H,\mathcal{M}_i\right) = \int\int\int\int \mathcal{G}\left(Z,C,H\right)\mathcal{K}\left(\mathcal{M}_i\right)\widetilde{P}\left(Z,C,H\right)P\left(\mathcal{M}_i|Z,C,H\right)d\mathcal{M}_idHdCdZ \ .$$
(21)

Furthermore, due to the disparate time scales between the evolution of the thermochemical state and soot, Mueller and Pitsch [30] argue that the conditional soot distribution can be modeled by the marginal distribution. The previous relationship then simplifies to

$$\widetilde{\phi}\left(Z,C,H,\mathcal{M}_i\right) = \int\int\int \mathcal{G}\left(Z,C,H\right)\widetilde{P}\left(Z,C,H\right)dHdCdZ\int\mathcal{K}\left(\mathcal{M}_i\right)P\left(\mathcal{M}_i\right)d\mathcal{M}_i \ , \quad (22)$$

and the thermochemical and soot portions of the convolution are now completely independent. The model for the joint subfilter PDF in Eq. 20 has now been reduced to modeling the thermochemical subfilter PDF and the marginal soot subfilter PDF.

The thermochemical subfilter PDF for the RFPV model is from the work of Ihme and and Pitsch [47]. Mathematically, the thermochemical PDF is expressed by first recasting the equation of state (Eq. 8) in terms of two quantities that uniquely identify each flamelet solution in the database: $\Lambda = C\left(Z_{\mathrm{st}}\right)$ and $\Phi = H\left(Z_{\mathrm{st}}\right)$. Thermochemical quantities are then given by

$$\xi = \mathcal{G}\left(Z,C,H\right) = \mathcal{G}^\star\left(Z,\Lambda,\Phi\right) \tag{23}$$

or, as a filtered quantity,

$$\widetilde{\xi} = \int\int\int \mathcal{G}\left(Z,C,H\right)\widetilde{P}\left(Z,C,H\right)dHdCdZ = \int\int\int \mathcal{G}^\star\left(Z,\Lambda,\Phi\right)\widetilde{P}\left(Z,\Lambda,\Phi\right)d\Phi d\Lambda dZ \ .$$
(24)

By definition, Z, Λ, and Φ are independent, and the marginal distributions are modeled as a beta distribution for the mixture fraction [51–53] and delta distributions for Λ and Φ [47]:

$$\widetilde{P}\left(Z,\Lambda,\Phi\right) = \beta\left(Z;\widetilde{Z},\widetilde{Z''^2}\right)\delta\left(\Lambda - \widetilde{\Lambda}\right)\delta\left(\Phi - \widetilde{\Phi}\right) \ . \tag{25}$$

The resulting dependence on $\widetilde{\Lambda}$ and $\widetilde{\Phi}$ is then reexpressed as a dependence on $\widetilde{C}$ and $\widetilde{H}$, assuming a unique inversion exists, which is guaranteed if Eq. 8 is unique. In words, this mathematical formalism is practically implemented by individually convoluting each flamelet solution in the database with the beta distribution for the mixture fraction and tabulating the resulting set of data as a function of the filtered mixture fraction, subfilter mixture fraction variance, filtered progress variable, and filtered heat loss parameter.

The transport equation for the filtered mixture fraction is obtained by spatially filtering Eq. 11 and is given by

$$\frac{\partial\overline{\rho}\widetilde{Z}}{\partial t} + \frac{\partial\overline{\rho}\widetilde{u_i}\widetilde{Z}}{\partial x_i} = \frac{\partial}{\partial x_i}\left(\overline{\rho}\widetilde{u_i}\widetilde{Z} - \overline{\rho u_i Z}\right) + \frac{\partial}{\partial x_i}\left(\overline{\rho}\widetilde{D}_Z\frac{\partial\widetilde{Z}}{\partial x_i}\right) + \dot{\overline{m}}_Z \ . \tag{26}$$

The filtered source term has been closed with the use of the presumed subfilter PDF (Eq. 25). Likewise, the transport equation for the filtered progress variable is given by

$$\frac{\partial\overline{\rho}\widetilde{C}}{\partial t} + \frac{\partial\overline{\rho}\widetilde{u_i}\widetilde{C}}{\partial x_i} = \frac{\partial}{\partial x_i}\left(\overline{\rho}\widetilde{u_i}\widetilde{C} - \overline{\rho u_i C}\right) + \frac{\partial}{\partial x_i}\left(\overline{\rho}\widetilde{D}_C\frac{\partial\widetilde{C}}{\partial x_i}\right) + \overline{\left(\frac{\dot{m}_{\Sigma Y_i C}}{C^*}\right)} \ , \tag{27}$$

14

and the transport equation for the filtered heat loss parameter is given by

$$\frac{\partial \overline{\rho}\widetilde{H}}{\partial t} + \frac{\partial \overline{\rho}\widetilde{u}_i\widetilde{H}}{\partial x_i} = \frac{\partial}{\partial x_i}\left(\overline{\rho}\widetilde{u}_i\widetilde{H} - \overline{\rho u_i H}\right) + \frac{\partial}{\partial x_i}\left(\overline{\rho}\widetilde{D}_H\frac{\partial \widetilde{H}}{\partial x_i}\right) + \overline{\dot{\rho}H} + \overline{\dot{q}}_{\mathrm{RAD}} \ . \qquad (28)$$

For the mixture fraction used in this work, an algebraic model for the corresponding sub-filter variance could be derived by writing the transport equation for the subfilter variance, assuming local equilibrium, and replacing the subfilter scalar dissipation rate with a linear relaxation model [54]. The modeled subfilter variance would then be given by

$$\widetilde{Z''^2} = \frac{C_V}{\overline{\rho}\widetilde{S}}\left(2\overline{\rho}D_t\frac{\partial \widetilde{Z}}{\partial x_i}\frac{\partial \widetilde{Z}}{\partial x_i} - \left(\overline{\dot{\rho}Z^2} - \overline{\dot{\rho}}\widetilde{Z^2}\right) + \left(2\overline{\dot{m}_Z Z} - 2\overline{\dot{m}}_Z\widetilde{Z}\right)\right) \qquad (29)$$

where $\widetilde{S}$ is the magnitude of the filtered strain rate tensor, D_t is the subfilter diffusivity used to close the scalar flux in the mixture fraction equation, and C_V is a constant that must specified or determined dynamically. The last two terms on the right hand side are due to the source terms that appear in the continuity and mixture fraction equations and are themselves a function of the subfilter variance. As a result of these terms, a dynamic procedure for C_V would require an iterative approach, with test filtering required at each iteration. Depending on the number of iterations needed for convergence, this model could become very expensive and is therefore discarded as computationally impractical. Instead, a simpler and less expensive approach is taken, and the subfilter mixture fraction variance is obtained from the solution of a transport equation for the filtered square of the mixture fraction ($\widetilde{Z''^2} = \widetilde{Z^2} - \widetilde{Z}^2$):

$$\frac{\partial \overline{\rho}\widetilde{Z^2}}{\partial t} + \frac{\partial \overline{\rho}\widetilde{u}_i\widetilde{Z^2}}{\partial x_i} = \frac{\partial}{\partial x_i}\left(\overline{\rho}\widetilde{u}_i\widetilde{Z^2} - \overline{\rho u_i Z^2}\right) + \frac{\partial}{\partial x_i}\left(\overline{\rho}\widetilde{D}_Z\frac{\partial \widetilde{Z^2}}{\partial x_i}\right) - 2\overline{\rho}\widetilde{D}_Z\frac{\partial \widetilde{Z}}{\partial x_i}\frac{\partial \widetilde{Z}}{\partial x_i} - \overline{\rho}\widetilde{\chi}_{\mathrm{sgs}} - \overline{\dot{\rho}Z^2} + 2\overline{\dot{m}_Z Z} \ ,$$
$$(30)$$

where χ_{sgs} is the subfilter contribution to the dissipation rate. This equation is preferred over a transport equation for the subfilter variance directly since a production term, which is susceptible to large numerical errors, is not computed explicitly [55, 56]. Following the work of Ihme and Pitsch [57], the subfilter scalar dissipation rate is modeled with a linear relaxation model with the timescale determined from the subfilter eddy viscosity:

$$\widetilde{\chi}_{\mathrm{sgs}} = C_\chi\frac{\nu_t}{\Delta^2}\left(\widetilde{Z^2} - \widetilde{Z}^2\right) \ , \qquad (31)$$

where $C_\chi = 20$.

Due to the large spatial intermittency of soot, Mueller and Pitsch [30] modeled the soot subfilter PDF as a double delta distribution with a "non-sooting" mode and a "sooting" mode:

$$P\left(\mathcal{M}_i\right) = \omega\delta\left(\mathcal{M}_i\right) + (1 - \omega)\delta\left(\mathcal{M}_i - \mathcal{M}_i^*\right) \ , \qquad (32)$$

where ω is the subfilter intermittency and the $\mathcal{M}_i^*$ are defined such that convolution with the PDF recovers the filtered values of the soot moments $\overline{\mathcal{M}}_i$. The subfilter intermittency is smaller when soot is more homogeneous at subfilter scales and can be determined from the

filtered square of any one of the soot moments. However, Mueller and Pitsch [30] showed that the model performs best if the number density is used, and the subfilter intermittency is given by

$$\omega = 1 - \frac{\overline{M}_{0,0}^{\,2}}{\overline{M_{0,0}^{\,2}}} \, .$$ (33)

The filtered square of the number density is obtained from the solution of a transport equation.

The transport equation for the filtered soot moments (and weight of the delta function N_0) is obtained by applying a spatial filter to Eq. 3 and is given by

$$\frac{\partial \overline{M}_{x,y}}{\partial t} + \frac{\partial \widetilde{u}_i^* \overline{M}_{x,y}}{\partial x_i} = \frac{\partial}{\partial x_i} \left(\widetilde{u}_i^* \overline{M}_{x,y} - \overline{u_i^* M_{x,y}} \right) + \overline{\dot{M}}_{x,y} \, ,$$ (34)

and the corresponding equation for the filtered square of the number density is given by

$$\frac{\partial \overline{M_{0,0}^{\,2}}}{\partial t} + \frac{\partial \widetilde{u}_i^* \overline{M_{0,0}^{\,2}}}{\partial x_i} = \frac{\partial}{\partial x_i} \left(\widetilde{u}_i^* \overline{M_{0,0}^{\,2}} - \overline{u_i^* M_{0,0}^{\,2}} \right) - \overline{M_{0,0}^{\,2}} \frac{\partial \widetilde{u}_i^*}{\partial x_i} + 2\overline{M_{0,0}\dot{M}_{0,0}} \, .$$ (35)

In the latter equation, the subfilter contribution to the product of the number density squared and the divergence of the total velocity has been neglected following Mueller and Pitsch [30]. Due to the simple nature of the soot subfilter PDF, convolution with the double delta distribution occurs on-the-fly, and the portions of the soot source terms which are functions of the thermochemical state are stored in the same table as for the other quantities needed for the RFPV combustion model.

3.2.3.2 Transported PDF approach In the transported PDF approach, a partial differential equation describing the evolution of the PDF in physical coordinates and the thermochemical compositional space $\boldsymbol{\phi} = (Z, C, H, \mathcal{M}_i)$ is directly solved. In this study, the transported PDF approach is employed for simulation of a turbulent jet flame in cylindrical coordinates. For this purpose, the transport equation is written in cylindrical coordinates as follows [58]:

$$
\begin{aligned}
&\frac{\partial G_L}{\partial t} + \frac{\partial}{\partial r}\left[\left(A_r + \frac{B}{r}\right)G_L\right] + \frac{\partial}{\partial \theta}\left(\frac{A_\theta}{r}G_L\right) \\
&+ \frac{\partial}{\partial z}\left(A_z G_L\right) + \frac{\partial^2}{\partial r^2}\left(B G_L\right) + \frac{\partial^2}{\partial \theta^2}\left(\frac{B}{r^2}G_L\right) \\
&+ \frac{\partial^2}{\partial z^2}\left(B G_L\right) = -\frac{\partial}{\partial \phi_\alpha}\left[\left(\widetilde{\mathcal{D}_i|\boldsymbol{\phi}} + S_\alpha(\boldsymbol{\phi})\right)\frac{G_L}{r}\right]
\end{aligned}
$$ (36)

where $G_l = rP$, $B = D_T$. A_r, A_θ, and A_z are given by

$$A_r = \widetilde{u}_r + \frac{1}{\overline{\rho}}\frac{\partial}{\partial r}\left(\overline{\rho}B\right)$$ (37)

$$A_\theta = \widetilde{u}_\theta + \frac{1}{r\overline{\rho}}\frac{\partial}{\partial \theta}\left(\overline{\rho}B\right)$$ (38)

$$A_z = \widetilde{u}_z + \frac{1}{\overline{\rho}}\frac{\partial}{\partial z}\left(\overline{\rho}B\right) \, .$$ (39)

16

The terms on the RHS of the PDF transport equation represent transport in composition space and consist of molecular mixing and chemical reactions, respectively. The primary advantage of the PDF approach is that the chemical source term appears closed and does not require modeling. However, modeling is required for describing the conditional diffusion term, $\widetilde{\mathcal{M}_i|\boldsymbol{\phi}}$:

$$\widetilde{\mathcal{D}_i|\boldsymbol{\phi}} = \frac{1}{\rho}\overline{\nabla \cdot \rho D \nabla \phi_i|\boldsymbol{\phi}}. \tag{40}$$

This term is closed using the interaction by exchange with the mean (IEM) model [59–61]:

$$\frac{\partial}{\partial \phi_i}\left(F_L\widetilde{\mathcal{D}_i|\boldsymbol{\phi}}\right) = \nabla \cdot \bar{\rho}\widetilde{D}\nabla F_L/\rho + \frac{\partial}{\partial \phi_i}\left[\frac{1}{\tau}\left(\phi_i - \widetilde{\psi}_i\right)F_L\right]. \tag{41}$$

Here τ is a mixing time-scale that needs to be specified, and $\widetilde{D}$ is a common diffusivity that is used for all the scalars in $\boldsymbol{\psi}$. In this work, this is taken to be equal to the diffusivity of mixture fraction. Note that the differential diffusion between soot moments and the gas phase scalars could be important [62]. As a first step, this is neglected here, but the differential diffusion of high-Schmidt number scalars could be considered by modifying the dissipation time scale [63, 64].

The transported PDF approach requires solution of the high-dimensional PDF transport equation (Eq. 36), which spans eleven dimensions for the state vector used in this work. Conventional finite difference or finite volume methods are not tractable, and a Lagrangian Monte-Carlo method is used [59–61, 65, 66]. In the Lagrangian approach, the computational domain is seeded with a large number of notional particles that evolve in physical and compositional spaces using a set of stochastic differential equations. Each of these particles carries a property vector that consists of the particle location vector, a characteristic weight, and the $\boldsymbol{\psi}$ vector.

The evolution of the particles in physical space is governed by the following equations:

$$dr^n = \left(A_r^n + \frac{B_1^n}{r^n}\right)dt + \sqrt{2dtB_1^n}dW_r, \tag{42}$$

$$d\theta^n = \frac{A_\theta^n}{r^n}dt + \sqrt{2dt\frac{B_1^n}{(r^n)^2}}dW_\theta, \tag{43}$$

$$dz^n = A_z^n dt + \sqrt{2dtB_1^n}dW_z, \tag{44}$$

where the superscript n denotes the particle index, and dW_i is a Weiner diffusion process with zero mean and variance of 1, and $B_1 = D + D_T$. The velocity and diffusivity fields used in this equation are interpolated onto the particle locations using trilinear interpolation. The transport in composition space consists of mixing and chemical reactions. The particle equation corresponding to the IEM mixing model is given by

$$d\boldsymbol{\phi}^n = \frac{1}{\tau}\left(\widetilde{\boldsymbol{\psi}} - \boldsymbol{\phi}^n\right), \tag{45}$$

where $\widetilde{\boldsymbol{\psi}}$ is the filtered composition vector in a given filter volume, $\boldsymbol{\phi}^n$ is the particle composition vector, and τ is a mixing time scale. In this work, the mixing time scale is determined

17

using the local effective diffusivity and the filter scale.

$$\tau = c_\phi \frac{\Delta^2}{D + D_T},\tag{46}$$

where c_ϕ is a model coefficient. The dynamic procedure proposed by Raman and Pitsch [66] is used for evaluating c_ϕ. The particle equations thus reduce to solving a vector of ordinary differential equations.

$$d\boldsymbol{\phi}^n = \mathbf{S}(\boldsymbol{\phi}^n)dt,\tag{47}$$

where $\mathbf{S}$ is the vector of chemistry and soot source terms.

The particle weights are proportional to the mass of the fluid they represent. It should be noted that the PDF transport equation is formulated for rF_L instead of F_L. This modified formulation ensures that the weights have no evolution equation. In other words, the particle weights are initialized at the inlet but do not change with time. To ensure consistency, the particle weights are set proportional to $\bar{\rho}^n r_0^n$ at the inlet, where $\bar{\rho}^n$ is the Eulerian density interpolated to the particle location, and r_0^n is the radial location of the particle.

3.2.4 PAH Model

The final component of the LES model to be discussed is a model for obtaining the PAH mass fraction and, subsequently, the mass transfer rate from the gas-phase to soot. The simplest approach would be to take the PAH mass fraction directly from the RFPV combustion model. However, the DNS study of Bisetti *et al.* (see Ref. 24 and Sec. 4.2) demonstrated that the PAH mass fraction deviates significantly from the steady flamelet model due to the relatively slow PAH chemistry. As the scalar dissipation rate changes, species with faster chemistry (e.g., the major species of combustion) respond quickly to these changes, and the unsteady term in the flamelet equations is negligible. For species with slower chemistry, a longer time is needed to respond to changes in the dissipation rate; the unsteady term in the flamelet equations must be retained; and the mass fractions of these species cannot be accurately described with the solutions to the steady flamelet equations.

Like PAH, NO is governed by relatively slow chemistry. To model the unsteady effects, Ihme and Pitsch [47] developed a transport equation model for NO. The same approach will be taken here for PAH. The spatially filtered transport equation for a lumped PAH mass fraction is given by

$$\frac{\partial \bar{\rho}\widetilde{Y}_{\mathrm{PAH}}}{\partial t} + \frac{\partial \widetilde{\rho}\widetilde{u}_i\widetilde{Y}_{\mathrm{PAH}}}{\partial x_i} = \frac{\partial}{\partial x_i}\left(\bar{\rho}\widetilde{u}_i\widetilde{Y}_{\mathrm{PAH}} - \bar{\rho}\widetilde{u_i Y_{\mathrm{PAH}}}\right) + \frac{\partial}{\partial x_i}\left(\bar{\rho}\widetilde{D}_{\mathrm{PAH}}\frac{\partial \widetilde{Y}_{\mathrm{PAH}}}{\partial x_i}\right) + \overline{\dot{m}}_{\mathrm{PAH}},\tag{48}$$

where $\dot{m}_{\mathrm{PAH}}$ is the sum of the sources of all of the PAH species. If all of the PAH have the same molecular diffusivity D_{PAH} (e.g., a unity Lewis number assumption), then the preceding equation is exactly the transport equation for the sum of the PAH mass fractions. If the PAH do not all have the same molecular diffusivity, then the diffusivity of naphthalene (generally the PAH species with the largest concentration) is preferred for D_{PAH}, and the preceding equation is then an approximate model for a lumped PAH.

With a conventional model for the scalar flux, the lone unclosed term in Eq. 48 is the filtered source term. This source can be decomposed into three components: a chemical

18

production term $\dot{m}_+$, a chemical consumption term $\dot{m}_-$, and an additional consumption term due to the mass transfer rate from the gas-phase to soot (dimerization) $\dot{m}_D$. For each individual species, the chemical production term is independent of the concentration of the species; the chemical consumption term is linear in the concentration of the species; and the dimerization term is quadratic in the concentration of the species. For the lumped species, the source term will be decomposed in the same way:

$$\overline{\dot{m}}_{\text{PAH}} = \overline{(\dot{m}_+)} + \overline{\left(\frac{\dot{m}_-}{Y_{\text{PAH}}}\right) Y_{\text{PAH}}} + \overline{\left(\frac{\dot{m}_D}{Y_{\text{PAH}}^2}\right) Y_{\text{PAH}}^2} \,. \tag{49}$$

Written in this way, the three terms in parentheses are nearly independent of the PAH mass fraction and can be taken directly from the RFPV combustion model. Following the work of Ihme and Pitsch for NO [47], the correlations in the second and third terms are closed by assuming scale-similarity between the transport equation model and the RFPV combustion model. The final form of the source term is then

$$\overline{\dot{m}}_{\text{PAH}} = \overline{\dot{m}}_+^{\text{RFPV}} + \overline{\dot{m}}_-^{\text{RFPV}} \left(\frac{\widetilde{Y}_{\text{PAH}}}{\widetilde{Y}_{\text{PAH}}^{\text{RFPV}}}\right) + \overline{\dot{m}}_D^{\text{RFPV}} \left(\frac{\widetilde{Y}_{\text{PAH}}}{\widetilde{Y}_{\text{PAH}}^{\text{RFPV}}}\right)^2 \,, \tag{50}$$

where the superscript $^{\text{RFPV}}$ indicates quantities which are obtained from the RFPV combustion model.

3.3 Chemical Mechanism

For construction of the flamelet look-up tables used in the LES computations, solutions to the steady and unsteady flamelet equations are obtained with FlameMaster [67]. The base chemical mechanism is from Blanquart *et al.* [68] with extensions from Narayanaswamy *et al.* [69]. The mechanism has been extensively validated for simple C_0-C_4 fuels, n-heptane, iso-octane, benzene, and several substituted aromatics (toluene, ethylbenzene, m-xylene, and α-methylnaphthalene) at both lean and rich conditions in several configurations. In addition, the mechanism contains PAH chemistry up to C_{16} and C_{18} species (pyrene, etc.). Numerous PAH formation and growth pathways are included in the mechanism.

For the commercial natural gas mixture considered in this work, the mechanism predicted that most naphthalene was formed from the combination of an indenyl radical and a methyl radical [70, 71]. However, the as-compiled mechanism did not contain a pathway for the decomposition of indenyl under rich conditions, and all of the indenyl that was formed (primarily through acetylene addition to a benzyl radical) eventually ended up as naphthalene, leading to unphysically large PAH concentrations. Therefore, a global rate for the thermal decomposition of indenyl was added to the mechanism based on the work of Laskin and Lifshitz [71]:

$$C_9H_7 \rightarrow C_3H_3 + C_4H_2 + C_2H_2 \tag{51a}$$
$$C_9H_7 \rightarrow C_5H_5 + C_4H_2 \tag{51b}$$
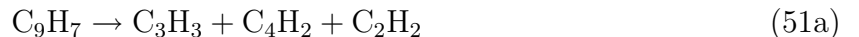
where the branching ratio between the two product channels is two in favor of the first. At lean conditions, this thermal decomposition is not competitive with oxygen-containing species and, therefore, does not affect any of the previous validation results [68, 69].

4 Results and Discussion

This section begins by presenting results from our investigation of soot oxidation (Sec. 4.1), then proceeds to discuss a series of turbulent flame investigations, including a DNS study of soot formation (Sec. 4.2) and validation studies of the LES soot model, using both the presumed PDF (Sec. 4.3.3) and transported PDF (Sec. 4.3.4) approaches.

4.1 Oxidation of Soot

We begin this section by first reporting results of our study of bay-capping reactions, one of the important reaction steps in soot surface growth, and examine their effect on the evolution of soot particle growth. We then examine the thermodynamic stability of the key intermediates of soot oxidation, graphene-edge oxyradicals, located at both zigzag and armchair sites, and then proceed with the kinetics of graphene oxyradical decomposition.

4.1.1 Surface growth: Bay-capping reactions

Controlling formation of soot in modern combustion systems requires a good mechanistic understanding of soot particle growth. One of the biggest unknowns, particle inception, received substantial attention in recent years and its mechanistic picture steadily advances toward a unified theory [5]. Another part of the mechanism, surface growth, has transformed from an empirical rate law to a simple elementary-reaction model, to a complex, multi-step process. The complexity of the surface growth mechanism stems from numerous possibilities of chemical transformations taking place at graphene edges, presumed to be the building units of soot particles. Among them are game-changing processes: migrations of lone [72] and embedded [73] five-member rings, which give rise to rapid lateral translation of five-member rings along zigzag edges.

Most recently, Whitesides and Frenklach [10] presented a new detailed kinetic Monte-Carlo (KMC) model of graphene-edge growth with a total of 42 surface transformations. Evolving edge morphology and growth rate were found to be affected by the rates of key reactions. One of the most interesting among them is capping, the addition of acetylene to an embedded five-member ring, shown in Fig. 1. The significance of this reaction step is
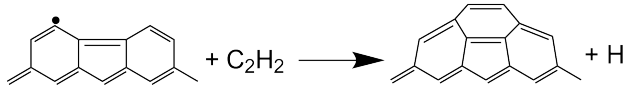
Figure 1: Bay-capping reaction.

several-fold [10]. First, it pins down the five-member ring and prevents it from migrating. As ring migration generally leads to smoother surfaces, this aspect of capping works against it. Second, capping forms armchair-like sites that initiate zipper-type growth of new layers. Finally, capping permanently embeds five-member rings into the growing graphene structure and hence causes it to curve.

In the Whitesides and Frenklach study [10], this reaction was assumed to have the rate coefficient of its zigzag-edge analog because no rate data were available. The importance

of this reaction called for a thorough examination of its kinetics. To do so, we employed a combination of quantum chemical calculations and reaction rate analysis to explore the elementary steps of these types of reactions and to derive their rate coefficients. To evaluate the influence of the embedded five-member ring on six-member ring cyclization, we compared the energetics and reaction rates of capping an embedded five-member ring with those of capping a "regular" armchair graphene-edge site.

The rate coefficient calculated by us for capping the five-member-ring bay turned out to be of the same order of magnitude as its prior estimate, yet with a substantially different activation energy. However, the calculated rate coefficient for capping the six-member-ring bay is one order of magnitude lower than that used in prior KMC studies.

To examine the influence of the new kinetic data, we performed detailed kinetic Monte Carlo simulations changing the rate coefficients of the bay-capping reactions of the initial model. With the new rate coefficients, the overall growth rates of graphene edge were lower. The most dramatic effect was obtained at 2000 K. At the same time, the change in the rate coefficients did not affect the phenomenon of curving obtained for graphene-edge evolution in the previous study [10], as shown in Fig. 2.

(a)   **(b)**   **(c)**
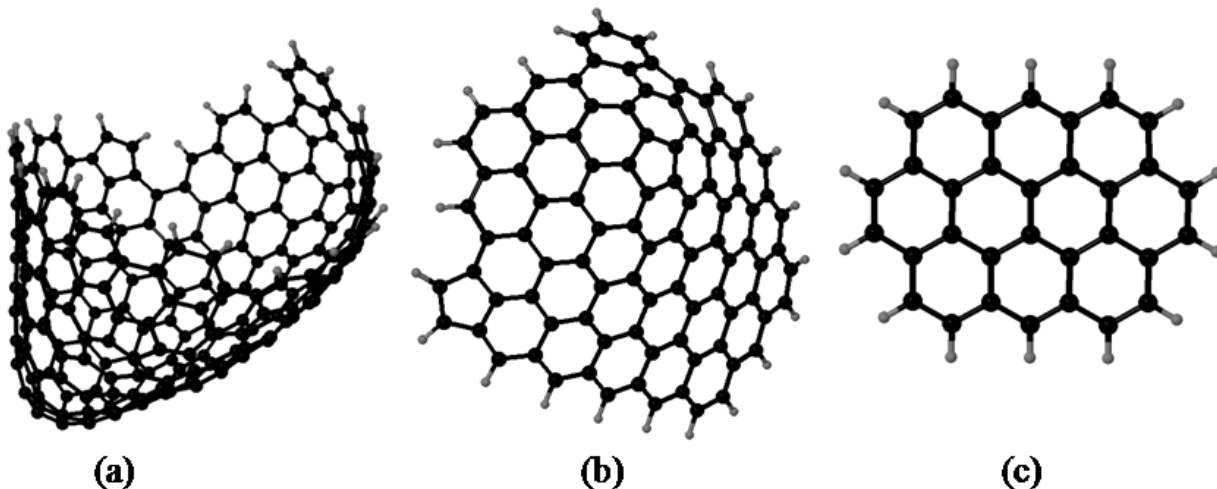
Figure 2: Representative structures formed at a simulation time of 5 ms from coronene growth at (a) 1500 K, (b) 2000 K, and (c) 2500 K

This work was presented at the 33rd Symposium on Combustion [74].

4.1.2   Thermodynamic stability of oxyradicals

The oxidative destruction and resistance to oxidation of soot are of practical interest, as these are primary pathways through which soot production is alleviated. However, experimental data are scarce. When such data are available, they typically have been collected on a composition of soot which is not well determined and dependent on many experimental factors, making extrapolation to new systems challenging. Therefore, theoretical methods are ideal as they provide control over modeling conditions and facilitate extension to larger and more complex systems.

Our first objective is investigation of the thermodynamic stability of graphene oxyradicals, which showed a systematic trend with position of the chemisorbed oxygen atom on the graphene edge. Our second objective is to explain the observed trend, and, to this end, we employ the theory of aromaticity. We chose the linear pentacene polyaromatic hydrocarbon (PAH) as the model of the graphene edge. Because the present focus is on processes that involve only the exterior of a graphene sheet, this model should be adequate. It contains the essential structural element involved in the key processes, i.e. the zigzag edge which can be systematically extended by both increasing the length of the polycyclic chain and by adding extra layers. We undertake a systematic investigation into the thermodynamic stability of pentacene oxyradicals as a model for the critical intermediate in graphene oxidation. The result of this investigation is an intuitive chemical model based on aromaticity and localization that explains the observed trends.

We started with a series of linear polyaromatics, investigating the relative thermodynamic stability of pentacene oxyradicals, shown in Fig. 3. Oxyradicals with O bonded to interior rings were found to be more stable than those with O bonded to exterior rings in the range of combustion temperatures. To assess thermodynamic stability, we calculated the standard Gibbs free energies of the four pentacene oxyradicals relative to oxyradical II with results shown in Fig. 4.

We then expanded the investigation to larger, two-dimensional aromatics, those shown in Fig. 5. As in the case of the linear aromatics, the energy and hence the thermodynamic stability of larger, two-dimensional aromatic oxyradicals are found to depend critically on the position of oxygen in the PAH edge. This is demonstrated in Fig. 6 where we plot the standard enthalpies of formation of oxyradical versus values of HOMA averaged per ring and the standard deviation of individual HOMA values. As can be seen from this figure, there is a nearly linear correlation of the data, which indicates that the radical stability depends on the value of HOMA as well as a distribution of HOMA over the molecular substrate. These results indicate that oxyradical stability correlates with local aromatic character of six-atom rings characterized by the harmonic oscillator measure of aromaticity (HOMA) and with the distribution of HOMA values in molecules. It is demonstrated that oxidation at the edge has a non-local effect on the structure of PAHs and leads to distinguishable types of HOMA patterns that are common for both families of PAHs.

The interplay between local aromaticity of benzene-like rings of graphene substrates and the global aromaticity of the latter has led to a simple explanation of the trends in relative stability of two families of linear and two-dimensional PAH oxyradicals. For any substrate, chemisorption of an oxygen atom leads to the loss of aromaticity by the corresponding ring and eliminates its contribution to inter-ring conjugation. As a result, the relative stability of linear oxyradicals is controlled by fragmentation of the globally delocalized π-electron system. It mainly depends on the nature and the amount of locally π-aromatic fragments formed. Relative energies of linear oxyradicals show linear dependency of the cumulative HOMA aromaticity measure. This linear trend is essentially preserved in oxyradicals of two-dimensional substrates. No fragmentation but rather rearrangement of the pattern of local aromaticity occurs upon oxidation in the edge. It appears to lead to three classes of local aromaticity patterns. The first class is checkerboard-like. It is related to the Clar structure of coronene with highly aromatic disjoint rings. The second class resembles a resonance of Clar structures leading to cycles of six weakly aromatic rings, hence the designations "Clar
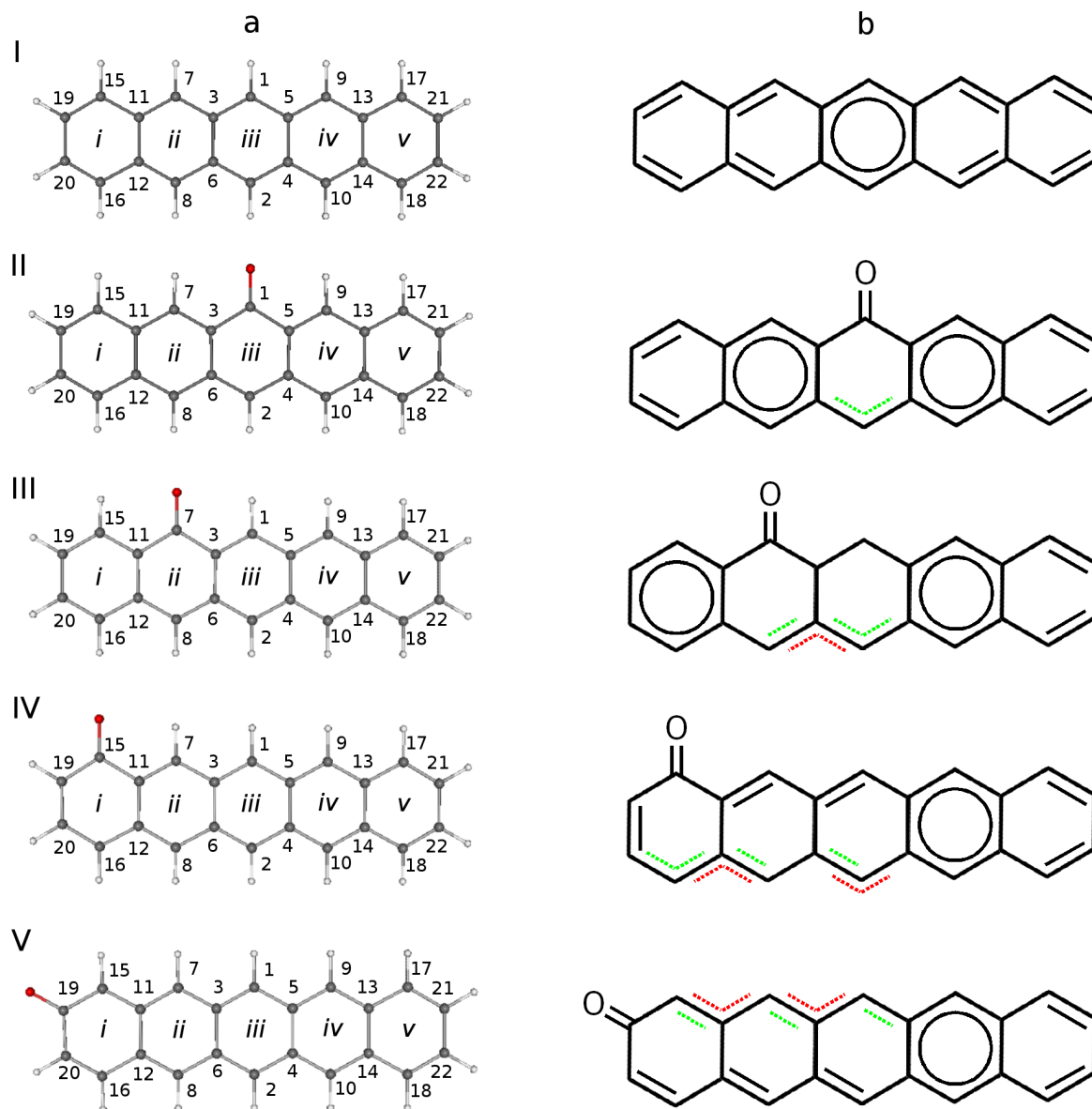
Figure 3: Left panel: structures of the pentacene molecule (I) and pentacene oxyradicals with the oxygen atom in different positions (II V). Connections between atoms are drawn on the basis of the interatomic distances. Upper case Roman numerals designate oxyradicals with different O atom positions; lower case italic Roman numerals designate six-atom rings; Arabic numerals enumerate C atoms. Right panel: schematic representation of chemical bonding in systems I-V.
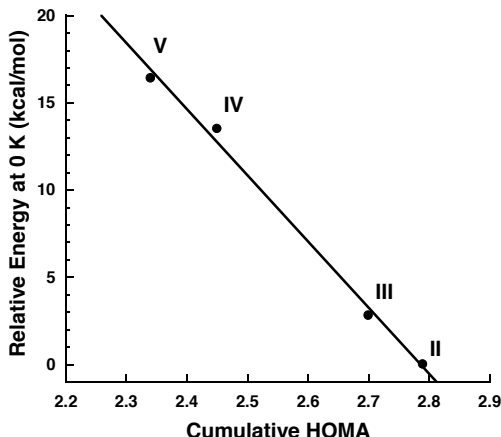
Figure 4: ZPE-corrected relative energies of oxyradicals II-V (at the B3LYP/6-311G(d,p) level of theory) plotted against cumulative HOMA. The straight line reflects nearly linear dependence.

coronene" and "superaromatic coronene". Also, there is an "intermittent" class which can be seen as a mixture of the previous two. It remains to be seen if these three types of patterns are of general relevance and emerge in other graphene-based systems. Their formation does not seem to be affected by the nature of the substrate edges in the present research, so the assumption of generality is plausible. This shows that a very local event, such as oxidation of the edge, has a strongly non-local effect on the entire framework of C-C bonds.

These results are reported in Refs. 75, 76, and 77.

4.1.3 Kinetics of oxyradical decomposition

Progress has been made in understanding reaction mechanisms of PAH formation and PAH-edge growth at high temperatures [4–6, 10]. Oxidation of PAH edges, while part of the overall growth processes in oxygen-containing environments, has received substantially less attention. The goal of the present study is to explore PAH-edge degradation mechanisms, focusing on the fate of PAH oxyradicals.

A number of studies investigated the oxidation of small aromatic molecules and oxygen chemisorptions at selective sites of two- and three-ring aromatics (for references see Ref. 78). According to these studies, at high temperatures the reaction between a phenyl radical and molecular oxygen leads to the formation of phenoxy radical, which subsequently decomposes to generate cyclopentadienyl radical, C_5H_5, and carbon monoxide, CO, shown in Fig. 7. Similarly, a naphthoxy radical is produced from a naphthyl radical reacting with O_2 and then decomposes to an indenyl radical and CO.

Fewer studies have been carried out on edge oxidation of larger PAHs and those pertinent to the present work are all theoretical. Radovic [79] examined the energetics and feasible pathways for the oxidation to CO_2 of several five- to seven-ring mostly peri-condensed PAHs. Celnik et al. [13] computed the rate of O_2 reaction with a PAH radical site generating an
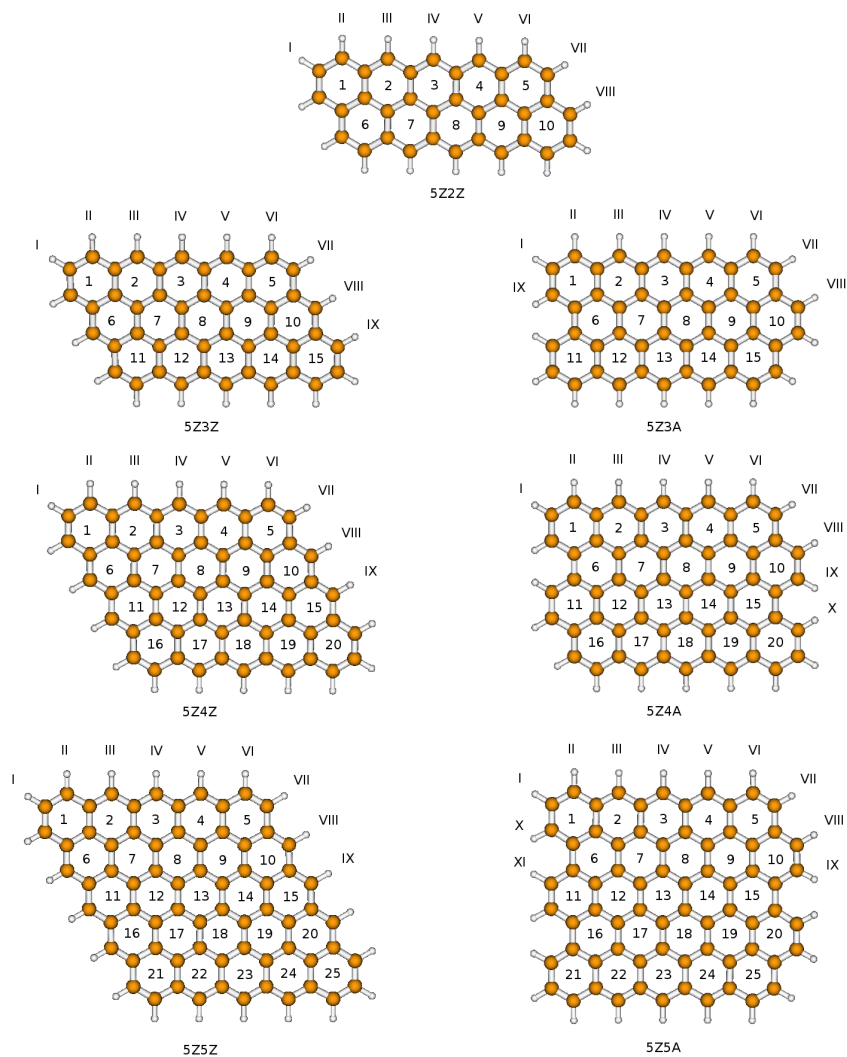
Figure 5: Structures of two-dimensional PAH substrates used to form oxyradicals. Roman numerals label position of oxygen in corresponding oxyradicals. Arabic numerals label six-atomic rings.
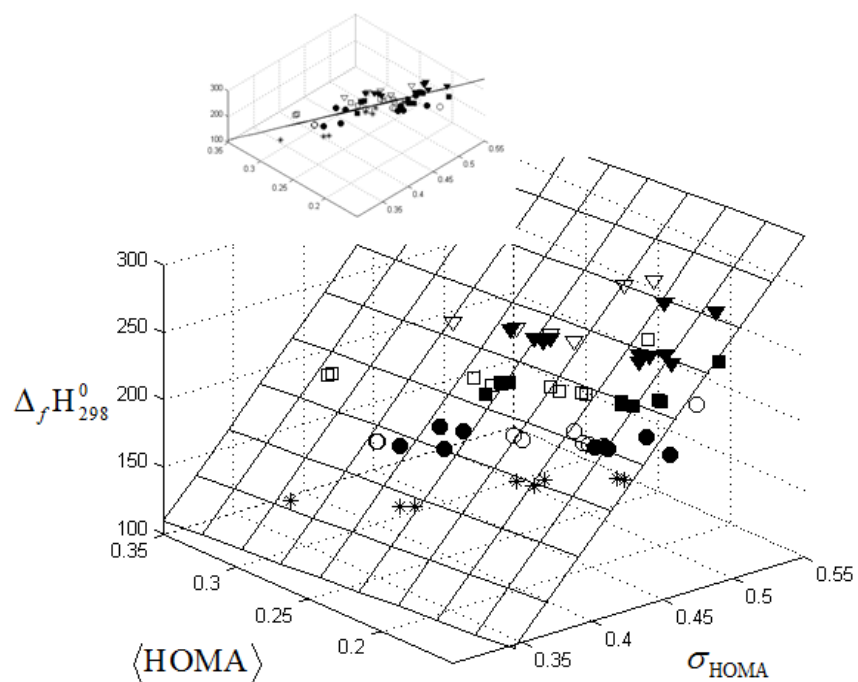
Figure 6: Standard enthalpy of formation, in kcal/mol, of two-dimensional oxyradicals versus average values of HOMA and its standard deviation, σ_{HOMA}. Also shown is a plane that is a fit through the data points. The inset displays the same figure but rotated to show the projection normal to the plane.
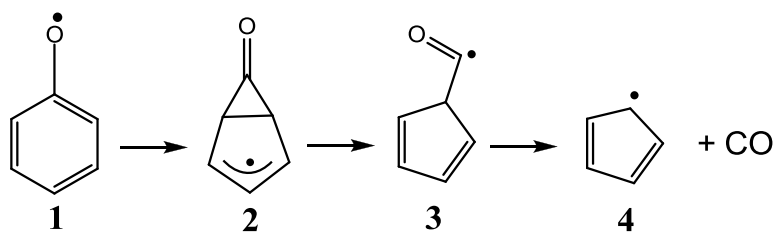
Figure 7: Phenyl oxidation by O_2.

oxyradical and an oxygen atom for benzene, naphthalene, anthracene, phenanthrene, pyrene, and benzo[a]anthracene at the B3LYP/6-31G(d) level of theory. Their results, in accord with an earlier study of Kunioshi et al. [80], showed that the oxidation rates are similar for all radical sites studied except for armchair sites, which exhibited higher activation energy. However, the decomposition of the oxyradicals generated was not investigated in their study.

All of these studies suggest that oxyradicals are not only the major intermediates during oxidation of small aromatics, but also of large PAHs and graphene edges. It is of interest, therefore, to investigate the fate of PAH oxyradicals and shed light on the evolution of graphene edges and soot surfaces during oxidation. Specifically, we want to determine whether graphene-edge oxyradicals decompose similarly to phenoxy and naphthoxy radicals and, if so, with what rates. We answer these questions by performing a theoretical study, following the previous work on the thermodynamic stability of graphene oxyradicals, at the same level of theory.

First, we focus on zigzag edges. For this we select pentacene, as in our prior thermodynamic study. We examine the reaction kinetics of four pentacene oxyradicals, shown in Fig. 8, as well as that of phenoxy radical, by solving energy-transfer master equations.

We examined four pentacene oxyradicals distinguished by O-atom bonding to carbon atoms, denoted I, II, III, and IV, respectively; these structures are displayed in Fig. 8. Although the four pentacene oxyradicals look similar in structure, they are quite different in potential energy and thermodynamic stability. Pentacene oxyradicals I, II, and III are 17.1, 14.1, and 2.9 kcal/mol higher in potential energy, respectively, than oxyradical IV at the B3LYP/6-311G(d,p) level. We showed earlier [75] that below 1000 K the thermodynamic stability of the four oxyradicals follows the trend of their relative potential energies, i.e. the order IV > III > II > I, while above 1000 K oxyradical III becomes thermodynamically more stable than IV because of the larger entropy contribution to the Gibbs free energy. The relative energies and stabilities can be explained, as for the thermodynamics case Fig. 8, by the different fragmentation of the delocalized π-electron system of the precursor pentacene molecule arising from the different locations of the chemisorbed oxygen atom.

Examination of the decomposition path of the phenoxy radical indicates that the oxygen atom, O1, and the three carbon atoms, C2, C3, and C4 (labeled in Fig. 8) are involved in breaking existing and forming new C-C bonds. It is worthwhile comparing bond lengths of these four atoms for pentacene oxyradicals with those for phenoxy radical. As shown in Fig. 8, the bond lengths or distances between O1 and C2, C2 and C3, C2 and C4, and C3 and C4 of oxyradical I are closest to those of the phenoxy radical among the four pentacene oxyradicals. For instance, the distance between C3 and C4 is in the order of phenoxy < I < II < III < IV. Therefore, the similarity in structure of the pentacene oxyradicals to the phenoxy radical is in the order of I > II > III > IV. An oxyradical with a shorter distance between C3 and C4 is more likely to decompose in the same way as the phenoxy radical and to generate a cyclic intermediate.

We explored the potential energy surfaces at the B3LYP/6-311G(d,p) level for the thermal decomposition of the four pentacene oxyradicals. To facilitate analysis of the pentacene oxyradical systems, we also computed the phenoxy reaction system at the same level of theory. A detailed report of the computed molecular properties—electronic energies, geometries, and vibrational frequencies—for the species involved is given in Ref. 78. Our results indicate that the decomposition pathways of pentacene oxyradicals I and II leading to CO
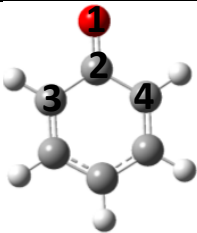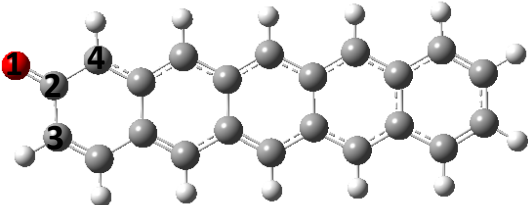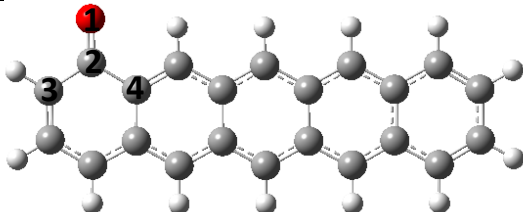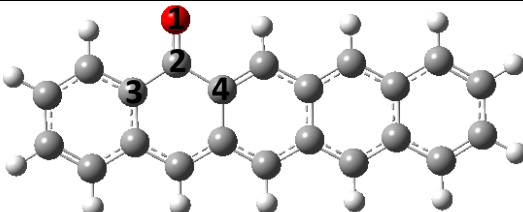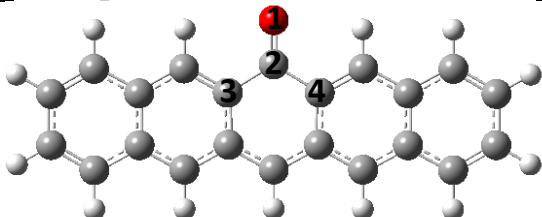
Species	Structure	Bond-length(Å)
Phenoxy		O1-C2: 1.251
		C2-C3: 1.452
		C2-C4: 1.453
		C3-C4: 2.476
Pentacene oxyradical I		O1-C2: 1.235
		C2-C3: 1.475
		C2-C4: 1.453
		C3-C4: 2.485
Pentacene oxyradical II		O1-C2: 1.232
		C2-C3: 1.456
		C2-C4: 1.493
		C3-C4: 2.501
Pentacene oxyradical III		O1-C2: 1.226
		C2-C3: 1.483
		C2-C4: 1.489
		C3-C4: 2.529
Pentacene oxyradical IV		O1-C2: 1.225
		C2-C3: 1.488
		C2-C4: 1.487
		C3-C4: 2.532

Figure 8: Structures of phenoxy and pentacene oxyradicals

generation are very similar to that of phenoxy radical, while CO is unlikely to be produced following the same pathways for oxyradicals III and IV.
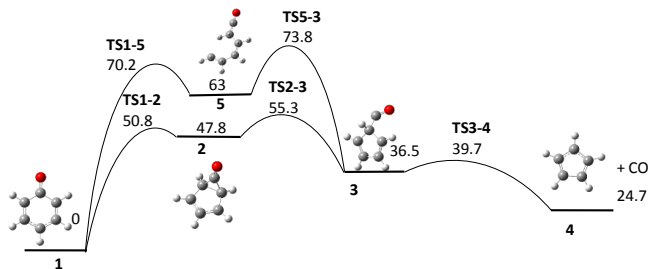
Figure 9: Minimum potential energy paths for the thermal decomposition of phenoxy radical at the B3LYP/6-311G(d,p) level. Energies (in kcal/mol) at 0 K relative to reactants are shown for each transition state and local minimum.

Figure 9 shows the minimum potential-energy paths for the decomposition of the phenoxy radical following different pathways. One proceeds through an electro-cyclic mechanism, forming the cyclic intermediate 2, followed by C-C bond cleavage to produce intermediate 3. Elimination of CO from 3 leads to the main products, 4 and CO. The other pathway proceeds through the ring opening, i.e., by breaking either the C2-C3 or C2-C4 bond. As noted, the ring opening requires much higher activation energy than the cyclization mechanism, in agreement with earlier studies (for references see [78]).

As shown in Figs. 10 and 11, pentacene oxyradicals I and II follow pathways similar to phenoxy radical. However, the reactions generating products 4 and CO from pentacene oxyradicals I and II are less endothermic, by 13.9 and 11.0 kcal/mol, respectively, than those of phenoxy radical. Compared with phenoxy radical, pentacene oxyradical I has a lower barrier (TS1-2) to generate intermediate 2, while oxyradical II has a higher barrier. The TS1-2 energy of the pentacene oxyradical I system is lower than that of II by 10.4 kcal/mol, which contributes to a faster decomposition rate of oxyradical I.

Similar to phenoxy radical, pentacene oxyradicals I and II each have distinct possible ring-opening pathways by breaking either of the two neighboring C-C bonds. For phenoxy radical, these two pathways are the same. However, for pentacene oxyradicals I and II, the two possible ring-opening pathways are different. One of these pathways, via TS1-5, is comparable in energy to that of phenoxy radical. The other one, via TS1-6, is much higher in energy, which makes the fate of 6 essentially unimportant.

In contrast to pentacene oxyradicals I and II, no cyclic intermediates were found for pentacene oxyradicals III and IV. A potential energy scan, in which the C3 to C4 distance was varied and other geometrical parameters allowed to relax, was performed to explore possible reaction pathways for III and IV along the reaction coordinate to form a cyclic intermediate, as shown in Fig. 12. For oxyradical III, as the two interacting carbon atoms come close to form a bond, only a local inflection point was found, indicating that a local minimum either does not exist or the potential energy well is too shallow. In the case of
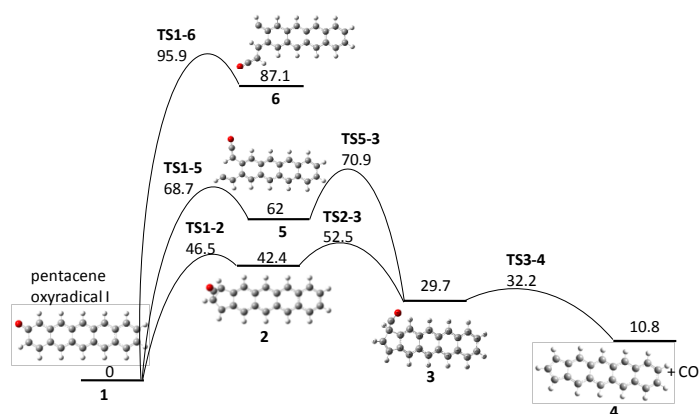
Figure 10: Minimum potential energy paths for the thermal decomposition of pentacene oxyradical I at the B3LYP/6-311G(d,p) level. Energies (in kcal/mol) at 0 K relative to reactants are shown for each transition state and local minimum.
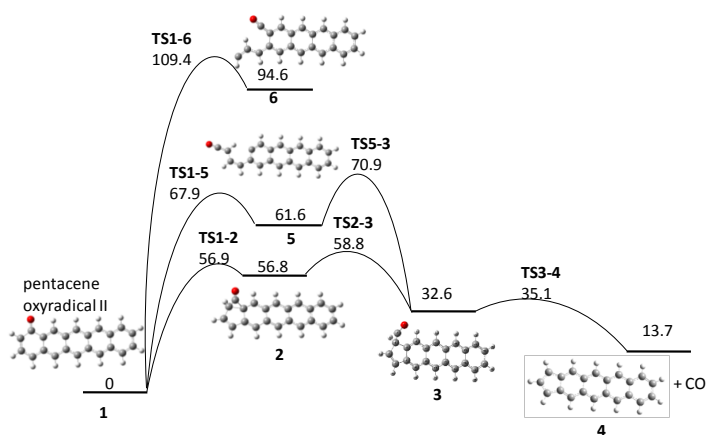
Figure 11: Minimum potential energy paths for the thermal decomposition of pentacene oxyradical II at the B3LYP/6-311G(d,p) level. Energies (in kcal/mol) at 0 K relative to reactants are shown for each transition state and local minimum.
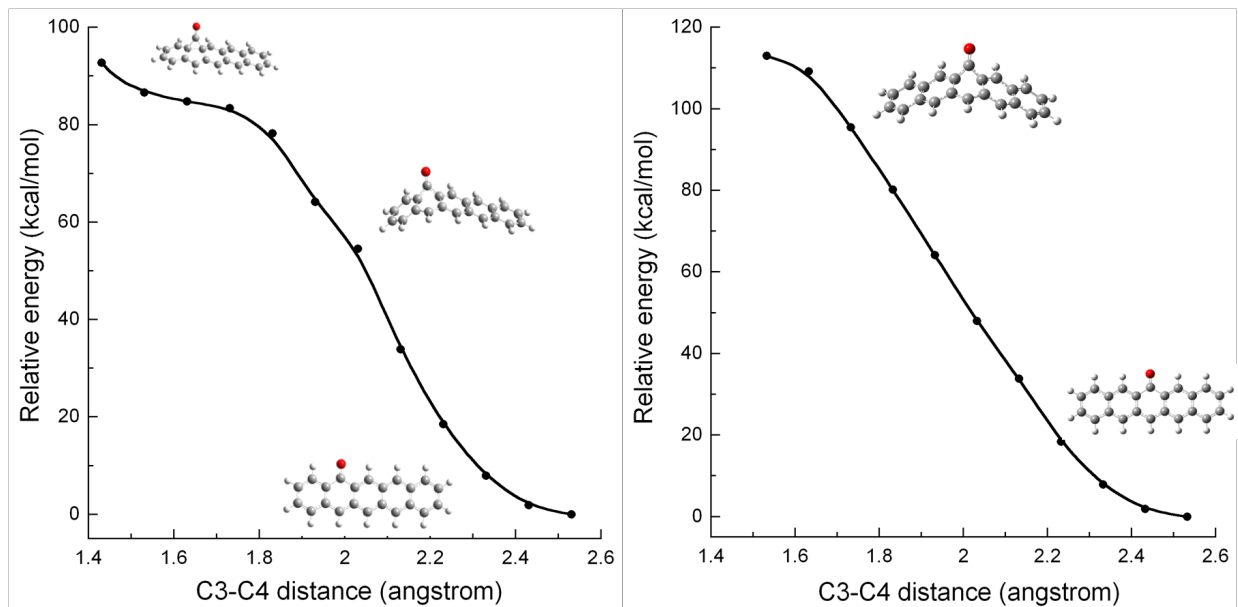
Figure 12: Relaxed potential energy scan for pentacene oxyradicals III (left) and IV (right) at the B3LYP/6-311G(d,p) level of theory.
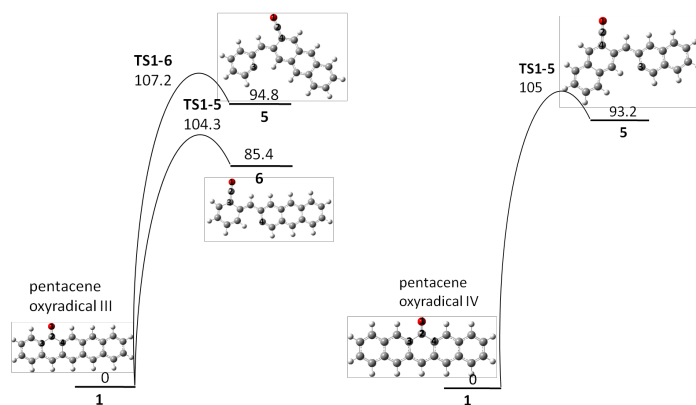
Figure 13: Minimum potential energy paths for the thermal decomposition of pentacene oxyradical III (left) and IV (right) obtained by breaking the C2-C3 and C2-C4 bonds adjacent to the C=O bonds, respectively, at the B3LYP/6-311G(d,p) level. Energies (in kcal/mol) at 0 K relative to reactants are shfown for each transition state and local minimum.

oxyradical IV, the potential energy continues to increase as the two carbon atoms get closer. Fig. 13 depicts the decomposition of oxyradicals III and IV through their respective ring-opening pathways. In both of these cases, intermediates 5 and 6 have very high potential energies relative to reactants with potential-energy barriers over 100 kcal/mol. Therefore, it is unlikely for oxyradicals III and IV to produce CO through reaction pathways similar to those of oxyradicals I and II. Furthermore, the ring-opening pathways of oxyradicals III and IV involve internal torsional rotations and therefore form non-planar molecular structures, which is unlikely to happen for multi-layer PAHs.

Based on the potential energy surfaces and the molecular properties calculated at the B3LYP/6-311G(d,p) level, we computed the rate coefficients of the thermal decomposition of phenoxy radical and the pentacene oxyradicals. For phenoxy and pentacene oxyradicals I and II, we found that the main decomposition products were carbon monoxide and species 4, and the production of other stable species was negligible for the conditions studied. Therefore, we may write the reactions as shown in Fig. 14. For pentacene oxyradicals I and II, the

(R1)

(R2)

(R3)

Figure 14: Overall decomposition reactions of aromatic oxyradicals.

ring-opening pathway through TS1-6 can be neglected as its rate coefficient is orders of magnitude smaller than that through TS1-5. Assuming intermediate species 2, 3, and 5 are in steady state, the high-pressure-limits of these rate coefficients, k_∞, can be calculated for the overall reactions R1, R2, and R3,

$$
\begin{aligned}
k_{1,\infty} &= 1.84 \times 10^7 T^{1.93} \exp\left(-25819/T\right) \text{ s}^{-1} \\
k_{2,\infty} &= 9.23 \times 10^7 T^{1.61} \exp\left(-25078/T\right) \text{ s}^{-1} \\
k_{3,\infty} &= 1.11 \times 10^7 T^{1.97} \exp\left(-29070/T\right) \text{ s}^{-1}
\end{aligned}
$$

Analysis of the computed reaction rates indicated that the cyclic pathway and the ring-opening pathway through TS1-5 both contribute to k_∞, and that the rate coefficients of steps 1→2 and 1→5 are smaller than those of the subsequent steps.

The rate coefficients at finite pressures were computed by solving the master equations using the Multiwell suit of codes, and the results are displayed in Figs. 15, 16, and 17.

To compare our results with those in the literature on phenoxy decomposition, Fig. 15 displays two sets of reported experimental results and our computed k_1 as a function of temperature and pressure. One experimental study is that of Lin and Lin [81], who investigated R1 at
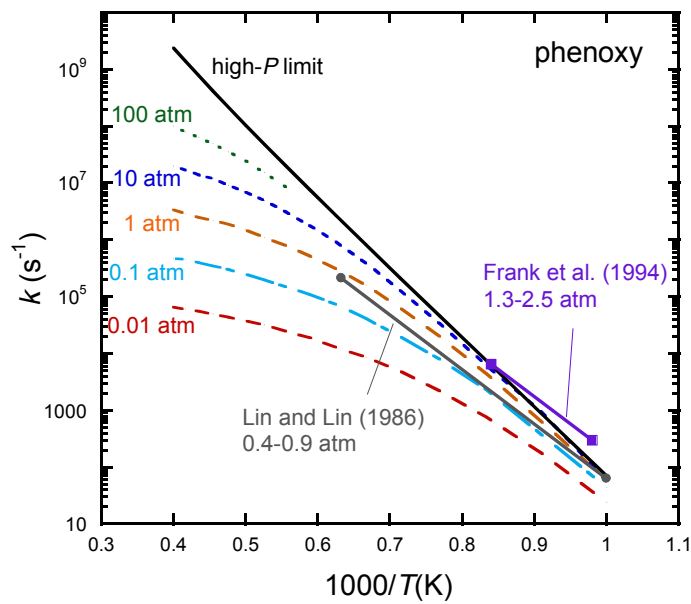
Figure 15: Comparison of computed k_1 with experimental rate coefficients.
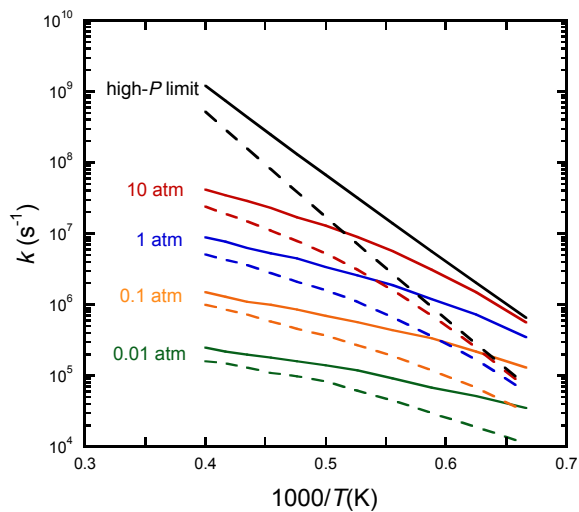
Figure 16: Rate coefficients of CO formation from pentacene oxyradicals I and II as a function of temperature and pressure. Solid lines: pentacene oxyradical I; dashed lines: pentacene oxyradical II.
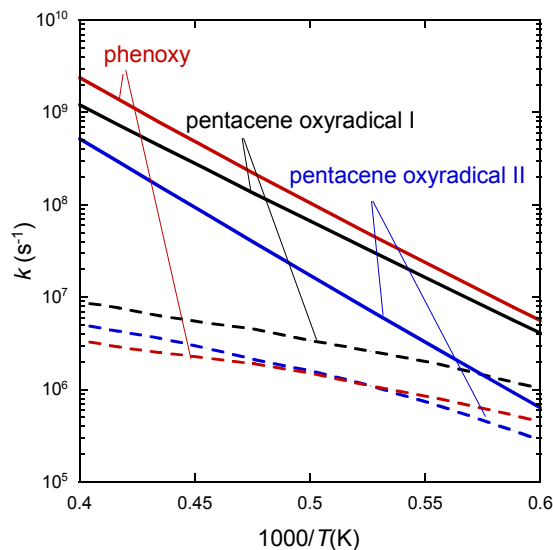
Figure 17: Rate coefficients of CO formation from phenoxy and pentacene oxyradicals I and II. Solid lines: the high-pressure limit; dashed lines: 1 atm.

1000-1580 K and 0.4-0.9 atm using anisole ($C_6H_5OCH_3$) and allyl phenyl ether ($C_6H_5OCH_2$) as precursors. These authors reported a rate coefficient of $10^{11.4\pm0.2}\exp(-22100\pm450/T)$ s^{-1}. The other experimental result comes from a shock-tube study of phenyl radicals reacting with molecular and atomic oxygen by Frank et al. [82], who determined the rate coefficient to be $7.4 \times 10^{11}\exp(-22070/T)$ s^{-1} in the range of 1020-1190 K and 1.3-2.5 bar.

Compared with the experimental studies, our computed results are within the uncertainty ranges of the measured values. This agreement can serve as validation of the present method and procedures. We note that the computed k_1 is both temperature and pressure dependent. As expected, k_1 increases as temperature or pressure rises. At relatively low temperatures, k_1 is close to the high-pressure limit, $k_{1\infty}$, when the pressure is larger than 1 atm. At intermediate temperatures, it is in the falloff region. At high temperatures, it approaches the low-pressure limit due to high internal energy at these temperatures. The pressure dependence of k_1 may explain the discrepancy between the experimental studies, since the measurements of Frank et al. [82] were carried out at higher pressures than those of Lin and Lin [81].

Figure 16 shows the computed rate coefficients k_2 and k_3 of CO formation from the decomposition of pentacene oxyradicals I and II, respectively. Similar to phenoxy radical, the deviation of the rate coefficients from their respective high-pressure limits increases with temperature. We also observe that in the temperature range of 1500-2500 K and the pressure range of 0.01–10 atm, the computed values of k_2 are 1.6 to 8.2 times those of k_3.

Figure 17 displays the rate coefficients of CO formation from the decomposition of phenoxy radical and pentacene oxyradicals I and II computed at the high-pressure limit and at 1 atm. As can be seen in Fig. 17, the rate coefficients are pressure dependent for all three

species. At the high-pressure limit, $k_{1\infty}$ is larger than both $k_{2\infty}$ and $k_{3\infty}$, while at 1 atm, k_1 is smaller than k_2 and close to k_3. The pressure dependence is weaker for the pentacene oxyradicals than for the phenoxy radical, as expected for large molecules.

The results obtained indicate that the decomposition rate is determined by the location of the oxygen atom in the pentacene oxyradicals. Oxyradicals with oxygen attached to inner rings are kinetically more stable than those with oxygen attached to outer rings. The latter can generate carbon monoxide at rates comparable to phenoxy radicals, while CO is unlikely to be produced from oxyradicals with oxygen bonded to inner rings.

The kinetics results for the zigzag edges are published in [78].

Finally, we computed decomposition rates of graphene oxyradicals whose oxygen atom is located at armchair sites, compare these rates to those at zigzag sites dicussed above. We then show that kinetic stability of oxyradicals, similar to their thermodynamic stability, is correlated with substrate aromaticity.

To study the decomposition of armchair edge oxyradicals, five molecules were selected; these structures are shown in Fig. 18. Phenanthrene oxyradicals I and II were selected
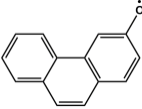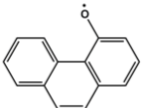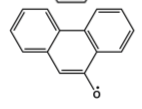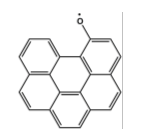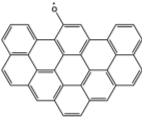
Specie name	Structure
Phenanthrene I	
Phenanthrene II	
Phenanthrene III	
Benzoperylene	
Extended-armchair	

Figure 18: Armchair oxyradical structures.

to examine the differences in decomposition rate between the two principal armchair sites. Phenanthrene oxyradical III was included to provide comparison with the previously studied zigzag site decomposition [78]. Benzoperylene oxyradical and the extended-armchair oxyradical have oxygen located on an armchair site that is the same as in phenanthrene II, but part of a larger substrate. The intent of including these larger substrates is to examine if and by

how much the decomposition rate for the same edge site changes with substrate size.

Phenanthrene oxyradicals I, II, and III decompose via similar pathways and intermediates (Figs. 19, 20, and 21).

Figure 19: Minimum potential energy paths for the thermal decomposition of phenanthrene oxyradical I at the B3LYP/6-311G(d,p) level. Energies are in kcal/mol at 0 K relative to the reactant.

The three pathways contain a cyclic intermediate 2, and all have at least one ring opening intermediate 5. For phenanthrene oxyradical I, two five-member rings with attached CO, intermediates 3 and 7, were found. For phenanthrene oxyradicals II and III, only one such intermediate, 3, was discovered. An additional channel was found for phenanthrene oxyradical II, namely TS 2-4, which connects intermediate 2 directly to product 4.

These pathways are similar to those computed for the decomposition of pentacene zigzag corner oxyradicals, which included the cyclic (2), attached-CO (3), and ring-opening (5) intermediates. Furthermore, the products of decomposition are also comparable in that all contain a five-member ring. Barrier energies of the corner-pentacene and phenanthrene oxyradical decomposition pathways are also very close to each other, often to within 3-4 kcal/mol. Such parallels in the reaction pathways indicate that the armchair-edge and corner zigzag-edge decompositions are comparable and could be classified as equivalent types of oxidation reactions.

Phenanthrene oxyradicals I, II, and III are all single row structures. To test the influence of substrate size on decomposition kinetics, the benzoperylene and extended-armchair oxyradicals were studied; both have oxygen on a site similar to that in phenanthrene II. The phenanthrene II and benzoperylene decomposition pathways, shown in Figs. 20 and 22, respectively, contain the same intermediates, but the energy of the highest transition state barrier along the lowest potential energy path (TS 1-2) is larger by 7 kcal/mol for benzoperylene. As shown below, this leads to an almost tenfold slower decomposition rate

Figure 20: Minimum potential energy paths for the thermal decomposition of phenanthrene oxyradical II at the B3LYP/6-311G(d,p) level. Energies are in kcal/mol at 0 K relative to the reactant.
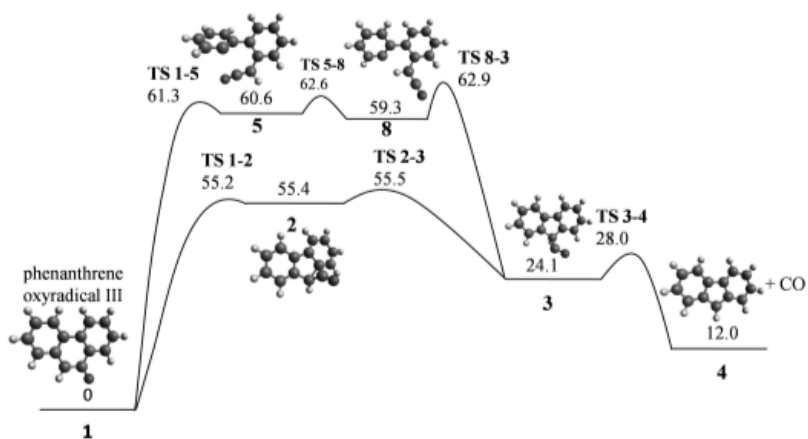
Figure 21: Minimum potential energy paths for the thermal decomposition of phenanthrene oxyradical III at the B3LYP/6-311G(d,p) level. Energies are in kcal/mol at 0 K relative to the reactant.

for benzoperylene oxyradical relative to phenanthrene II oxyradical. The extended-armchair decomposition pathway differs from the phenanthrene II and benzoperylene pathways. The extended-armchair pathway, shown in Fig. 23, does not contain the cyclic intermediate 2, but it does have the ring-opening intermediate 5. In this case, rather than proceeding from 1 to 2 to 3 as with the other structures, the extended-armchair oxyradical goes directly from 1 to 3. The difference in potential energy between the highest barrier on the lowest energy path of the extended-armchair (TS 1-3) and that of benzoperylene (TS 1-2) is 2.8 kcal/mol. This difference is counteracted by a 11.7 kcal/mol higher ring-opening barrier (TS 1-5) of benzoperylene compared to that of the extended-armchair. These opposing trends nearly cancel and, as shown in the next section, the extended-armchair and benzoperylene oxyradicals decompose at similar rates. Using the above results, reaction rates were calculated for
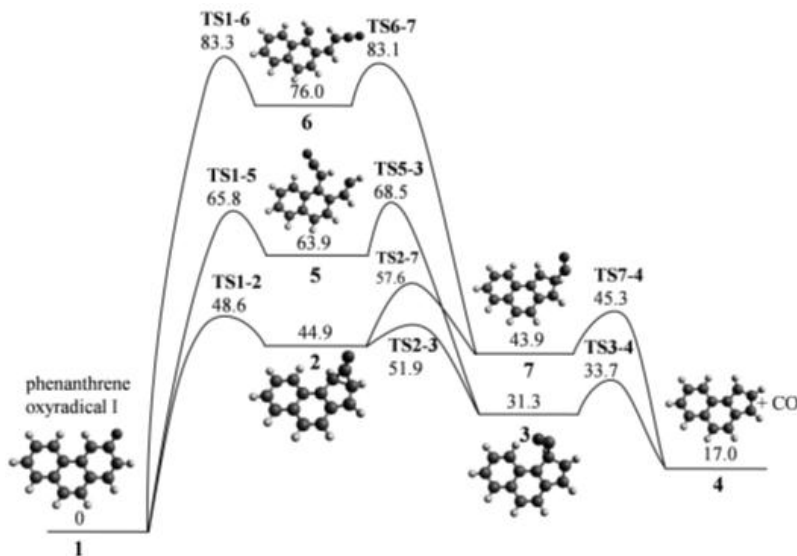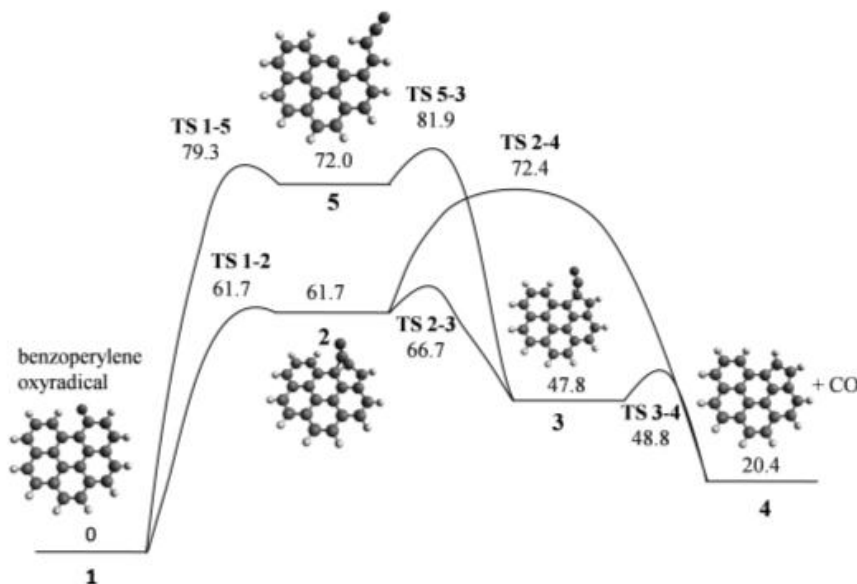

Figure 22: Minimum potential energy paths for the thermal decomposition of benzoperylene oxyradical at the B3LYP/6-311G(d,p) level. Energies are in kcal/mol at 0 K relative to the reactant.

the five reactions, shown in Fig. 24.

The principal products of oxyradical decompositions were the embedded five-member ring and CO. The accumulation of other species was negligible for the conditions studied. The rate coefficients at specific values of pressure and temperature were computed by solving the master equations using the Multiwell suite of codes. All of these reactions displayed similar pressure and temperature dependence.

In observing the pressure dependence, it was desirable to calculate the high-pressure-limit rate coefficients for each of the overall reactions R1a–R5a. To accomplish this aim, we assumed that all intermediates of an individual reaction system are in steady state. The fitted Arrhenius expressions for the high-pressure-limit rate coefficients are reported in Fig. 25.

Inspection of rate coefficients computed for the three phenanthrene oxyradicals, displayed in Fig. 26, indicates that phenanthrene I, with oxygen furthest to the outside, decomposes
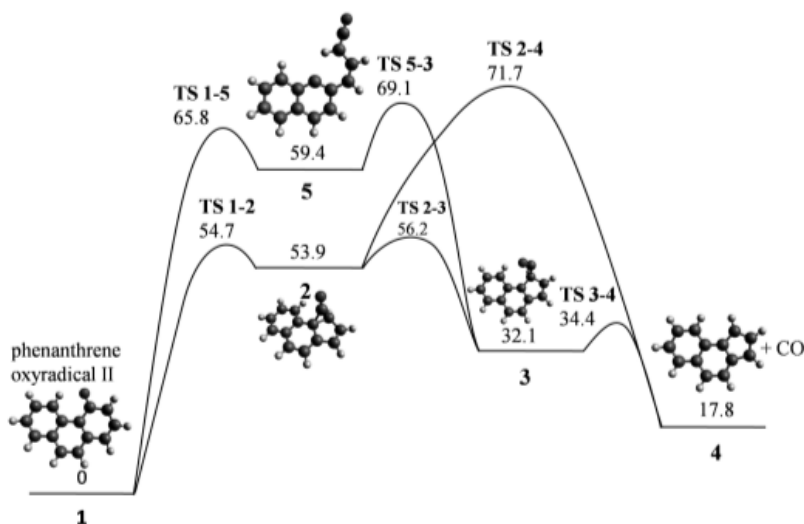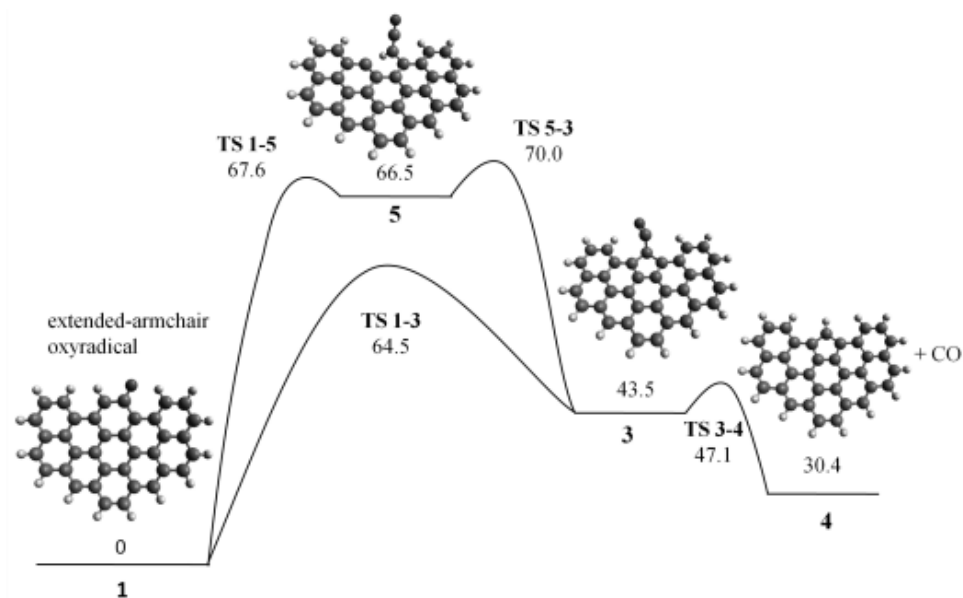
Figure 23: Minimum potential energy paths for the thermal decomposition of the extended-armchair oxyradical at the B3LYP/6-311G(d,p) level. Energies are in kcal/mol at 0 K relative to the reactant.

faster than phenanthrene II, whereas the latter decomposes about as fast as phenanthrene III. The correlation of these rates with the molecular structure of the three phenanthrene oxyradicals can be rationalized by counting "free edges", a concept introduced in Ref. 78. A "free edge" classifies the connectivity of the C-O site in the context of the multi-ring aromatic structure. For example, in phenanthrene I, C-O is connected, on both sides, to carbon atoms that are members of only one ring; we classify each of these edges as free edges. On the other hand, C-O in phenanthrenes II and III is connected on one side to a C atom that is a member of two rings, and on the other side to a C atom that is a member of one ring. Therefore, phenanthrenes II and III contain only one free edge, with the non-free edge connected to the carbon atom that is a member of two rings. Using this simple structural classification enables us to rationalize the relative ordering of the decomposition rates among phenanthrene oxyradicals I, II, and III. Phenanthrene I has two free edges and decomposes fastest, whereas II and III, each having just one free edge, decompose slower than I and at nearly comparable rates.

In Fig. 27 we compare the decomposition rates of phenanthrene II, benzoperylene, and the extended-armchair oxyradicals. Inspection of these findings indicates that the increase in substrate size, from phenanthrene to benzoperylene, substantially reduces the computed reaction rate, whereas the rate seems to level off with further increase in size, from benzoperylene to extended-armchair. The benzoperylene oxyradical decomposes nearly an order of magnitude slower than the phenanthrene II oxyradical. This is primarily due to the higher potential energy of TS1-2 in the benzoperylene pathway compared to that of phenanthrene II. Comparing the extended-armchair energetics to that of benzoperylene indicates that although the lowest energy path for the extended-armchair has a higher barrier (TS 1-3) than

39

(R1a)

(R2a)

(R3a)

(R4a)

(R5a)
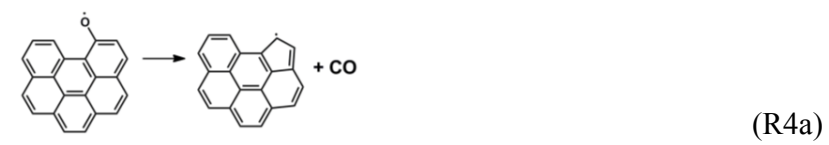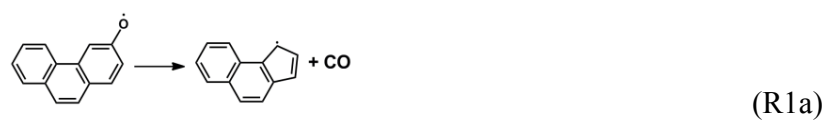
Figure 24: Overall decomposition reactions of aromatic armchair oxyradicals.

Reaction	Rate coefficient (s^{-1})
R1a	$1.08 \times 10^2 T^{3.28} \exp(-21866/T)$
R2a	$4.00 \times 10^{-2} T^{4.38} \exp(-24624/T)$
R3a	$6.42 \times 10^{10} T^{1.00} \exp(-29183/T)$
R4a	$3.78 \times 10^4 T^{2.59} \exp(-30151/T)$
R5a	$4.47 \times 10^{12} T^{0.39} \exp(-33796/T)$

Figure 25: High-pressure-limit rate coefficients.

benzoperylene (TS 1-2), it has a substantially lower barrier to ring opening, thus making its decomposition rate competitive with that of benzoperylene oxyradical decomposition. These results may indicate that a two-row graphene structures may be sufficiently large to represent an edge reaction for an arbitrarily large graphene substrate.

Comparing the decomposition rates of the armchair-edge and zigzag-edge oxyradicals highlights the resemblance between the decomposition rates of the armchair and corner zigzag edges. Figure 28 displays the decomposition rates of phenanthrene I and II as well as those of pentacene I and II from our earlier zigzag study. Focusing first on the 1-atm results displayed in Fig. 28, we see strong correlation between the phenanthrene and pentacene decomposition rates, namely phenanthrene I and pentacene I decomposition rates are very close to one another, as are the decomposition rates of phenanthrene II and pentacene II. Structurally, phenanthrene I is similar to pentacene I—both have free edges on each side of the C-O bond. Likewise, phenanthrene II structurally resembles pentacene II, with a free edge on only one side of the C-O bond. Again, the structures with the same number of free edges decompose at similar rates, and the structures with two free edges decompose faster than those with one free edge. However, at the high-pressure limit the correlation between the pentacene and phenanthrene oxyradical decomposition rates is weaker (Fig. 28). The general trend within the different types of molecules still holds, as oxyradical structures with more free edges decompose at a faster rate than those with just one free edge. This "free-edge" analysis rationalizes one of the key results of the present study, namely, that phenanthrene oxyradicals and corner pentacene oxyradicals decompose at similar rates.
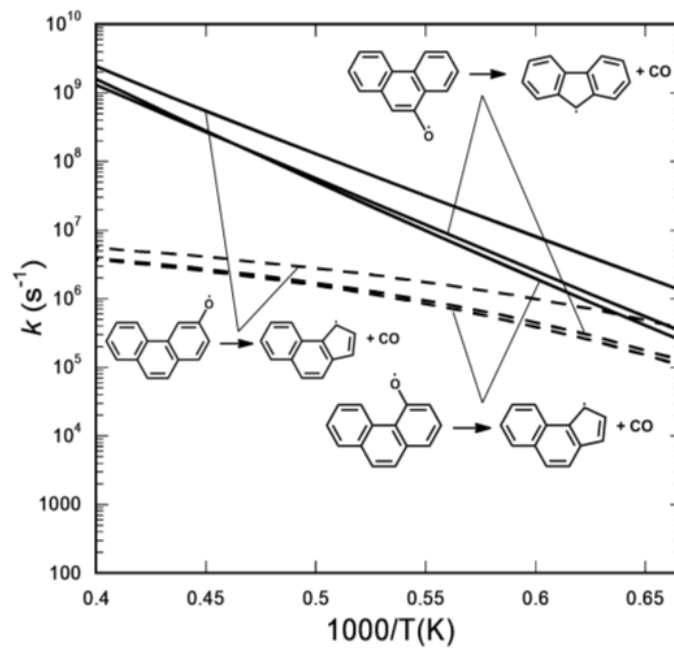
Figure 26: Rate coefficients of the decomposition of phenanthrene oxyradicals I, II and III. The solid lines are the high-pressure-limit values and the dashed lines are the rate coefficients at 1 atm.
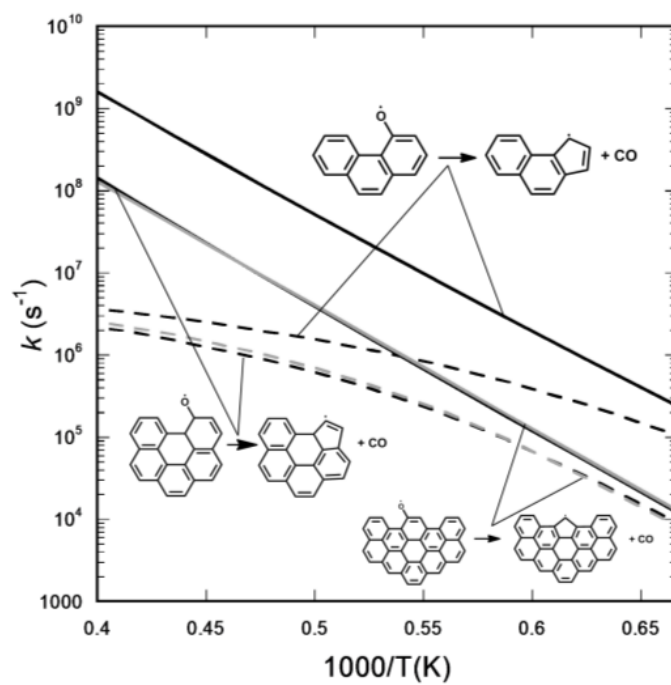
Figure 27: Rate coefficients of the decomposition of phenanthrene oxyradical II (black lines), benzoperylene oxyradical (black lines), and the extended-armchair oxyradical (gray lines). The solid lines are the high-pressure-limit values and the dashed lines are the rate coefficients at 1 atm.
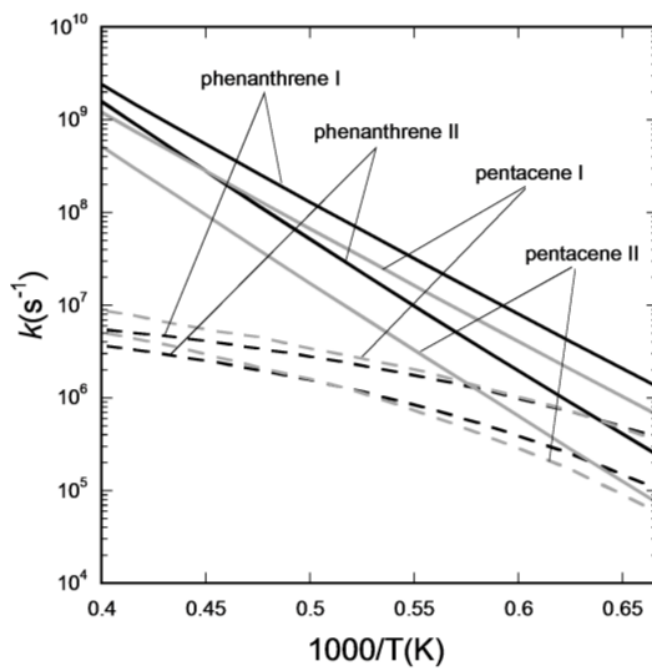
Figure 28: Rate coefficients of the decomposition of phenanthrene oxyradicals I and II (black lines) and pentacene oxyradicals I and II (gray lines). The solid lines are the high-pressure-limit values and the dashed lines are the rate coefficients at 1 atm.

We now turn to examing the correlation of the computed reaction rates with the molecular structure of the oxyradicals. Polyaromatic hydrocarbons are structurally related to the benzene molecule. This connection implies strong similarity in electronic structure that characterizes aromatic systems, namely, that of delocalized bonding. However, in the analysis of chemical properties of large PAHs studied as models of extended systems, such as soot and graphene, this connection is rarely exploited. It is reasonable to examine thermodynamic and kinetic aspects of reactivity of large PAHs on the basis of their local and global aromaticity. Such a connection can lead to formulation of simple quantitative or semi-quantitative predictive models that appeal to chemical intuition and help to rationalize structure-property relationships of the target systems—soot and graphene.

Aromaticity can be defined as the extra stabilization of a system featuring delocalized bonds with respect to a fictitious system with completely localized bonds. In practice, assessment of the resonance energy is a difficult task, especially for molecules that require multiple Kekule structures in the resonance description. Multiple measures of aromaticity have been proposed in order to simplify the task and connect the analysis to observable properties. Considering the computational challenges associated with theoretical treatment of large PAHs it appears reasonable to choose the simplest model of aromaticity that utilizes the observation that aromatic bonding is strongly associated with equalization of bond lengths due to formation of a delocalized bonding framework. In the Harmonic Oscillator Model of Aromaticity (HOMA) employed in our earlier thermodynamics study, one evaluates the mean deviation of bond lengths in a system under consideration with respect to bond lengths in benzene. It is further scaled such that HOMA = 0 for the Kekule form of benzene and HOMA = 1 for the aromatic form.

Our previous studies demonstrated that a simple correlation exists between cumulative HOMA of oxyradicals and their relative thermodynamic stability. The origin of this relationship is fragmentation of the delocalized π-bonding framework due to its disruption upon chemisorption of an O atom at a graphene radical site. It is reasonable to assume that the same reasoning applies to energetic characteristics of oxyradical decomposition. In the present case, HOMA can be used for reactivity analysis for reaction kinetics. Considering the diversity of factors controlling reaction kinetics, for example, the multiple intermediates and transition states, we narrowed the range of analyzed characteristics down to a single one, namely the relative energy of the first transition state. Barrier height is a relative value, so it is logical to consider its relationship to a relative descriptor of aromatic bonding, that can be defined as the difference between HOMA of the benzene-like ring undergoing CO expulsion of the reactant and HOMA of the transition state, i.e., $HOMA_{rel} = HOMA_{TS}$ - $HOMA_{reactant}$. A simple correlation in the data can be seen by plotting (Fig. 29) the results obtained for both zigzag and armchair cases. The smallest barrier height is associated with the smallest absolute HOMA change, thus suggesting that CO expulsion should proceed via the route that involves the smallest rearrangement of the conjugated bonding framework.

4.2   DNS Study of Soot Formation and Evolution

A DNS study was performed to provide insight into the processes controlling soot formation and growth in turbulent flames, while considering state-of-the-art chemistry and soot models developed under this project. A two-dimensional turbulent nonpremixed flame sub-
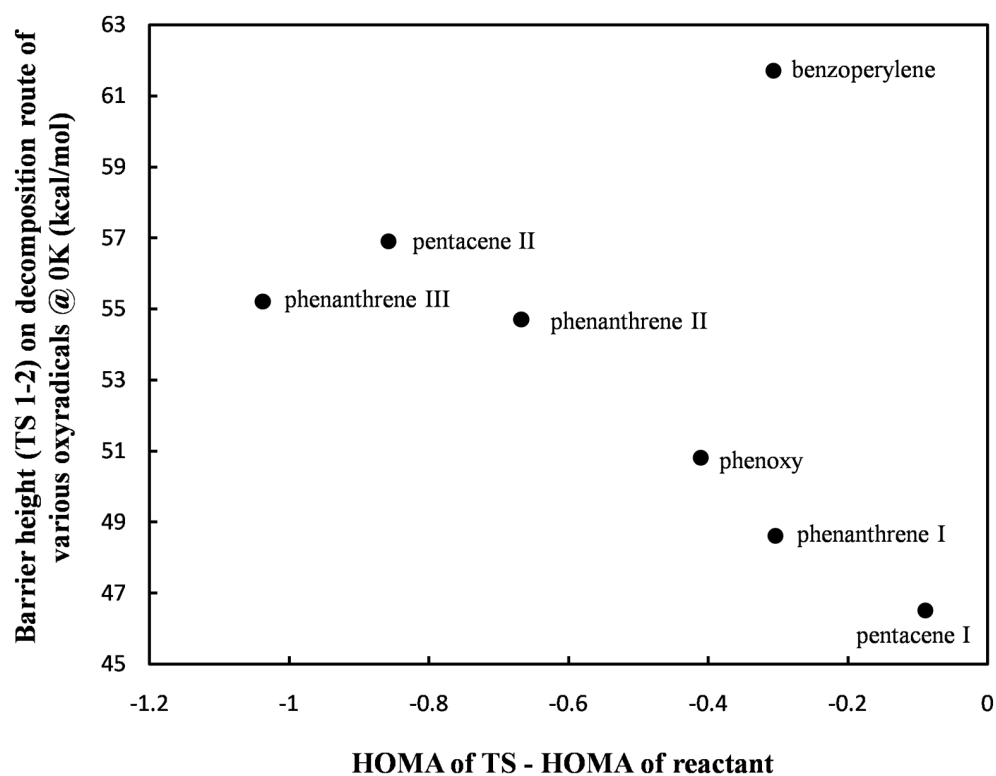
Figure 29: First barrier heights of oxyradical decompositions against relative HOMA of respective transition states (TS 1-2).

ject to decaying isotropic turbulence was selected to make the simulation computationally tractable. This study distinguishes it- self from previous work [28, 29] by considering finite rate chemistry from fuel oxidation to the formation of PAH and a detailed soot model based on elementary physical processes and rates rather than using a semi-empirical approach. Finite rate chemistry allows for the investigation of the effect of turbulent mixing on the formation and yield of key soot precursors such as acetylene and naphthalene.

The complete formulation of the flow governing equations and simulation numerical methods used in the DNS are provided in Ref. 24, but are omitted here to focus more directly on the study's implications for LES modeling.

The detailed chemical mechanism used to generate the LES flamelet tables (see Sec. 3.3) must be reduced to be feasible for finite rate chemistry computations. A multi-step approach combining automatic and manual reduction techniques was used to reduce the size of the chemical mechanism and make it more affordable for DNS. Throughout the reduction process, emphasis was placed on accurately predicting the combustion characteristics of both n-heptane (C_7H_{16}) and toluene (C_7H_8), two major components typically found in surrogate fuel formulations. The final reduced mechanism contains only 47 species and 290 reactions. It was validated against a series of laminar test cases, including laminar burning velocities, a rich premixed flame, and a diffusion flame. Soot was modeled using the approaches described in Sec. 3.2.1.

4.2.1 Initial Conditions and Simulation Parameters

The two-dimensional computational domain consists of a square of size L. Periodic boundary conditions are applied in both the horizontal (x) and vertical (y) directions, effectively resulting in a constant volume system. At the onset of the simulation, a horizontal strip of fuel is surrounded by oxidizer. The fuel stream consists of n-heptane diluted with 84.4% (by volume) nitrogen at a temperature of 300 K. The oxidizer stream consists of air (21% oxygen and 79% nitrogen) also at 300 K. The significant nitrogen dilution in the fuel stream is necessary to reduce peak soot volume fraction to a level for which radiative heat transfer from soot particles and its effect on the gas- phase can be safely neglected. The compositions of fuel and oxidizer yield a stoichiometric mixture fraction $Z_{st} = 0.143$. The stoichiometric scalar dissipation rate at extinction for the two streams (at 300 K and 1 atm) is 175 s^{-1}, computed in a counterflow geometry employing the reduced mechanism. The background pressure, initialized at 1 atm, increases to approximately 2 atm towards the end of the simulation due to heat release. Given the modest increase in pressure during the simulation, pressure effects are not expected to play any significant role in the physical processes of interest.

The reactive scalar fields are initialized as follows. Temperature and chemical species mass fractions are taken from a representative one-dimensional flamelet solution and mapped from mixture fraction space onto the vertical coordinate according to a specified hyperbolic tangent mixture fraction spatial profile. The one-dimensional flamelet solution is obtained at a prescribed stoichiometric scalar dissipation rate $\chi_{st} = 60$s^{-1}, corresponding to approximately one third of the extinction conditions. The velocity field is initialized with isotropic turbulence fluctuations of a prescribed spectrum and Re$_\lambda = 170$ at the start of the simulation. Additionally, no soot is present in the domain at time zero.
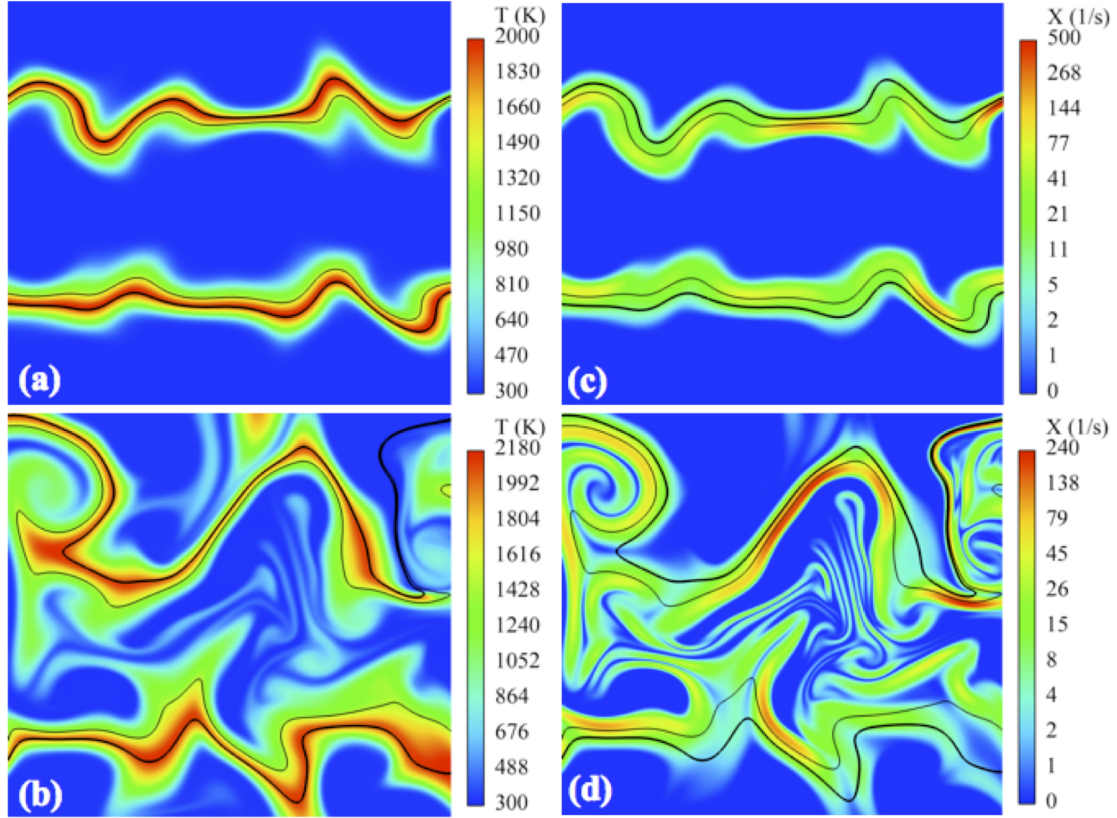
Figure 30: Scalar fields of temperature (a,b) and scalar dissipation rate in logarithmic scale (c,d) at 1.5 and 10 ms (top to bottom). The thick solid black line indicates the stoichiometric iso-contour, while the thin black line indicates the $Z = 0.3$ iso-contour.

Notwithstanding the two-dimensional treatment of turbulence, the chosen computational configuration and parameters are a reasonable approximation of the dynamics and turbulence scales characteristic of soot formation in the near field of a low Reynolds number nonpremixed turbulent jet flame.

4.2.2 Turbulent Flame Dynamics

Due to the strong dependence of soot growth on flame parameters such as temperature, equivalence ratio, and strain rate, turbulence/chemistry interaction is investigated first. Turbulent fluid motion wrinkles the flame and causes the stoichiometric contour to curve and stretch throughout the do- main. Instantaneous snapshots of temperature and scalar dissipation rate at times 1.5 and 10 ms are shown in Fig. 30.

Scalar dissipation rate is distributed spatially in thin, elongated layers. A few locations along the flame display significant weakening and extinction due to high scalar dissipation rate ($\chi_{max} \approx 490s^{-1}$ at 1.5 ms). For instance, local extinction can be observed at 10 ms in the top right corner of the domain, where the stoichiometric iso-contour passes through a region of low temperatures. At locations where flame extinction occurs, the mass fraction of OH drops from its peak value of 3.6×10^{-3} to negligible amounts (not shown).
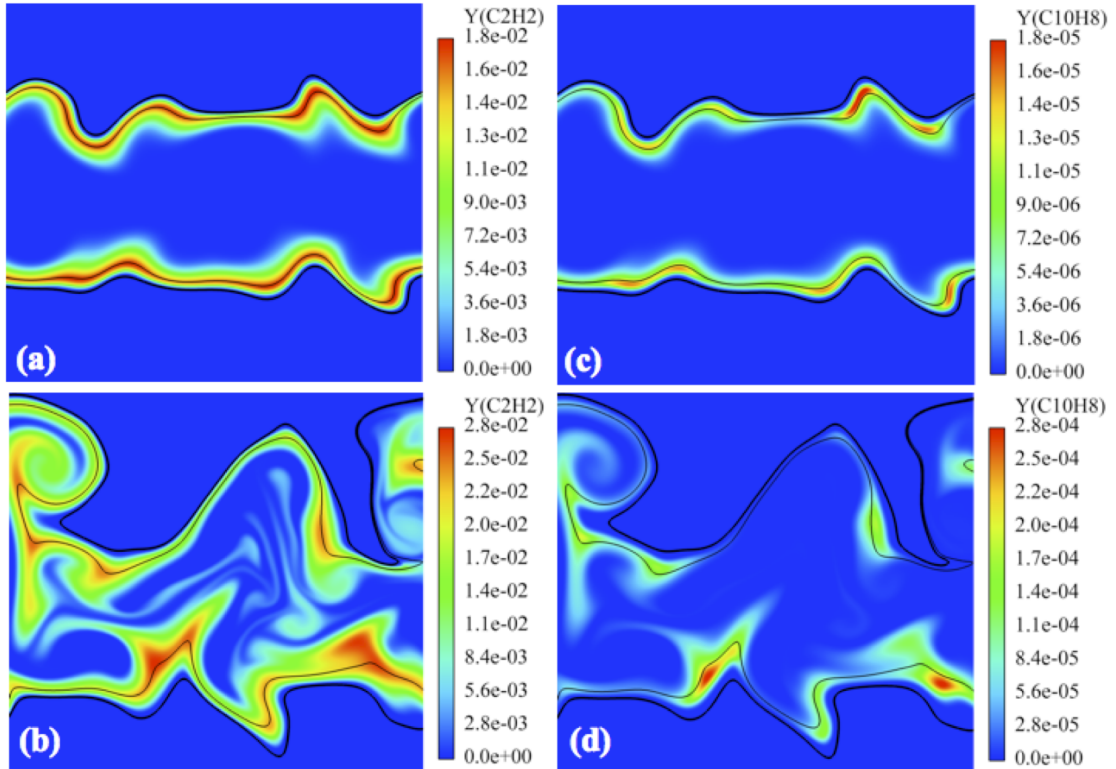
Figure 31: Scalar fields of acetylene (a,b) and naphthalene (c,d) at 1.5 and 10 ms (top to bottom). The thick solid black line indicates the stoichiometric iso-contour, while the thin black line indicates the $Z = 0.3$ iso-contour.

In the soot model used in this work, two species have significant impact on soot yield, namely naphthalene and acetylene. The concentration of naphthalene ($C_{10}H_8$) governs the rates of nucleation and condensation, while the concentration of acetylene (C_2H_2) is used in evaluating the growth rate by surface reactions. Figure 31 shows acetylene and naphthalene mass fractions at times 1.5 and 10 ms. Compared to temperature, the mass fractions of naphthalene and acetylene are affected more significantly by turbulence and by spatial and temporal variations in the scalar dissipation rate. At 10 ms, the mass fraction of naphthalene is highest in regions of low scalar dissipation rate, giving rise to concentration patches away from the flame, along the $Z = 0.3$ iso-contour. The mass fraction of acetylene also responds to changing values of scalar dissipation rate, displaying similar spatial patterns. However, the sensitivity of acetylene to turbulent stretching appears to be less pronounced than for naphthalene.

To better analyze the effects of scalar dissipation rate on the yield of acetylene and naphthalene, the DNS results are compared to the solutions of the steady flamelet equations and are shown in Fig. 32. The data are sampled from the DNS calculation at 5 ms and along the $Z = 0.3$ iso-contour. The $Z = 0.3$ location was chosen as it corresponds to the peak mass fraction for both acetylene and naphthalene as found in the one-dimensional flamelet calculations. For comparison, the one-dimensional flamelet calculations were performed with the same assumptions used for the DNS (e.g. unity Lewis number, no Soret and Dufour effects, etc.) and the same reduced chemical mechanism. The background pressure is taken to be that of the DNS at 5 ms (1.19 bar).

Even in the absence of turbulent fluctuations, the mass fraction of naphthalene displays a significantly stronger sensitivity to scalar dissipation rate compared to acetylene. With the exception of the data points at low values of scalar dissipation rates, the one-dimensional flamelet solution describes well the dependence of the mean peak mass fraction on scalar dissipation rate shown in the DNS data.

While the dependence of peak mass fraction on scalar dissipation rate observed in the DNS data is described well by the steady flamelet solution, significant scatter exists around the mean values. The magnitude of the deviation is much larger for naphthalene than for acetylene. This scatter may be explained by the rapidly changing turbulent flow field and the slowly adjusting chemical species. Furthermore, the flamelet solution at low scalar dissipation rate overestimates the mass fraction of both naphthalene and acetylene. The difference is due to unsteady flamelet effects, which are known to be more pronounced at low scalar dissipation rate [83]. The results show that naphthalene exhibits much stronger unsteady effects than acetylene, due to the slower chemistry of naphthalene (lower Damkohler number). A similar behavior is expected for PAH larger than naphthalene.

4.2.3   Soot Dynamics and Morphology

The emphasis of the present work is identifying the key mechanisms of soot growth as well as characterizing the effects of turbulent mixing on the evolution of soot. The morphology of soot particles is investigated also by focusing on aggregate properties such as the primary particle diameter and the number of primary particles.
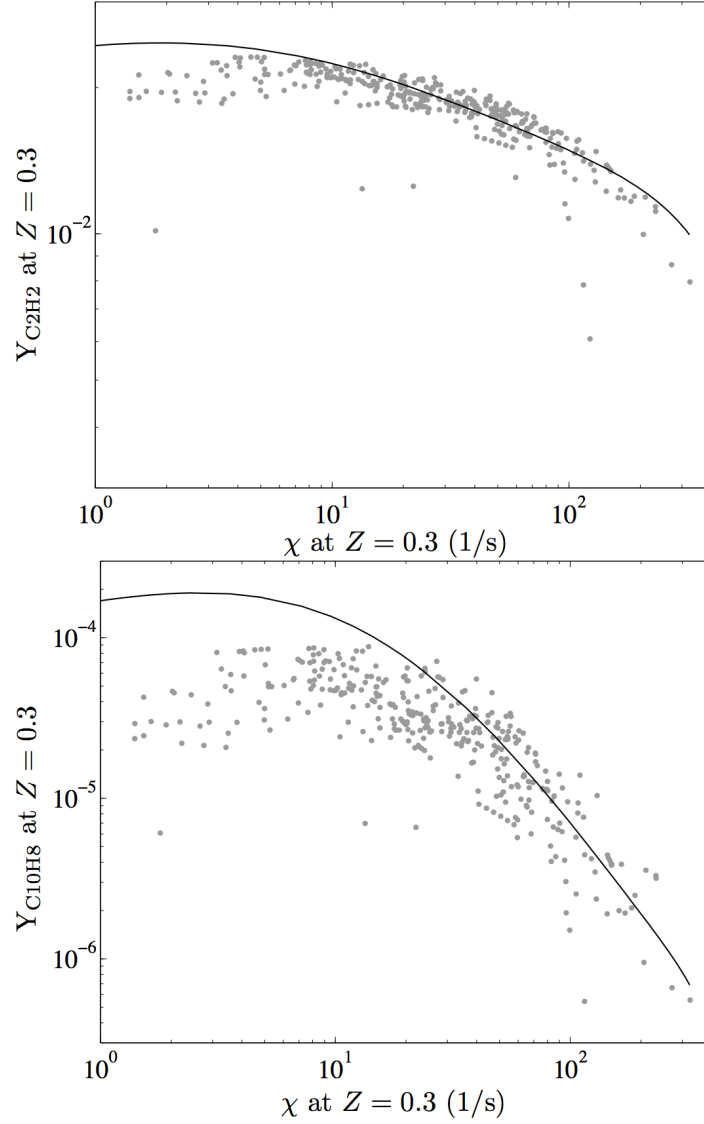
Figure 32: Mass fraction of acetylene and naphthalene as a function of scalar dissipation rate. Samples taken at $Z = 0.3$. DNS data sampled at 5 ms. Acetylene (top); naphthalene (bottom): —— steady flamelet solution; ● , DNS data.

4.2.3.1 Soot evolution overview Figure 33 shows instantaneous snapshots of soot number density and soot volume fraction fields taken at 10 and 15 ms. The spatial distribution of soot exhibits two distinct patterns: (a) small islands/patches of large values of soot number density and volume fraction; and (b) sharp fronts and filament-like patterns. While the islands appear to accumulate preferentially along the $Z = 0.3$ iso-contour, the filaments penetrate deep into the fuel stream, marking the edges of eddies. The number and length of the filaments increase with time as turbulent eddies stretch soot patches across the domain in the absence of diffusive transport. Due to the high Schmidt number (or low mass diffusivity) typical of soot transport, soot particles do not diffuse, and their transport is controlled mostly by convection and to a much lesser extent by thermophoresis.

Soot begins nucleating on the rich side of the flame sheet at a location where naphthalene abounds ($Z \approx 0.3$). From the onset of the simulation and up to 5 ms, the rate of increase of soot mass is dominated by the nucleation of spherical soot particles. At early times, soot consists of a large number of small, spherical particles, and the soot particle size distribution is monodisperse. The mean diameter and number of primary particles at 1.5 ms are spatially homogeneous and equal to 0.98 nm and 1, respectively (not shown). Meanwhile, naphthalene dimers condense on the surface of existing particles. During the simulation, the overall rate of condensation increases as existing particles grow and more surface becomes available. At 10 ms, condensation emerges as the physical process contributing most to soot mass growth. Intense growth occurs in regions of high concentration of naphthalene and low scalar dissipation rate as is evident by comparing visually Fig. 31(d) and Fig. 33(c). For instance, at 10 ms, a patch of naphthalene mass fraction appears near the bottom left corner of Fig. 31(d) where there is a peak in soot volume fraction (see Fig. 33(c)). The patch-like soot patterns observed in the domain are identified as regions of naphthalene-based soot growth at locations of low scalar dissipation rate.

The patch-like structure of soot and PAH provides insight into the process physics and its modeling. From a physical perspective, the sensitivity of PAH species to hydrodynamic strain and unsteady scalar dissipation rate indicates that turbulent mixing in technical combustion devices can lead to soot growth suppression, while having limited effect on the fuel oxidation chemistry. Based on the results presented, the dependence of soot yield on the mixing rate can be explained by the sensitivity of PAH to scalar dissipation rate. Hydrodynamic strain effects are expected to be particularly important for nonpremixed and low-temperature premixed flames. A lesser sensitivity of soot growth rates to strain is expected for high-temperature premixed flames due to surface reactions being the dominant growth process. Surface growth rates depend on the concentration of acetylene, which is less sensitive to strain. From a modeling perspective, soot growth models that rely on smaller hydrocarbon species as a proxy for large PAH molecules ignore or misrepresent the effects of turbulent mixing and hydrodynamic strain on soot formation due to differences between the Damkohler number of small and large hydrocarbon species. For example, acetylene is often used as an indicative critical species in the soot formation process in order to simplify the treatment of gas phase chemistry. As shown in this work, the sensitivity of acetylene to turbulent mixing is significantly less pronounced than naphthalene. Therefore, the application of a soot model relying on acetylene-based mass growth to a configuration for which PAH-based growth is the dominant growth route will misrepresent the effect of hydrodynamic strain on the overall soot yield.
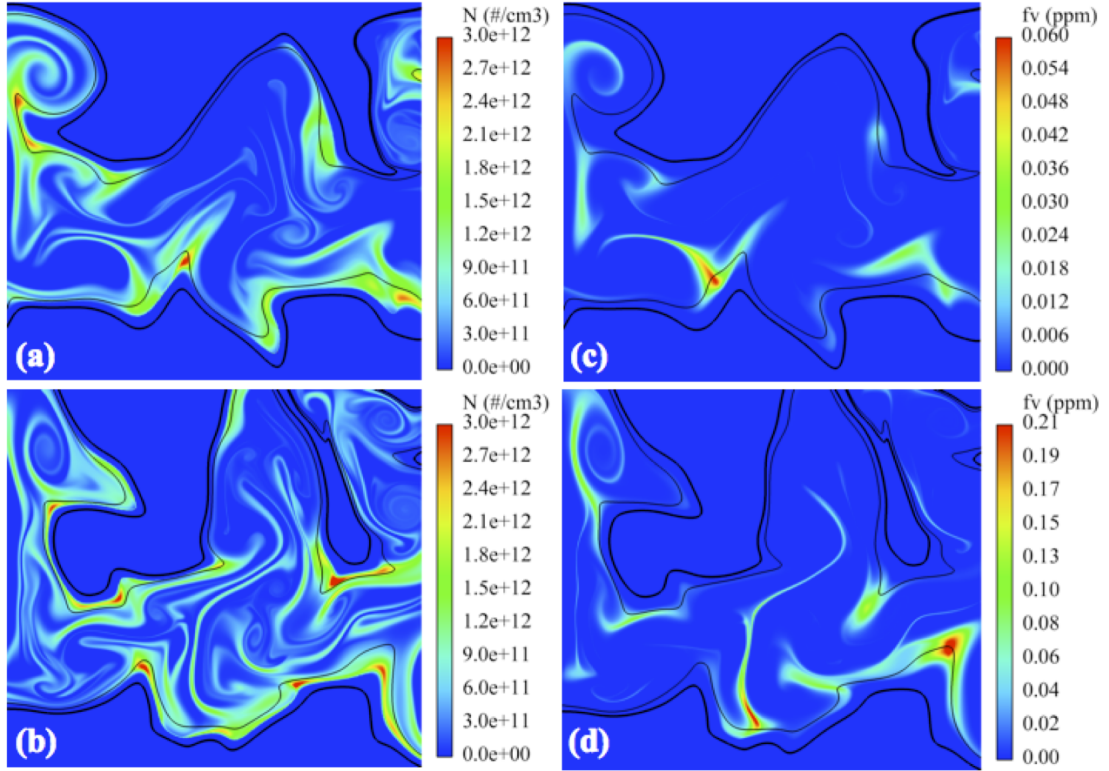
Figure 33: Scalar fields of soot particle number density, N (a,b) and soot volume fraction, f_v (c,d) at 10 (top) and 15 ms (bottom). The thick solid black line indicates the stoichiometric iso-contour, while the thin black line indicates the $Z = 0.3$ iso-contour.
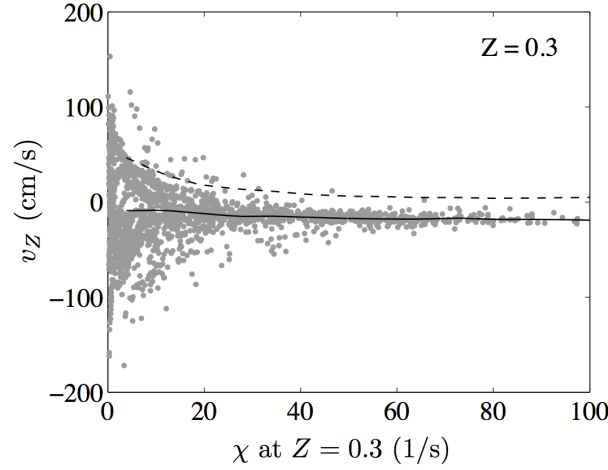
Figure 34: Conditional statistics of the displacement speed v_Z along the $Z = 0.3$ iso-contour versus the local scalar dissipation rate at 15 ms. ▬ mean; ▪▪▪▪ standard deviation; ● data.

4.2.3.2 Soot transport and growth processes Soot growth and oxidation rates are a function of temperature and mixture composition. While local mixture fraction determines nucleation, con- densation, and oxidation rates, it provides limited information about quantities such as soot number density and volume fraction. This is due to soot experiencing significant motion in mixture fraction space because of differen- tial diffusion effects among soot and gas-phase species. Differential diffusion effects are important in soot transport and were first discussed and analyzed by Pitsch et al. [84]. In a simple candle flame, differential diffusion causes soot to be transported towards the flame sheet where it is oxidized. This process is similarly responsible for soot burnout in diesel engines and aircraft engine combustors.

A convenient description of the motion of a mixture fraction (Z) iso-surface relative to fluid convection is provided by the iso-surface displacement velocity $\mathbf{v}_Z$. The scalar quantity v_Z is called the iso-surface displacement speed and takes both positive and negative values. Due to negligible mass diffusivity, soot particles are convected with the flow, and the displacement speed describes the movement of soot relative to a given mixture fraction iso-contour. Thermophoresis contributes to the movement of soot in mixture fraction space also. However, for the conditions of the present DNS, we find that thermophoretic velocities normal to the $Z = 0.3$ iso-contour remain well below 3 cm/s and are thus neglected.

Figure 34 shows the displacement speed v_Z versus scalar dissipation rate χ_Z along the $Z = 0.3$ iso-contour, which corresponds approximately to the location of peak soot growth rates and soot volume fraction for the chosen stream compositions. The data are sampled at the end of the simulation (15 ms). Two distinct regimes can be identified. At locations of low scalar dissipation rate, the absolute value of the displacement speed is largest and displays both negative and positive values. On the contrary, in regions of high scalar dissipation rate, the displacement speed is lowest and mostly negative. The mean displacement speed conditioned on scalar dissipation rate is constant across the range of scalar dissipation rates observed. Mixing reduces the peak mixture fraction value and the fraction of positive
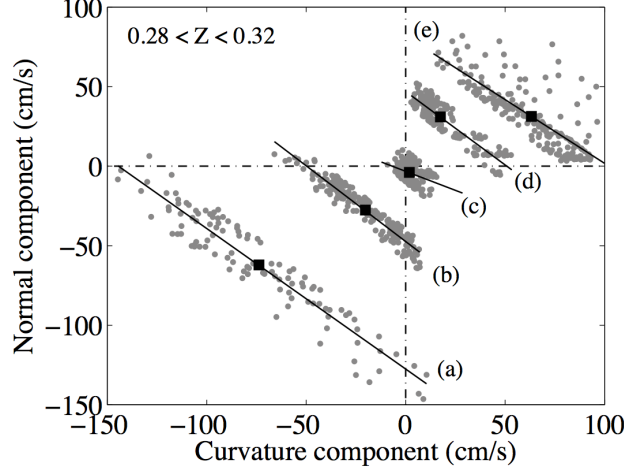
Figure 35: Statistics of the curvature and normal components of the displacement velocity. The data are sampled along mixture fraction iso-contours $0.28 < Z < 0.32$ at 15 ms. The solid lines are linear least square fits to five sets of data, binned according to the value of the displacement velocity: (a) $160 < v_Z < 140$, (b) $60 < v_Z < 40$, (c) $10 < v_Z < 10$,(d) $40 < v_Z < 60$, (e) $80 < v_Z < 100$ (cm/s). For each set, the mean values of the two displacement velocity components is indicated by a solid square.

displacement speed increases as soot is convected towards the flame sheet.

In order to better understand the spatial distribution of the displacement speed, it is written as the sum of a curvature term κ, proportional to the iso-contour curvature, and a normal term, proportional to the spatial derivative of the mixture fraction gradient along the normal.

Figure 35 illustrates the contribution of the two terms contributing to the overall displacement speed. The data are binned with respect to the resulting displacement speed to highlight the relative importance of the two terms for a given value of v_Z. Except in the case of very small values of the displacement speed, the curvature and normal terms have the same sign and act synergistically. This fact allows to judge the sign of the displacement speed from the sign of the curvature or normal component alone. Also, the mean values of the two components are similar, indicating that (on average) they contribute equally to the resulting displacement speed. Finally, at locations where the curvature term is the largest in the domain, the normal term is negligible. Hence, at locations of maximum iso-contour curvature, the displacement speed is solely due to the curvature component.

Based on the data presented, we conclude that soot particles in regions of positive iso-contour curvature (center of curvature on the lean side of the iso-contour) move towards richer mixtures (negative displacement speed); the opposite occurs for soot particles in regions of negative curvature and positive displacement speed.

An important connection between soot volume fraction and iso-contour curvature is established by the correlation between curvature and scalar dissipation rate along the $Z = 0.3$ iso-contour. The data are shown in Fig. 36 where a negative correlation between curvature and scalar dissipation rate is apparent: regions of high curvature are characterized by low scalar dissipation rate. Due to the sensitivity of PAH to scalar dissipation rate, regions of
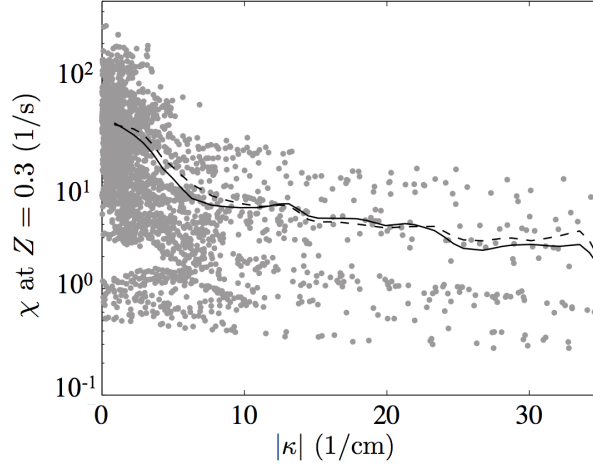
Figure 36: Statistics of scalar dissipation rate conditioned on the absolute value of the iso-contour curvature at 15 ms. ▬ mean; ▪▪▪▪ standard deviation; ● data. The data are sampled along the $Z = 0.3$ iso-contour.

high curvature are characterized by sustained soot nucleation and growth and (eventually) the highest soot volume fraction (see Fig. 37). The mean soot volume fraction along three iso-contours around the location of peak growth ($Z = \{0.23, 0.26, 0.3, 0.34\}$) increases for increasing absolute value of the curvature, reaching a minimum at zero curvature. The mean soot volume fraction profiles are approximately symmetric for positive and negative curvatures. A small, but obvious bias in favor of positive curvature and negative displacement speed appears as the data are sampled along increasingly rich iso-contours.

Due to the symmetry in the statistics of the displacement speed at low scalar dissipation rate, movement towards leaner or richer compositions is almost equally likely. The displacement direction established by the sign of the iso-contour curvature determines the subsequent soot evolution. Soot moving towards the flame (negative curvature) first grows by surface reaction via the HACA mechanism at locations of high temperature and acetylene concentration. As the displacement continues, soot is oxidized near the flame sheet. The occurrence of surface growth followed by oxidation at the flame sheet was first described by Pitsch et al. [84] in the context of unsteady flamelets and recently demonstrated in two DNS studies of turbulent sooting flames [28, 29].

Due to the inverse correlation between curvature and scalar dissipation rate, the most rapid displacement in mixture fraction space occurs at locations where abundant PAH species generate the highest values of soot volume fraction. The correlation between high values of soot growth rates and pronounced differential diffusion motion in Z-space explains the observed soot distribution and growth patterns in mixture fraction space. First, soot nucleates around $Z = 0.26$ in regions of low scalar dissipation rate. Soot particles in those regions characterized by positive curvature are displaced towards richer mixtures. During this relative motion, mass growth continues sustained by PAH species condensation on soot particles. Growth by condensation eventually surpasses growth by nucleation as more soot surface becomes available. Since the concentration of naphthalene decreases monotonically for $Z > 0.26$, soot growth rates decrease as the aggregates are displaced further towards richer

56
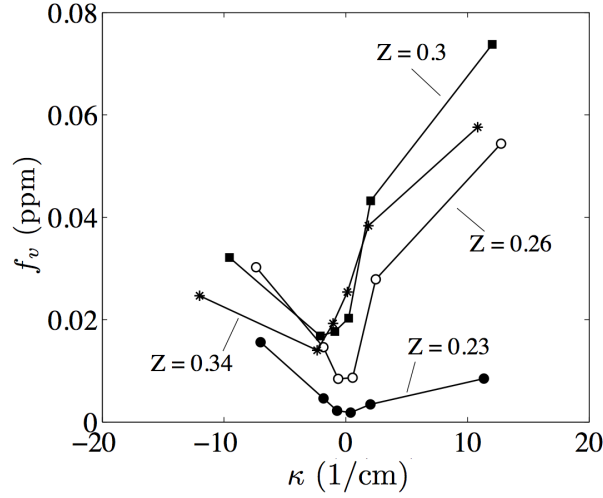
Figure 37: Mean soot volume fraction along four mixture fraction iso-contours ($Z = \{0.23, 0.26, 0.3, 0.34\}$) conditioned on the local value of the iso-contour curvature. Data sampled at 15 ms.

mixtures and cross the $Z = 0.3$ iso-contour. Soot volume fraction peaks approximately at $Z = 0.31$, i.e. at richer conditions than those of peak nucleation and peak condensation due to a drift in mixture fraction space caused by differential diffusion. On average, soot growth due to surface reactions is maximum at $Z = 0.23$, i.e. at mixture compositions leaner than those characteristic of peak nucleation.

Despite the movement of soot in mixture fraction space being nearly symmetric, the spatial distribution of soot volume fraction is significantly biased towards the fuel stream due to higher PAH-based growth rates at rich mixtures and an oxidizing environment next to the flame sheet.

4.3 LES Model Validation and Simulation Results

4.3.1 Validation Case: Delft Flame III

The configuration that will be used to validate the model is Delft Flame III [85], a piloted turbulent nonpremixed jet flame fueled by commercial natural gas. At the burner exit, a 6 mm diameter fuel jet is surrounded by a primary annular coflow of air with an inner diameter of 15 mm, which decreases from 30 mm over the last 60 mm of the burner, and an outer diameter of 45 mm. The flame is stabilized by twelve small pilot flames arranged in a ring which emanate from the rim separating the fuel stream from the primary air. These pilot flames are part of an insert in the fuel tube which causes the fuel jet diameter to decrease from 8 mm at a location 16 mm upstream of the burner exit. The bulk velocity of the fuel stream is 21.9 m/s giving a jet Reynolds number of roughly 8200 based on the fuel jet diameter and bulk velocity. The bulk velocity of the primary air stream is 4.4 m/s, and the coflow velocity is 0.3 m/s.

Several experimental campaigns have been carried out with the burner, and three of these

datasets will be used for validation in this work. Two-component velocity measurements were made with Laser Doppler Anemometry (LDA) by Stroomer [1]. Subsequent measurements of the thermochemical scalars were made by Nooren *et al.* [2] using the Raman-Rayleigh-LIF (Laser Induced Fluorescence) technique. These measurement were confined to a region closer to the burner where soot is not present. Further downstream, the soot volume fraction was measured using Laser Induced Incandescence (LII) by Qamar *et al.* [3].

Since the measurements were made in three different places, the composition of commercial natural gas was not exactly the same. In the latter two studies [2, 3], the natural gas was diluted with N_2 to match the adiabatic flame temperature of the first study. In this work, the fuel composition from the soot volume fraction measurements will be used. However, analysis has shown that the results of this work are not sensitive to a specific fuel composition.

4.3.2 Computational Implementation

The models presented in the previous section are implemented in NGA, a structured finite difference code for low Mach number turbulent reacting flows that was initially developed at Stanford. The code is based on the numerical methods of Desjardins *et al.* [86]. In this work, the momentum and continuity equations are discretized with second order spatial operators. The scalar equations required in the presumed PDF approach are spatially discretized with a bounded QUICK scheme [87]. All of the subfilter stresses and fluxes are closed with the dynamic model [88–90] with Lagrangian averaging [91, 92]. In order to accommodate the large four-dimensional tables required for the RFPV and soot models, the code has been parallelized using a hybrid method with one Message Passing Interface (MPI) process per cluster node and several OpenMP threads per node.

In order to generate the boundary conditions for the simulation, two additional smaller simulations are first performed. First, a fully developed pipe/annulus flow is computed for the burner upstream of the exit region. Second, the results of this simulation are used as inflow conditions for a simulation of the last few centimeters of the burner where the geometries of the primary air annulus and fuel jet change. The results of this second simulation are then used as inflow conditions for the main flame simulation. The secondary air co-flow is prescribed as a bulk flow. The pilot geometry is modeled as an annulus rather than twelve individual streams to preserve axisymmetry, and the inflow velocity is specified as a bulk flow. The pilot velocity is reduced (since the pilot area is larger) such that the mass flow rate matches the experiment and was found to be sufficiently strong to keep the flame attached to the burner. The reduced pilot velocity has an additional benefit of allowing a large timestep to be taken, which is absolutely vital since soot in the downstream region of the flame evolves very slowly.

The computational domain is discretized with 384, 192, and 64 points in the axial, radial, and circumferential directions, respectively. The domain is decomposed with 96 processors with a total computational cost of about $8.5\,\text{s}/\mu\text{s}$. Statistics are collected over a period of approximately $O\,(450\,\text{ms})$ for a total computational cost of roughly $O\,(100{,}000\,\text{cpu-hrs})$.

Figure 38: Radial profiles of the Favre-averaged axial velocity. The axial locations are indicated. Lines are the LES, and symbols are the experimental measurements of Stroomer [1].

Figure 39: Radial profiles of the Favre-averaged mixture fraction. The axial locations are indicated. Lines are the LES, and symbols are the experimental measurements of Nooren *et al.* [2].

4.3.3 Presumed PDF Method Results

4.3.3.1 Upstream Results: Velocity and Scalars   In this section, the LES results are compared to the experimental velocity and scalar measurements upstream where soot is not present [1, 2]. In addition to the soot model, this work is also the first LES of Delft Flame III. Where appropriate, results of previous studies of Delft Flame III utilizing RANS will be discussed. While accurate predictions of the velocity and scalars upstream do not imply that these quantities are predicted accurately downstream where soot is present, accurate predictions upstream do increase the confidence in the corresponding downstream quantities which cannot be validated directly against experimental measurements.

Radial profiles of the axial velocity are shown in Fig. 38. Overall, agreement between the LES and the experimental measurements is excellent. At the furthest station downstream, the LES predicts a slightly smaller velocity than the experimental measurements, but this small deviation is certainly within the experimental uncertainty [1]. In a previous RANS study [93], the axial velocity at the furthest downstream station was significantly underpredicted for nearly all of the turbulence and combustion models investigated. Compared to this previous study, the present LES predicts the axial velocity much more accurately.

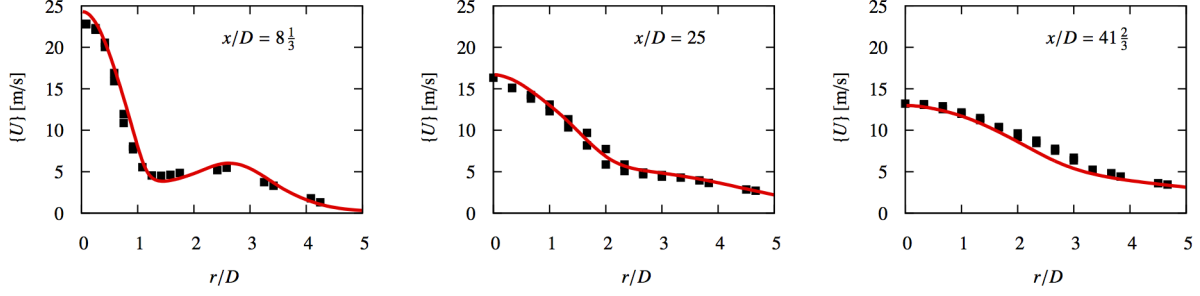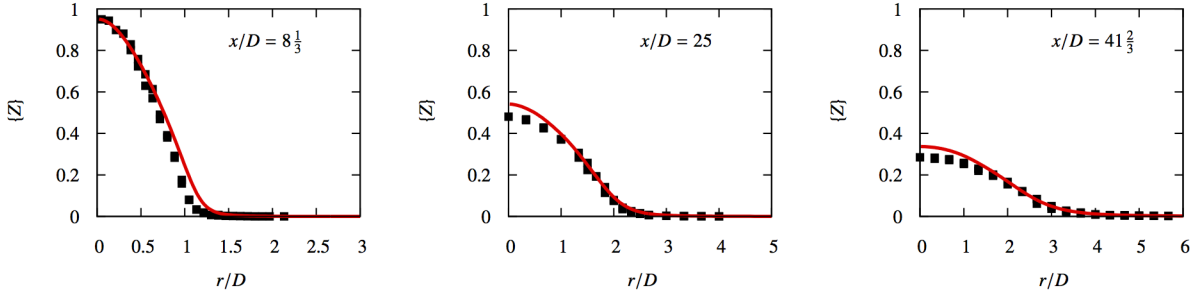Radial profiles of the mixture fraction are shown in Fig. 39. Overall, like the velocity, the

Figure 40: Radial profiles of the Favre-averaged temperature. The axial locations are indicated. Lines are the LES, and symbols are the experimental measurements of Nooren *et al.* [2].

LES agrees very well with the experimental measurements. The total potential experimental uncertainty for the mixture fraction is just less than 10% (though possibly up to nearly 25% in rich mixtures) [2], and most of the deviations from the experimental measurements are within this uncertainty. However, there are two minor discrepancies worth noting. First, the spreading rate of the jet at the first station near the nozzle is slightly too fast. Second, at the two downstream stations, the centerline mixture fraction is slightly overpredicted. These minor differences become more apparent in the temperature and species mass fractions profiles that follow.

In previous RANS studies [93–96], the same two discrepancies are observed, that is, an initial jet spreading rate that is too fast and an overprediction of the centerline mixture fraction at downstream locations. However, in the previous RANS studies, an overprediction of the jet spreading rate remains even at the stations furthest downstream from the nozzle. In the LES, the spreading rate of the jet seems to be only slightly overpredicted very close to the burner.

The minor discrepancy in the jet spreading rate near the burner is a consequence of the model for the subfilter mixture fraction variance. As discussed previously, an algebraic model cannot be used in the downstream region of the flame where soot is present. However, upstream, the dynamic algebraic model of Pierce and Moin [54] can be used. Using this model (results not shown), the mixture fraction variance was significantly smaller, consistent with the work of Kaul and coworkers [55, 56], and the initial jet spreading rate was well captured. Presumably, the correct spreading rate could also be captured with the transport equation model with the use of a more accurate model for the subfilter scalar dissipation rate. However, it is worth noting that the initial spreading rate was not sensitive to the value of the coefficient in Eq. 31, so a change in the model form would be needed.

Radial profiles of the temperature are shown in Fig. 40. Overall, both the shapes and magnitudes of the experimental profiles are predicted relatively accurately. Close to the burner, the slightly broadened temperature profile is consistent with the the corresponding mixture fraction profile in Fig. 39. Furthest from the burner, the temperature is somewhat overpredicted near the centerline. However, the experimental temperatures obtained with the Raman-Rayleigh-LIF technique may underpredict the temperature by up to 70 K, es-

60

Species	Uncertainty (%)	
	Lean	Rich
CO	20	25
CO_2	12	8
H_2	17	37
H_2O	11	18

Table 1: Total potential experimental uncertainty for the species mass fraction measurements [2].

pecially closer to the centerline where CH_4 interferes with the temperature measurement. Subsequent temperature measurements using CARS [97] confirmed the underprediction of the temperature with the Raman-Rayleigh-LIF technique.

In the previous RANS studies utilizing an adiabatic steady flamelet model [93], the temperature was globally overpredicted. Habibi *et al.* [96] considered radiation effects with a steady flamelet model. However, while the inclusion of radiation improved the prediction of the temperature at the measurement station furthest from the burner, the temperature closer to the burner was overpredicted. The overprediction is a consequence of using only burning flamelets with the steady flamelet model which does not capture the minor local extinction in the flame. With transported PDF methods [93–95], local extinction can be captured with RANS models. However, the predicted temperature is very sensitive to the amount of local extinction predicted by the mixing model and the value of any specified coefficient. The present LES RFPV model is an improvement upon both classes of RANS combustion models, capturing the correct amount of local extinction and accurately predicting the temperature without a strong sensitivity to a constant that must be specified for a mixing model. Admittedly, a constant must be specified for the subfilter scalar dissipation rate model in Eq. 31, but the predicted temperatures at the measurement stations considered in Fig. 40 are not sensitive to this constant.

Radial profiles of the major products of combustion are shown in Fig. 41. Nearly all of the discrepancies observed for the species are consistent with discrepancies observed for other quantities. For example, CO and H_2 are overpredicted near the centerline where the mixture fraction is overpredicted. Considering the larger experimental uncertainties for the individual species mass fractions, which are summarized in Table 1, overall agreement with the experimental measurements can be considered good.

As discussed above, near the burner where soot is not present, the subfilter variance could also be modeled with an algebraic model. With an algebraic model, both CO and H_2 show marked decreases (not shown) compared to the transport equation model, bringing them into better agreement with the experimental measurements. In addition, just as form the mixture fraction, the species do not show a significant sensitivity to the coefficient in the subfilter scalar dissipation rate model, at least compared to the sensitivity of the species to the subfilter variance model. This observation further highlights the need for improved subfilter scalar dissipation rate models.

4.3.3.2 Downstream Results: Soot In this section, the downstream LES results are presented. First, the evolution of soot in the jet flame is discussed qualitatively. Particular attention will be paid to the relative roles of the various formation, growth, and destruction

(a) Carbon Monoxide: CO

(b) Carbon Dioxide: CO_2

(c) Molecular Hydrogen: H_2
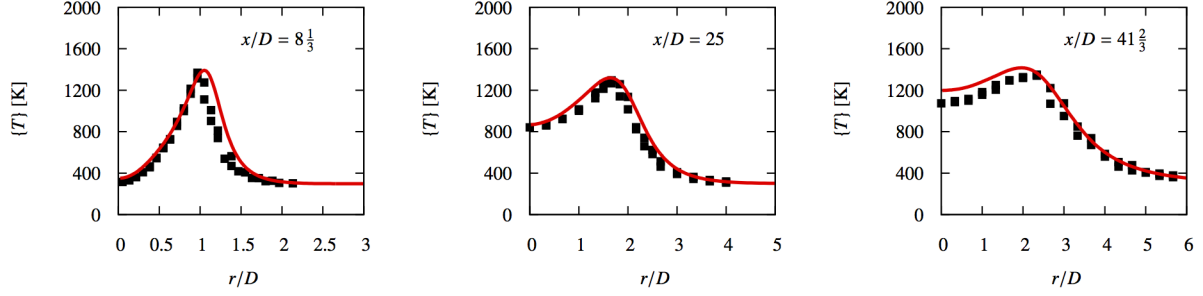

(d) Water Vapor: H_2O
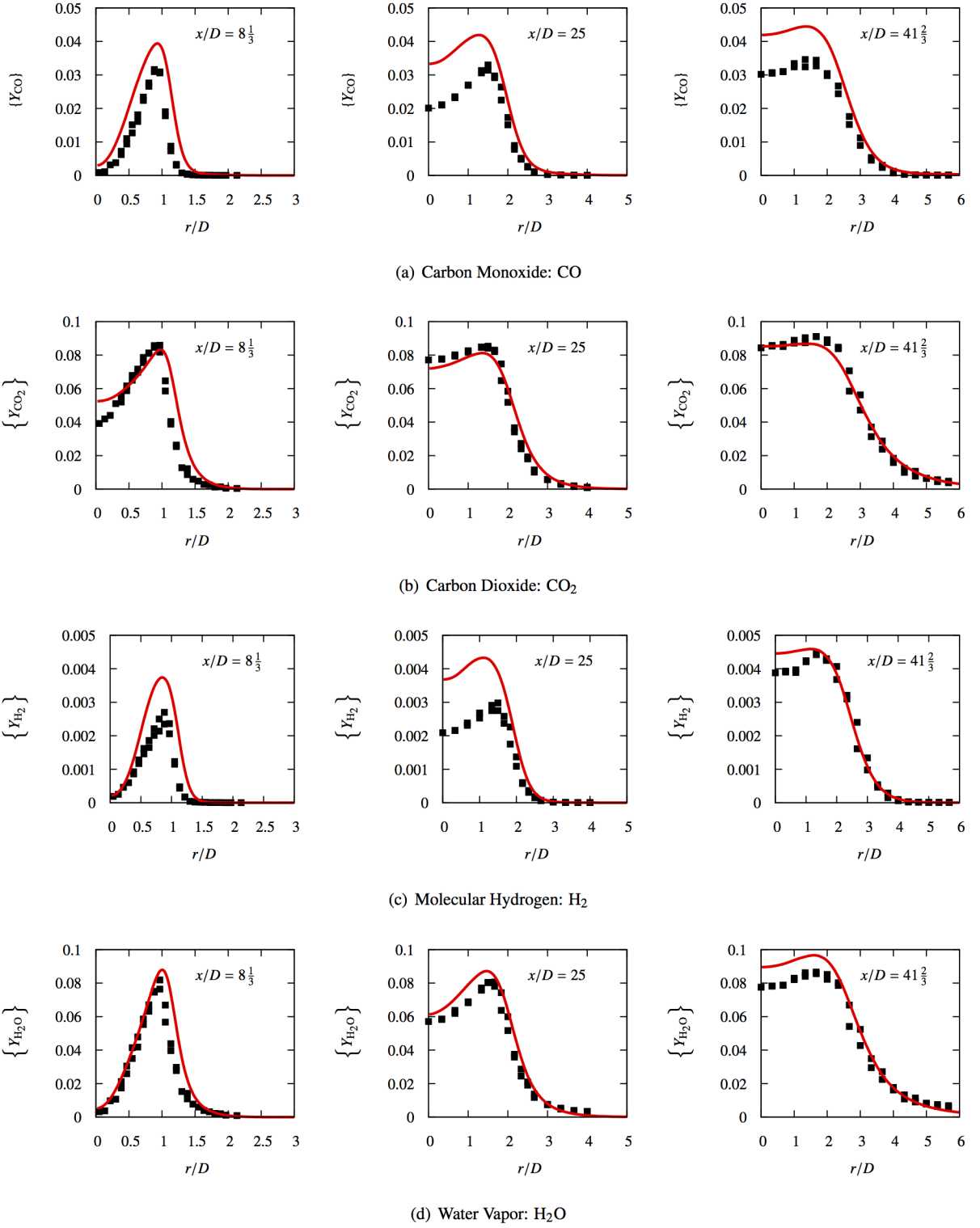
Figure 41: Radial profiles of the Favre-averaged mass fractions. The axial locations are indicated. Lines are the LES, and symbols are the experimental measurements of Nooren *et al.* [2].

(a) Volume Fraction, f_V [ppb]

(b) Number Density, $N \left[1/\text{cm}^3 \times 10^{-12}\right]$

(c) Primary Particle Diameter, d_p [nm]
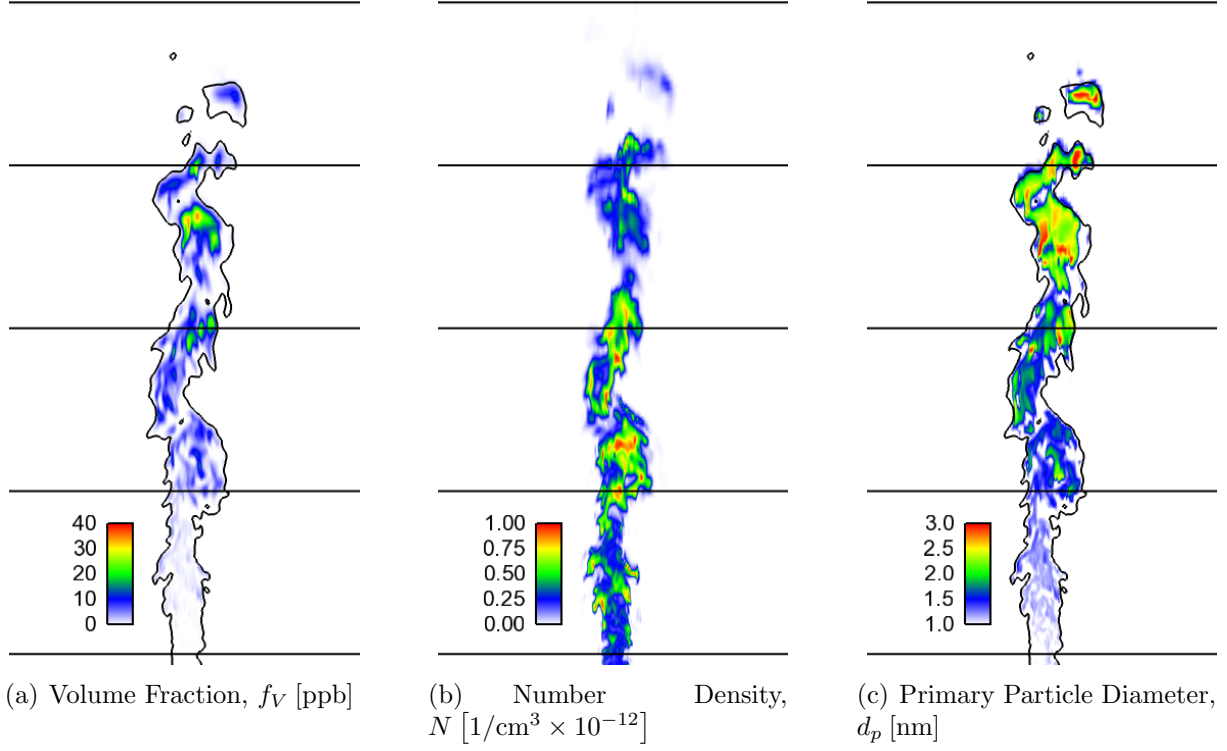
Figure 42: Instantaneous soot properties. The solid black lines correspond to the stoichiometric mixture fraction iso-contour. The horizontal lines demarcate intervals of $25\,x/D$ from 25 to 125.

processes. Then, the LES results are compared to the experimental soot volume fraction measurements [3]. Finally, soot is sensitive to the coefficient in subfilter scalar dissipation rate model (Eq. 31), and this sensitivity is investigated in detail.

The instantaneous fields of a few soot properties are shown in Fig. 42. Several qualitative features are immediately apparent. First, soot is confined only to regions of rich mixture fraction. When soot reaches stoichiometric mixtures, oxidation by OH proceeds so quickly that soot never has an appreciable residence time at lean mixtures. Second, soot is not homogeneous at a given mixture fraction or, in other words, is spatially intermittent, which is a consequence of the sensitivity of PAH to the local scalar dissipation rate. Spatial intermittency also arises from the fact that soot has no molecular diffusivity. However, most of this structure is lost in LES due to the implicit spatial filtering. Conversely, temporal intermittency is readily observed with more than a factor of three variation in the maximum soot volume fraction in the domain. Finally, the largest soot volume fractions tend to be present at mixture fractions significantly greater than stoichiometric. This fact is a consequence of the active soot growth mechanisms and will be discussed in greater detail in the subsequent paragraphs.

Each of the four regions indicated in Fig. 42 corresponds to a distinct phase of the soot evolution. In the first region ($x/D < 50$), the soot number density is large while the volume fraction and average primary particle diameter are relatively small. Here, nucleation of soot particles from PAH is the lone active process, resulting in many small particles. At slightly

63

(a) Volume Fraction, f_V [ppb]

(b) Number Density, $N \left[1/\mathrm{cm}^3 \times 10^{-12} \right]$

(c) Primary Particle Diameter, d_p [nm]
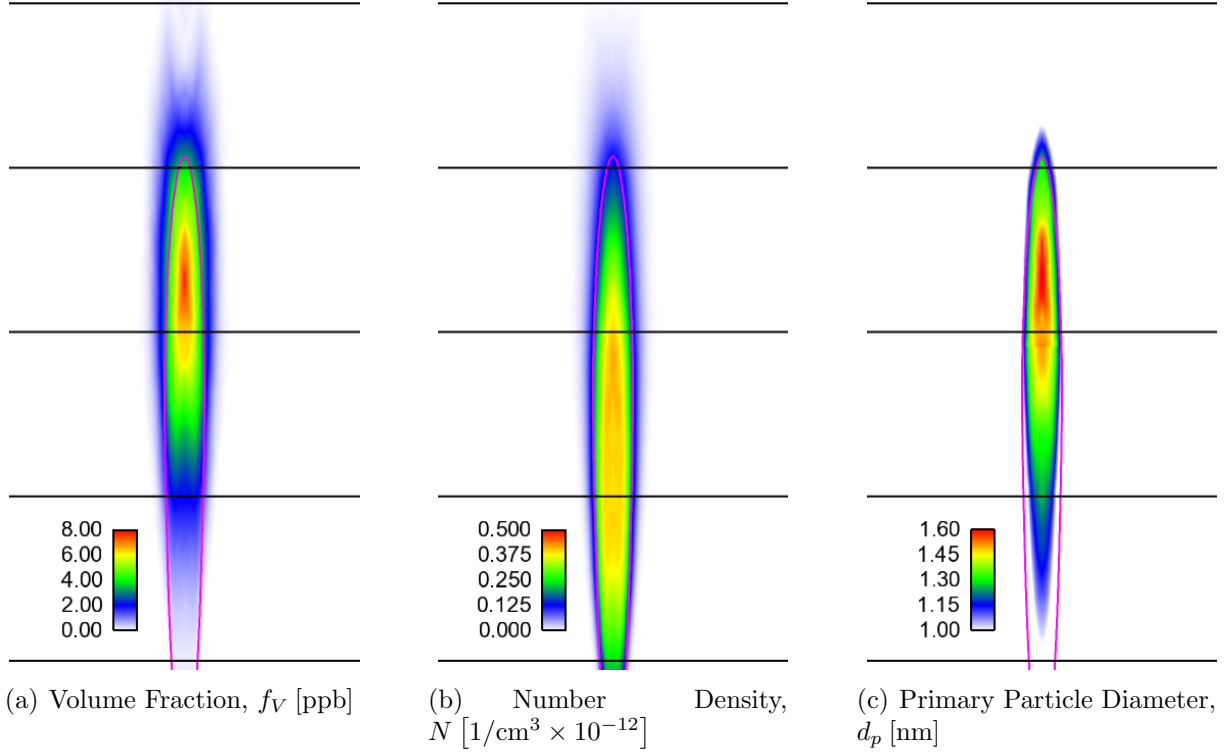
Figure 43: Time-averaged soot properties. All of the lines are the same as in Fig. 42.

larger heights above the burner ($50 < x/D < 75$), the number density remains roughly constant while the volume fraction and average primary particle diameter begin to increase. The particles formed in the lower region are now numerous enough that some of the PAH begins to condense onto existing particles rather than forming new particles. At higher heights yet ($75 < x/D < 100$), the volume fraction and primary particle diameter attain their maximum values, and the number density begins to decrease. At these locations, nearly all of the PAH condenses onto the now larger particles, and coagulation results in fewer but larger aggregates. Finally, far downstream ($x/D > 100$), regions of rich mixture fraction start to disappear as the flame closes, and the particles are oxidized by OH as they approach and finally pass through the stoichiometric mixture fraction iso-contour.

Just as observed in the DNS study of Bisetti *et al.* [24], surface growth is found to play a limited role in the evolution of soot. In this nonpremixed flame, soot nucleates around a mixture fraction of 0.2. Then, according to the DNS study, transport in mixture fraction space toward leaner or richer mixtures is roughly equally probable. If the soot is transported to richer mixture fraction, it lingers and grows according to the processes outlined above (condensation followed by coagulation). If the soot is transported to leaner mixture fractions, it first grows by surface growth but is then immediately oxidized as it passes through the stoichiometric mixture fraction iso-contour. However, since these particles are small, the cumulative growth by surface growth is relatively small, and, as a result, surface growth does not contribute significantly to the total soot formation rate in this flame.

The time-averaged fields of a few soot properties are shown in Fig. 43. The variation in the quantities moving downstream from the burner is very similar to the instantaneous images

| (a) Volume Fraction | (b) Total Intermittency |

Figure 44: Axial profiles of the averaged soot volume fraction and total intermittency. Lines are the LES, and symbols are the experimental measurements of Qamar *et al.* [3]. The solid red line is the nominal constant for the subfilter dissipation rate model (Eq. 31); the dashed green line is half t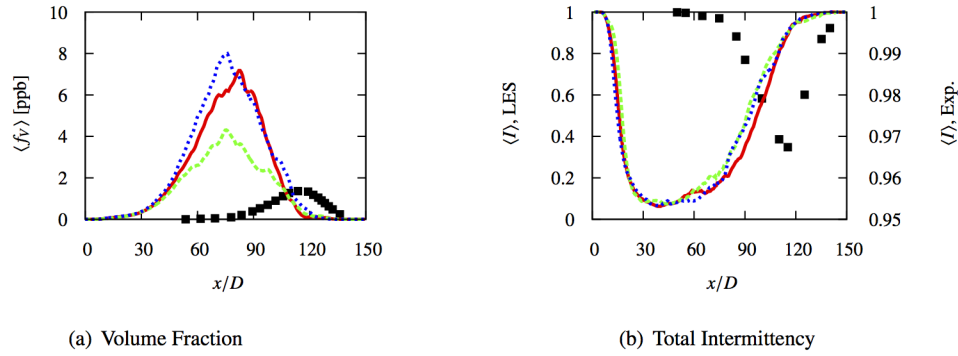he constant; and the dotted blue line is double the constant. Note that for the total intermittency the LES results and experimental measurements are plotted with different vertical scales.

in Fig. 42. However, note that the maximum time-averaged volume fraction and number density are significantly lower than the instantaneous maxima. This is a direct consequence of the intermittency of soot as a result of the sensitivity of PAH to the scalar dissipation rate and a lesser extent to the zero diffusivity of soot since the subfilter diffusivity dominates in LES. Also, in Fig. 43, significant soot volume fraction is present at lean mixtures due to the turbulent fluctuations in the radial direction (and axial direction at the flame tip) of the stoichiometric mixture fraction iso-contour. With a RANS model, this effect would not be observed, and soot would be confined entirely to regions of rich mixture fraction since it would be oxidized near the stoichiometric mixture fraction iso-contour.

The axial profile of the mean soot volume fraction is shown in Fig. 44 and compared with the experimental measurements of Qamar *et al.* [3]. The LES model is shown to reasonably predict the magnitude of the soot volume fraction, although this measure is sensitive to the subfilter scalar dissipation rate model as discussed in the subsequent section. However, soot is formed much earlier in the simulation than in the experiment. Subsequent analysis revealed the onset of soot was not sensitive the subfilter dissipation rate model. In this region only nucleation is active, which depends essentially only on the chemistry. Therefore, without additional validation data, this discrepancy must be attributed largely to the significant uncertainty in the kinetic mechanism for PAH formation and growth, particularly for methane flames.

The axial profile of the total intermittency is also shown in Fig. 44 and compared with the experimental measurements. The total intermittency is defined by Qamar *et al.* [3] as the probability of the soot volume fraction being less than 0.1 ppb (the experimental threshold) at a given location at a given time. In the LES, this measure is a function of not only the volume fraction but also the subfilter intermittency. While the LES predicts a much lower intermittency than the experiments, the comparison is difficult given the discrepancy

(a) $x/D = 66\frac{2}{3}$

(b) $x/D = 83\frac{1}{3}$
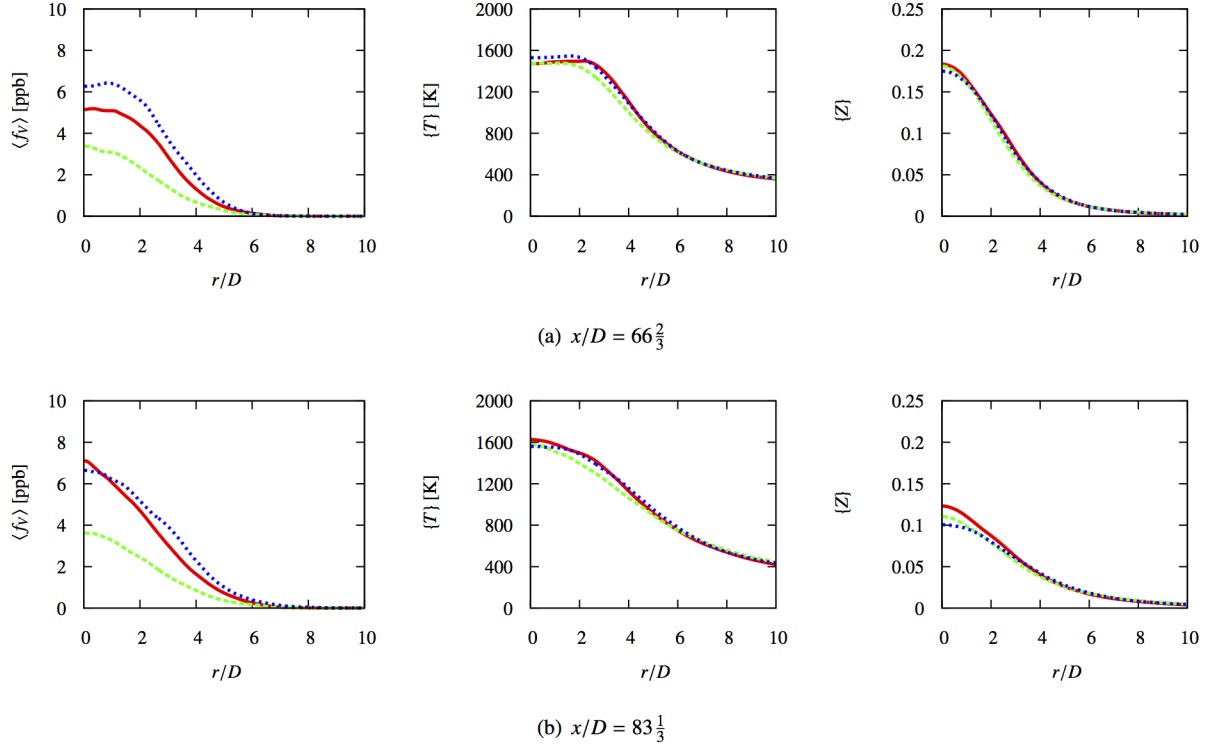
Figure 45: Radial profiles of soot volume fraction, temperature, and mixture fraction in the region of peak soot volume fraction. The different lines are the same as in Fig. 44.

in the volume fraction. However, like the experiments, the LES shows an increase in the intermittency in the oxidation region of the flame. As discussed by Qamar *et al.* [3], this indicates a reduction in frequency of soot events and not the intensity of these events in this region of the flame. Based on the LES results, this is a direct consequence of rich pockets of mixture fraction intermittently pinching off from the continuous region of rich mixture fraction upstream. This phenomenon can be observed in Fig. 42.

As alluded to previously, the LES results are quites sensitive to the subfilter dissipation rate model. Fig. 44 includes results for not only the nominal value of the constant in Eq. 31 but also the results with the coefficient doubled and halved. As shown in Fig. 44, the maximum time-averaged volume fraction decreases by nearly a factor of two when the constant in Fig. 31 is halved. On the other hand, the maximum volume fraction only increases by about 25% when the constant is doubled. The value of the constant does not appreciably affect the location of the onset of soot, the flame length, or the intermittency.

In order to determine the reason for the sensitivity the subfilter dissipation rate, radial profiles of the volume fraction, temperature, and mixture fraction are shown in Fig. 45 at two axial locations where the soot volume fraction is large. At both locations, there is only a minor difference between the temperature and mixture fraction profiles, some of which is due to a lack of complete statistical convergence, but the soot volume fraction profiles are markedly different. This indicates that the subfilter dissipation rate model does not affect soot through the background flow field and thermochemical state but instead through the

66

Figure 46: Conditional soot source terms. Lines are the same as in Fig. 44. Positive values correspond to the combined PAH formation and growth pathways (nucleation and condensation), and negative values correspond to oxidation.
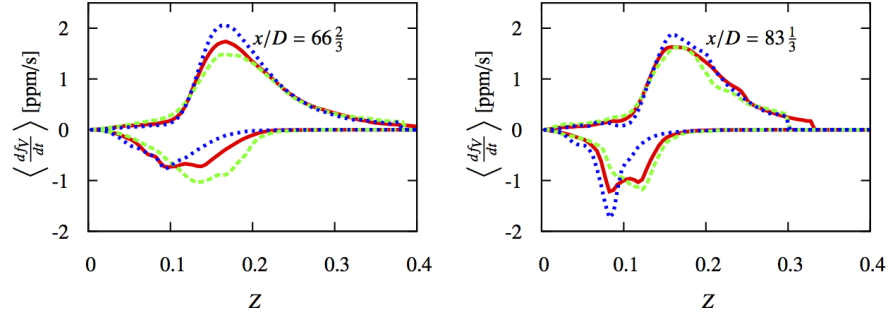
mixture fraction variance itself.

When the subfilter dissipation is decreased and the subfilter variance increased, the subfilter distribution of mixture fraction includes both leaner values and richer values. Increased amounts of lean mixture fractions increase the rate of oxidation, and as a result, as the variance increases, the rate of oxidation increases. Conversely, increased amounts of rich mixture fractions increase the combined rates of nucleation and condensation. However, the effect for rich mixture fractions is diminished as the PAH concentration is constrained to a relatively narrow profile centered around approximately $Z = 0.2$. This effect is readily seen in plots of the conditional source terms in Fig. 46. For larger variances, oxidation occurs at larger mixture fractions. On the other hand, nucleation and condensation are virtually unaffected. In the end, for the smaller subfilter dissipation, formation and growth are more co-located with oxidation in mixture fraction space, and the total soot yield is reduced.

An additional interesting trend in Fig. 44 is that the beginning of the increase in the soot volume fraction is largely independent of the model constant for the subfilter dissipation rate. In this region, the centerline line mixture fraction is still sufficiently large that, even for large subfilter variances, virtually no lean mixtures are present in the subfilter distribution of the mixture fraction. As a result, the argument above for increased oxidation with increased subfilter variance does not apply. Therefore, the premature increase in the volume fraction compared to the experiments is likely due to the significant uncertainty in the kinetic mechanism for PAH formation and growth. *A priori* analysis of the flamelet solutions revealed significant sensitivity to certain reaction pathways (such as that discussed in the previous section), which could easily account for the observed discrepancies.

4.3.4 Transported PDF Method Results

4.3.4.1 Instantaneous fields Figure 47 shows the instantaneous fields of temperature, PAH mass fraction, soot volume fraction, and soot number density. As expected, soot formation is predominant in the fuel-rich region inside the stoichimetric surface where moderately high temperatures aid the formation of PAH molecules. While PAH formation is initiated far upstream ($x/d > 20$), significant soot volume fraction is observed only after x/d=60.
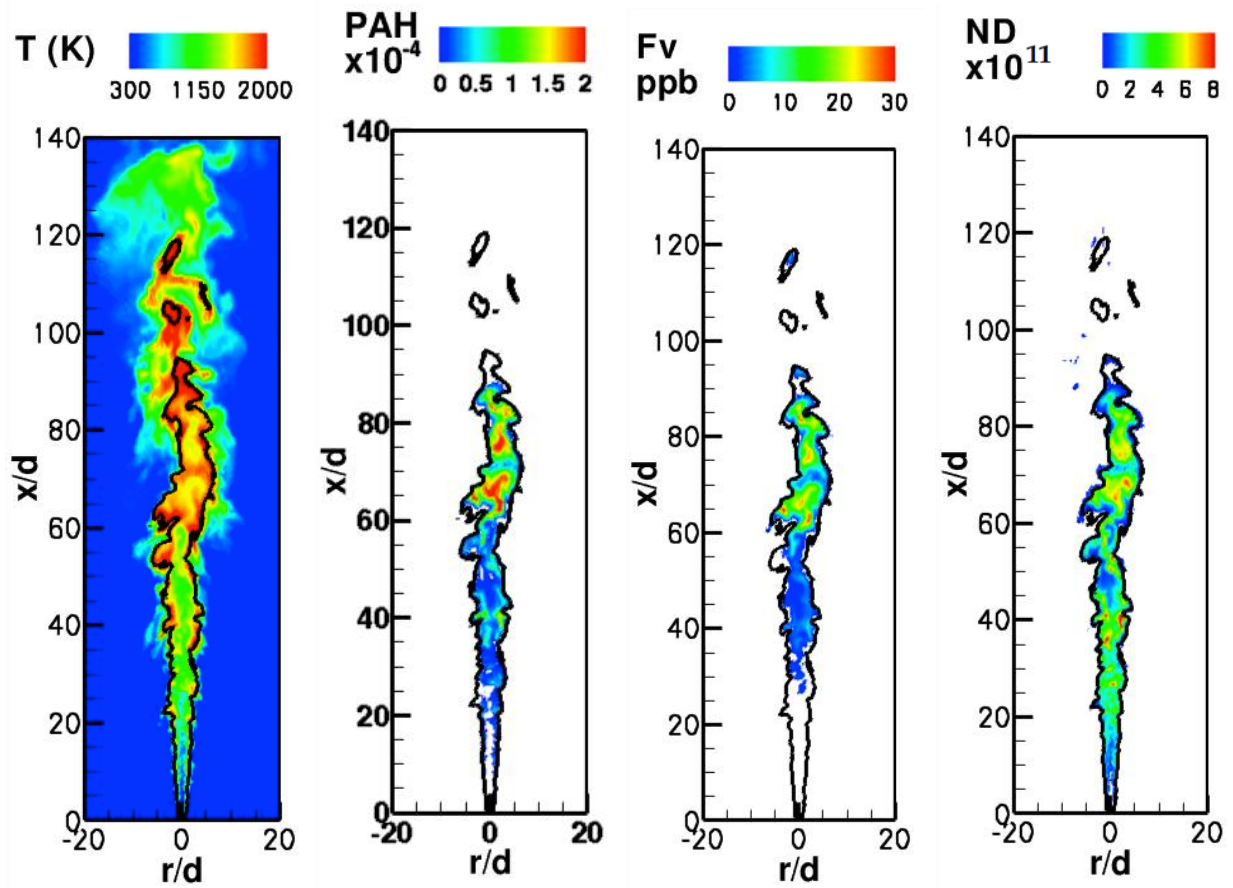
Figure 47: Instantaneous contours of temperature, PAH mass fraction, soot volume fraction, and soot number density. Iso-value of stoichiometric mixture fraction is indicated by a solid black line.

The lag between PAH growth and soot formation shows the time scale differences between the two processes. Similar to the experiment, soot formation is found to be highly intermittent with sporadic bursts of high soot volume fraction regions followed by extended periods of low soot volume fraction. Prior studies have demonstrated that soot precursor growth, especially the evolution of naphthalene, is highly sensitive to the strain rates in the flow. Consequently, the turbulent features that a fluid packet experiences strongly dictates soot nucleation [24]. Figure 47 also shows that the soot number density starts to increase far upstream due to nucleations up to $x/d=20$. Further downstream, the number density does not decrease substantially, indicating that soot coagulation is almost balanced by persisting nucleation process.

4.3.4.2 Soot and gas-phase statistics Figure 48 shows the time-averaged mixture fraction and temperature statistics for the flame, measured far upstream of the region of high soot volume fraction. Results indicate that the LES/PDF predicts the flame statistics reasonably accurately, including the RMS statistics of the flow. In the PDF technique,
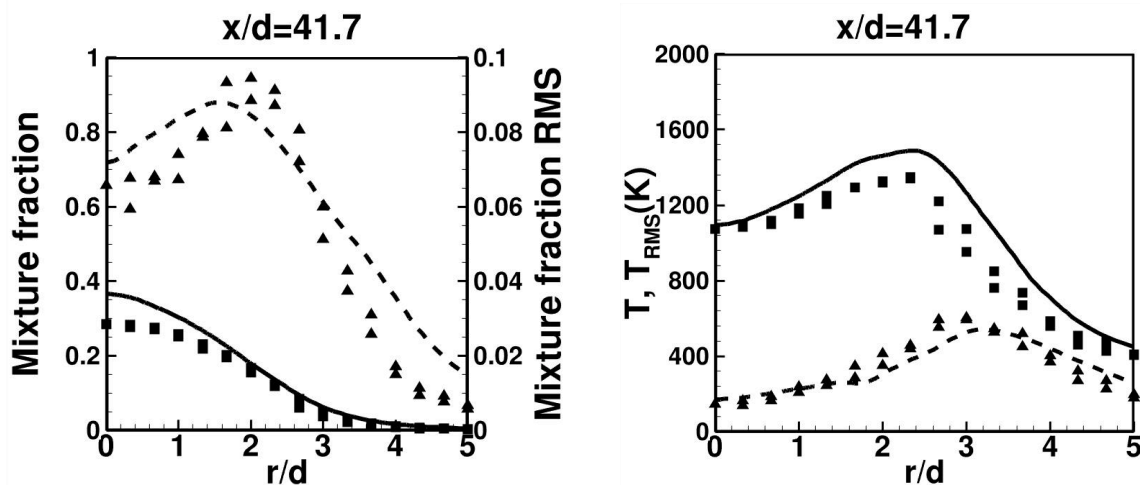
Figure 48: Comparison of time averaged mean and RMS of mixture fraction and temperature with the experiment of Nooren, *et. al.* [2]. Simulation: mean (——), RMS (••••); Experiment: mean (■), RMS (▲).
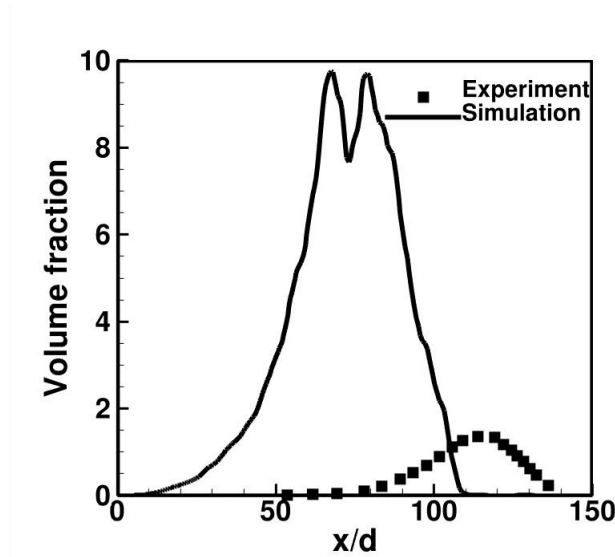
Figure 49: Comparison of soot volume fraction from the simulation with the experiment of Qamar, *et. al.* [3]. The data is plotted along the centerline.

the subfilter mixing model (Eq. 45) is a source of spatial numerical diffusion, since it mixes particles that are spatially distributed within a single control volume. As the dissipation rate increases, the higher mixing rates lead to increased numerical diffusion that will manifest as reduced temporal fluctuations. The accuracy of the RMS statistics provides confidence that the PDF numerics have not unduly affected the flame computation.

Figure 49 shows the soot volume fraction obtained from the LES/PDF approach and the experiments. The simulation results over predict the soot volume fraction substantially,

and also show an earlier inception and growth compared to the experiments. Mueller and Pitsch [98] reported that the soot profiles showed very large variations with the dissipation rate models used. Here, a dynamic procedure is used to evaluate the dissipation rate [66]. While this approach was shown to correctly predict extinction levels in partially-premixed flames, LES models that depend on scalar gradients are susceptible to high numerical errors [99, 100], which would partially explain the over prediction here.

Although the scalar comparisons upstream (Fig. 48) are reasonably good, it is not known if the minor errors seen upstream will propagate and amplify further downstream. For instance, the mixture fraction plots show an over-prediction of roughly 15% near the centerline, while the temperature itself is nearly the same as experiments. This mismatch could lead to fuel-rich high temperature regions downstream that will promote the formation of soot particles. Without further information on the scalar profiles downstream, it is not possible to deduce the role of these errors in prediction errors.

While comparing experiments to simulations, it is also important to consider the experimental errors. Methane flames are not highly sooting flames, with the peak soot volume fraction in the parts per billion levels. Further, the structure and characteristics of the soot particles are not known from the experiments. Given the experimental uncertainty associated with LII-based measurement of nascent low volume fraction soot signals, it is likely that these errors contribute to the mismatch as well.

4.3.4.3   Subfilter soot and scalar statistics   From the particle information, subfilter statistics and PDFs can be computed to better understand soot evolution. Figure 50 shows the instantaneous contours of subfilter standard deviation of mixture fraction, temperature, soot volume fraction, and number density. It is seen that the subfilter fluctuations of mixture fraction are confined to the near-stoichiometric region, with the variations essentially reduced to zero outside of this region. While temperature fluctuations follow a similar pattern, the high standard deviation regions are seen on the lean-side of the flame, outside the closed surface formed by the stoichiometric contour. It should be noted that small fluctuations in mixture fraction could lead to large changes in temperature close to the stoichiometric region. The subfilter fluctuations of soot moments are also large, reaching as high as 40% of the mean values. Similar to the filtered moments, the peaks in these quantities are located in the relatively high-temperature fuel-rich regions inside the stoichiometric surface.

Figure 51 shows the subfilter PDF of scalars computed at different axial locations, slightly off the centerline. The progress variable is skewed towards the values greater than 0.8, indicating a fully burning mixture. The mixture fraction PDF shows a broader spread, with significant probability of having fuel-rich pockets ($Z > 0.075$). The PAH PDF shows a bi-modal behavior with a large fraction of the particles having near-zero PAH concentrations and another group of particles with higher PAH values. These two groups of particles come from the fuel-lean and fuel-rich sides, respectively, corresponding to the broad mixture PDF observed. The PDF of soot moments exhibits a broad and nearly uniform PDF, with a bias towards zero moment corresponding to the fuel-lean mixture fraction values.

4.3.4.4   Conditional statistics   The evolution of the soot particles in mixture fraction and reaction progress variable coordinates is illustrative of the evolution process. Figure 52 shows the one-dimensional conditional scatter plots of PAH mass fraction, soot volume
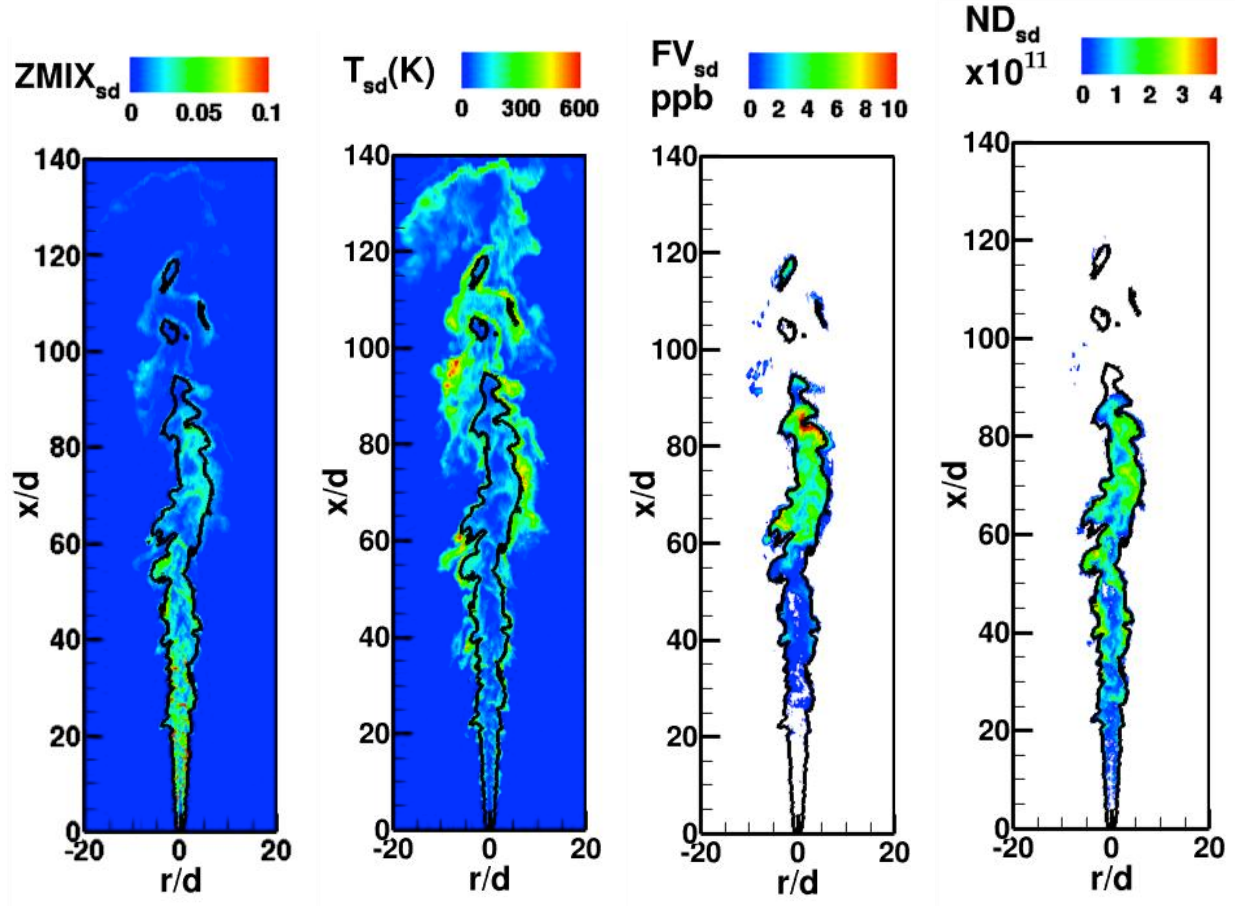
Figure 50: Instantaneous contours of subfilter standard deviation of mixture fraction, temperature, soot volume fraction and soot number density. Iso-value of stoichiometric mixture fraction is indicated by a solid black line.

71
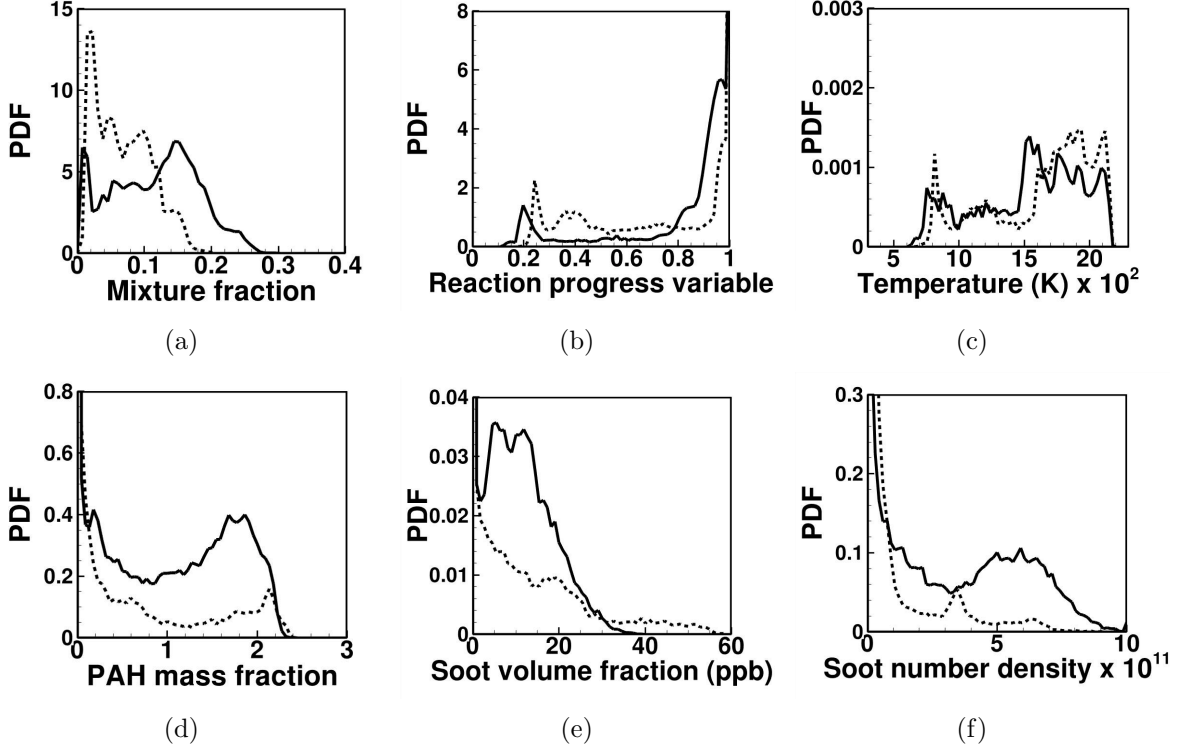
Figure 51: Time averaged marginal PDFs of (a) mixture fraction, (b) reaction progress variable, (c) temperature, (d) PAH mass fraction, (e) soot mass fraction, and (f) soot number density plotted at r/d=1.5. x/d=70: (——), x/d=90: (••••)

fraction and soot number density at x/d=70. Here, data sets at several instances, spanning more than 70 ms, have been pooled together. All three quantities show a peak in values near a mixture fraction of 0.165, which seems to be most likely fuel composition to contain soot. It is also seen that that there is a near linear increase in the quantities in the region of $0.075 < Z < 0.16$, but profiles have a non-linear shape in richer mixtures. To further understand these conditional statistics, Fig. 53 shows the instantaneous conditional scatter plot at two different locations at one time (same as that in Figs. 47 and 50). It is seen that the when the filtered soot volume fraction is lower (< 20 ppb), the conditional plots show a wider spread with richer regions containing significant soot volume fractions. Here, the mixture fraction PDF itself is broader, with a wider range of values present. However, when the filtered soot volume fraction is higher (x/d=90), the mixture fraction distribution appears narrower, and the conditional scatter plot exhibits a linear profile. These two modes result in the behavior see in Fig. 52.

Figure 54 shows the two-dimensional scatter plots of PAH mass fraction and soot volume fraction in $\{Z, C\}$ space. The plots show that PAH is significantly higher in a small region with very high progress variable in the fuel-rich region. This indicates that the formation of the soot precursors is confined to high temperature regions on the fuel-rich side of the stoichiometric surface (see Fig. 47). Soot volume fraction, on the other hand, has a wider spread with large soot volume fractions seen in regions of lower progress variable (and lower
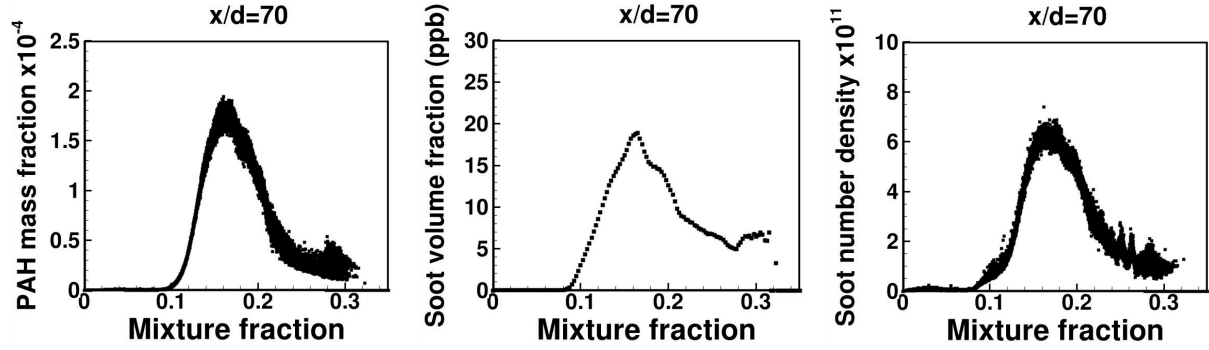
Figure 52: Conditional scatter plots of PAH mass fraction, soot volume fraction and soot number density plotted at x/d=70. Data obtained from multiple instantaneous fields.

temperature) inside the fuel-rich region. This indicates that the soot particles travel away from the region of high PAH concentration.

It is also important to note that these conditional scatter plots are sensitive to the subfilter mixing model used. Since soot particles do not diffuse, the assumption of equal diffusivity will have an impact on the results obtained here. In particular, soot oxidation in the near-stoichiometric region should be higher than that see in this simulation. Since the IEM model allows the notional particles to mix without reacting, allowing traversal in composition space across flame fronts, the effect of oxidation is under-predicted. The influence of differential diffusion on soot evolution needs further consideration
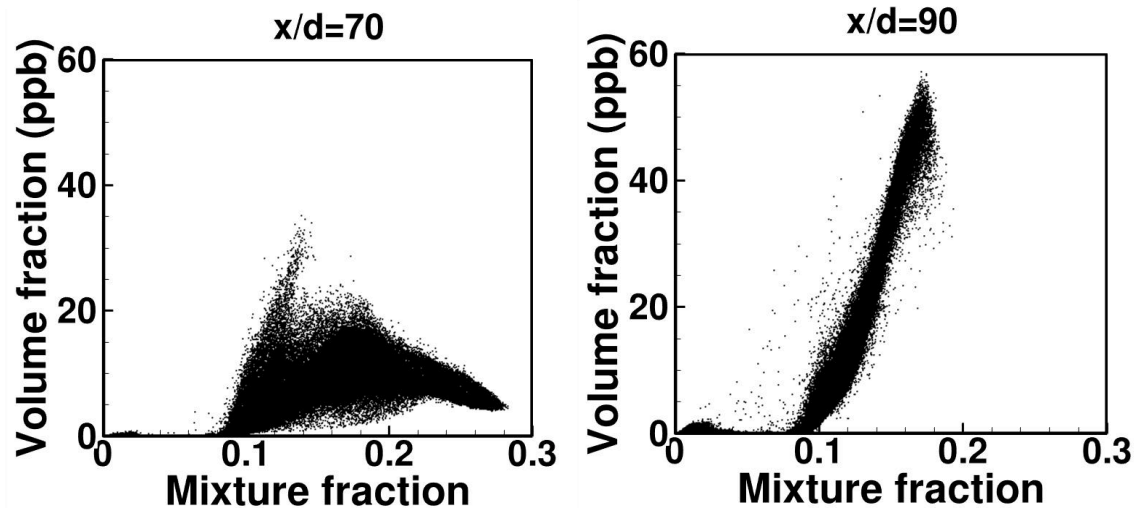
Figure 53: Instantaneous variation of soot volume fraction with mixture fraction plotted at x/d=70 (left) and x/d=90 (right).
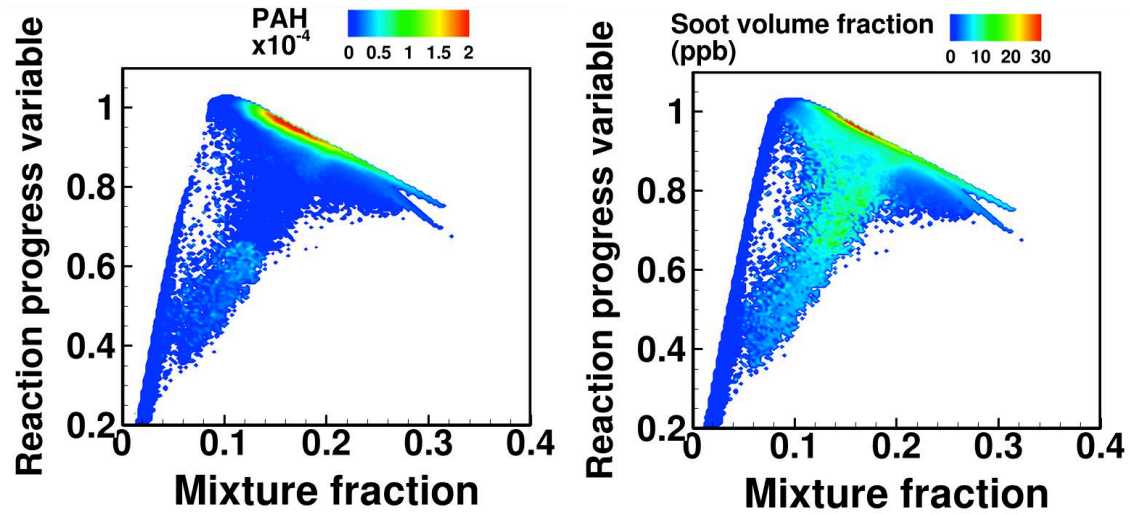
Figure 54: Time averaged contours of PAH mass fraction and soot volume fraction conditioned on mixture fraction and reaction progress variable plotted at x/d=70.

5   Conclusions

5.1   Conclusions on Soot Oxidation

We studied the thermodynamics and kinetics of aromatic oxyradicals, the key intermediates in oxidation of soot.

The results of the thermodynamics study show that thermodynamic stability varies substantially at different chemisorbed O sites.

Similarly, the results of the kinetics study show that the rate of oxyradical decomposition varies with the location of the chemisorbed O site.

The principal conclusion, combining the thermodynamic and kinetic results, is that only the "outer" rings are able to undergo oxidation, similar to phenoxy decomposition, whereas the inner rings resist oxidation in combustion environments. This finding implies that for an arbitrary shaped PAH, oxidation should predominantly remove armchair and corner-zigzag sites, leaving resistant-to-oxidation inner zigzag sites essentially intact. Considering that the growth of both armchair and zigzag edges proceed at effectively the same rate, we expect to find proliferation of zigzag-edge surfaces on soot particles formed in flame environments.

We also found that the variability of both thermodynamic stability and decomposition rate of aromatic oxyradicals can be explained and correlated with substrate aromaticity. These correlations could lead to development of practical rules for predicting oxidation rate coefficients for arbitrary size and shape aromatics, thereby supplementing and enhancing models of soot oxidation.

5.2   Conclusions of DNS Soot Study

In this project, we carried out the first DNS study of a turbulent sooting flame including finite rate chemistry of Polycyclic Aromatic Hydrocarbons (PAH), which are widely accepted as being precursors to soot particles.

Our results on the formation and early evolution of soot highlight several features having important implications in turbulent sooting flames research and modeling.

- The concentration of PAH is a function of local mixture fraction and scalar dissipation rate. Furthermore, unsteady mixing appears to significantly affect PAH concentration. This behavior explains the observed sensitivity of soot yield to strain rates. These findings emphasize that turbulent combustion models need to account adequately for the dependence of PAH concentrations on turbulent mixing. In addition, acetylene was shown to be less sensitive to strain. Semi-empirical models using acetylene to describe soot growth are not expected to capture the correct dependency of soot yield on mixing.

- Differential diffusion of soot due to negligible molecular diffusion transport contributes to spreading soot in mixture fraction space. While transport processes are approximately symmetric and movement towards and away from the flame is equally likely at early times, the distribution of soot in mixture fraction space is significantly biased. The highly non-linear growth and destruction processes affecting soot evolution

result in soot being preferentially located at mixtures richer than those where particles nucleate.

- Surface reactions are most active next to the flame sheet where soot is oxidized by hydroxyl radicals and molecular oxygen. Soot displaced towards the flame grows by surface reactions and is oxidized quickly. In regions of intense growth, the displacement speed is usually large, leaving little time for growth.

- The morphology of soot particles and aggregates is largely determined by their motion in mixture fraction space.

5.3   Conclusions on LES Soot Model

In this project, an integrated Large Eddy Simulation (LES) model for soot evolution in turbulent nonpremixed flames has been developed and validated in a laboratory scale natural gas jet diffusion flame. The model components include an accurate yet efficient soot model based on the Hybrid Method of Moments (HMOM), an extended Flamelet/Progress Variable (RFPV) gas-phase combustion model, which includes heat losses due to gas-phase radiation and which captures the detailed chemical kinetics of both fuel oxidation and soot precursor formation, and a model to account for the slow chemistry of PAH, the immediate precursors of soot. Presumed and transported PDF approaches for subfilter closure of the combustion and soot models were considered.

The model was validated in Delft Flame III, a piloted coflow turbulent nonpremixed flame fueled by commercial natural gas. Results for velocity, mixture fraction, temperature, and major species mass fractions in the upstream, non-sooting region of the flame showed very good agreement with experimental measurements, especially compared to previous RANS studies.

Compared to the experimental measurements, the LES provided a reasonable prediction of the maximum soot volume fraction. This quantity was found to be sensitive to the description of small scale mixing rates. In the presumed PDF approach, the relevant parameter is the subfilter scalar dissipation rate. Improved agreement was obtained by decreasing the model constant for this quantity, which increases the subfilter scalar variance. Similarly, simulations using the transported PDF were found to be sensitive to the mixing constant used in the micromixing model.

However, the LES predicted the formation of soot much closer to the nozzle than in the experiment. The primary reason for this discrepancy was attributed to significant uncertainty in the chemistry of PAH. The LES was also compared to experimental measurements of the total intermittency, the probability of soot being less than a specified threshold at a given location at a given time. While quantitative comparisons are not meaningful in light of the disagreement in the volume fraction profile, the LES and experimental measurements both showed a gradual increase in the intermittency as soot is oxidized. This increase is indicative of a decrease in the frequency of pockets of large soot volume fraction in the soot oxidation zone rather than a simple decrease in the soot volume fraction.

While this work is major step forward in the modeling of soot evolution with LES, two major modeling needs that have a significant impact on the results presented here have been identified. First, the results were shown to be quite sensitive to the model coefficients used to

parameterize small scale mixing rates. More reliable models for variance and dissipation rate in presumed PDF approaches and for micromixing in transported PDF approaches would lead to improvements in predictions of soot evolution in turbulent combustion. Second, considerable uncertainty remains in the kinetic mechanism for PAH formation and growth. Both these issues will be addressed in future research efforts.

Bibliography

[1] P. Stroomer. *Turbulence and OH structures in flames*. PhD thesis, Delft University of Technology, 1995.

[2] P. A. Nooren, M. Versluis, T. H. van der Meer, R. S. Barlow, and J. H. Frank. Raman-Rayleigh-LIF measurements of temperature and species concentrations in the Delft piloted turbulent jet diffusion flame. *Appl. Phys. B*, 71:95–111, 2000.

[3] N. H. Qamar, Z. T. Alwahabi, Q. N. Chan, G. J. Nathan, D. Roekaerts, and K. D. King. Soot volume fraction in a piloted turbulent jet non-premixed flame of natural gas. *Combust. Flame*, 156:1339–1347, 2009.

[4] M. Frenklach. Reaction mechanism of soot formation in flames. *Phys. Chem. Chem. Phys.*, 4:2028–2037, 2002.

[5] H. Bockhorn, A. D'Anna, A. F. Sarofim, and H. Wang. *Combustion Generated Fine Carbonaceous Particles*. KIT Scientific, Karlsruhe, Germany, 2009.

[6] H. Wang. Formation of nascent soot and other condensed-phase materials in flames. *Proc. Combust. Inst.*, 33:41–67, 2011.

[7] M. Frenklach. *A Unifying Picture of Gas Phase Formation and Growth of PAH, Soot, Diamond and Graphite*, pages 259–273. NASA Conference Publication 3061, 1990.

[8] M. Frenklach and H. Wang. Detailed modeling of soot particle nucleation and growth. *Proc. Combust. Inst.*, 23:1559–1566, 1991.

[9] M. Frenklach. On surface growth mechanism of soot particles. *Proc. Combust. Inst.*, 26:2285–2293, 1996.

[10] R. Whitesides and M. Frenklach. Detailed kinetic monte carlo simulations of graphene-edge growth. *J. Phys. Chem. A*, 114:689–703, 2010.

[11] J. Appel, H. Bockhorn, and M. Frenklach. Kinetic modeling of soot formation with detailed chemistry and physics. laminar premixed flames of c2 hydrocarbons. *Combust. Flame*, 121:122–136, 2000.

[12] K. G. Neoh, J. B. Howard, and A. F. Sarofim. page 261. Plenum, New York, 1981.

[13] M. S. Celnik, M. Sander, A. Raj, R. H. West, and M. Kraft. Modelling soot formation in a premixed flame using an aromatic-site soot model and an improved oxidation rate. *Proc. Combust. Inst.*, 32:639–646, 2009.

[14] B. Zhao, Z. Yang, M.V. Johnston, H. Wang, A.S. Wexler, M. Balthasar, and M. Kraft. Measurement and numerical simulation of soot particle size distribution functions in a laminar premixed ethylene-oxygen-argon flame. *Combustion and Flame*, 133:173–188, 2003.

[15] B. Zhao, Z. Yang, Z. Li, M.V. Johnston, and H. Wang. Particle size distribution function of incipient soot in laminar premixed ethylene flames: effect of flame temperature. *Proceedings of the Combustion Institute*, 30:1441–1448, 2005.

[16] Ü.Ö. Köylü, GM FaethT L, and MG Carvalho. Fractal and projected structure properties of soot aggregates. *Combustion and Flame*, 100:621–633, 1995.

[17] D.L. Marchisio and R.O. Fox. Solution of population balance equations using the direct quadrature method of moments. *Journal of Aerosol Science*, 36:43–73, 2005.

[18] M. E. Mueller, G. Blanquart, and H. Pitsch. A joint Volume-Surface model of soot aggregation with the method of moments. *Proc. Combust. Inst.*, 32:785–792, 2009.

[19] G. Blanquart and H. Pitsch. A joint Volume-Surface-Hydrogen multi-variate model for soot formation. In H. Bockhorn, A. D'Anna, A. Sarofim, and H. Wang, editors, *Combustion Generated Fine Carbonaceous Particles*, pages 439–466. KIT Scientific Publishing, 2009.

[20] M. Frenklach and S. J. Harris. Aerosol dynamics modeling using the method of moments. *J. Coll. Int. Sci.*, 118:252–261, 1987.

[21] M. Frenklach. Method of moments with interpolative closure. *Chemical Engineering Science*, 57:2229–2239, 2002.

[22] R. McGraw. Description of aerosol dynamics by the quadrature method of moments. *Aerosol Science and Technology*, 27:255–265, 1997.

[23] M. E. Mueller, G. Blanquart, and H. Pitsch. Hybrid Method of Moments for modeling soot formation and growth. *Combust. Flame*, 156:1143–1155, 2009.

[24] F. Bisetti, G. Blanquart, M. E. Mueller, and H. Pitsch. On the formation and early evolution of soot in turbulent nonpremixed flames. *Combust. Flame*, In Press.

[25] M. E. Mueller, G. Blanquart, and H. Pitsch. Modeling the oxidation-induced fragmentation of soot aggregates in laminar flames. *Proc. Combust. Inst.*, 33:667–674, 2011.

[26] H. Pitsch. Large-eddy simulation of turbulent combustion. *Annual Review of Fluid Mechanics*, 38:453–482, 2006.

[27] H. El-Asrag and S. Menon. Large eddy simulation of soot formation in a turbulent non-premixed jet flame. *Combust. Flame*, 156:385–395, 2009.

[28] D. O. Lignell, J. H. Chen, P. J. Smith, T. Lu, and C. K. Law. The effect of flame structure on soot formation and transport in turbulent nonpremixed flames using direct numerical simulation. *Combust. Flame*, 151:2–28, 2007.

[29] D. O. Lignell, J. H. Chen, and P. J. Smith. Three-dimensional direct numerical simulation of soot formation and transport in a temporally evolving nonpremixed ethylene jet flame. *Combust. Flame*, 155:316–333, 2008.

[30] M. E. Mueller and H. Pitsch. LES subfilter modeling of soot-turbulence interactions. *Phys. Fluids*, Submitted.

[31] R.P. Lindstedt and S.A. Louloudi. Joint-scalar transported pdf modeling of soot formation and oxidation. *Proceedings of the Combustion Institute*, 30(1):775 – 783, 2005.

[32] Abhilash J. Chandy, David J. Glaze, and Steven H. Frankel. A Hybrid Large Eddy Simulation/Filtered Mass Density Function for the Calculation of Strongly Radiating Turbulent Flames. *Journal of Heat Transfer - Transactions of the ASME*, 131(5), May 2009.

[33] J. P. Perdew, K. Burke, and M. Ernzerhof. Generalized gradient approximation made simple. *Phys. Rev. Lett.*, 77:3865–3868, 1996.

[34] O. F. Sankey and D. J. Niklewski. Abinitio multicenter tight-binding model for molecular-dynamics simulations and other applications in covalent systems. *Phys. Rev. B*, 40:3979–3995, 1989.

[35] J. M. Soler, E. Artacho, J. D. Gale, A. Garcia, J. Junquera, P. Ordejon, and D. Sanchez-Portal. The siesta method for ab initio order-n materials simulation. *J. Phys.-Condensed Matter*, 14:2745–2779, 2002.

[36] J. J. P. Stewart. Optimization of parameters for semiempirical methods v: Modification of nddo approximations and application to 70 elements. *J. Mol. Modeling*, 13:1173–1213, 2007.

[37] J Kruszewski and T. M. Krygowski. Definition of aromaticity basing on harmonic oscillator model. *Tetrahedron Lett.*, 36:3839, 1972.

[38] A. D. Becke. Density-functional thermochemistry .3. the role of exact exchange. *J. Chem. Phys.*, 98:5648–5652, 1993.

[39] R. Krishnan, J. S. Binkley, R. Seeger, and J. A. Pople. Self-consistent molecular-orbital methods .20. basis set for correlated wave-functions. *J. Chem. Phys.*, 72:650–654, 1980.

[40] J. R. Barker. *Int. J. Chem. Kinet.*, 41:748–763, 2009.

[41] R. G. Gilbert and S. C. Smith. *Theory of Unimolecular and Recombination Reactions.* Blackwell-Scientific, Oxford, UK, 1990.

[42] H. Wang and M. Frenklach. *Combust. Flame*, 96:163–170, 1994.

[43] D. M. Golden. What do we know about the iconic system CH3+ CH3+ M C2H6+ M? *Z. Phys. Chem.*, 225:1–14, 2011.

[44] D. L. Marchisio and R. O. Fox. Solution of population balance equations using the Direct Quadrature Method of Moments. *J. Aerosol Sci.*, 36:43–73, 2005.

[45] C. D. Pierce and P. Moin. Progress variable approach for Large Eddy Simulation of non-premixed turbulent combustion. *J. Fluid Mech.*, 504:73–97, 2004.

[46] N. Peters. Laminar diffusion flamelet models in non-premixed turbulent combustion. *Prog. Energy Combust. Sci.*, 10:319–339, 1984.

[47] M. Ihme and H. Pitsch. Modeling of radiation and nitric oxide formation in turbulent nonpremixed flames using a flamelet/progress variable formulation. *Phys. Fluids*, 20:055110, 2008.

[48] H. Pitsch and N. Peters. A consistent flamelet formulation for non-premixed combustion considering differential diffusion effects. *Combust. Flame*, 114:26–40, 1998.

[49] R. W. Bilger. The structure of turbulent nonpremixed flames. *Proc. Combust. Inst.*, 22:475–488, 1988.

[50] R. S. Barlow, A. N. Karpetis, J. H. Frank, and J.-Y. Chen. Scalar profiles and NO formation in laminar opposed-flow partially premixed methane/air flames. *Combust. Flame*, 127:2102–2118, 2001.

[51] A. W. Cook and J. J. Riley. A subgrid model for equilibrium chemistry in turbulent flows. *Phys. Fluids*, 6:2868–2870, 1994.

[52] J. Jiménez, A. Liñán, M. M. Rogers, and J. F. Higuera. A priori testing of subgrid models for chemically reacting non-premixed turbulent shear flows. *J. Fluid Mech.*, 349:149–171, 1997.

[53] C. Wall, B. J. Boersma, and P. Moin. An evaluation of the assumed beta probability density function subgrid-scale model for large eddy simulation of nonpremixed, turbulent combustion with heat release. *Phys. Fluids*, 12:2522–2529, 2000.

[54] C. D. Pierce and P. Moin. A dynamic model for subgrid-scale variance and dissipation rate of a conserved scalar. *Phys. Fluids*, 10:3041–3044, 1998.

[55] C. M. Kaul, V. Raman, G. Balarac, and H. Pitsch. Numerical errors in the computation of subfilter scalar variance in large eddy simulations. *Phys. Fluids*, 21:055102, 2009.

[56] C. M. Kaul and V. Raman. *A posteriori* analysis of numerical errors in subfilter scalar variance modeling for large eddy simulation. *Phys. Fluids*, 23:035102, 2011.

[57] M. Ihme and H. Pitsch. Prediction of extinction and reignition in nonpremixed turbulent flames using a flamelet/progress variable model. 2. Application in LES of Sandia flames D and E. *Combust. Flame*, 155:90–107, 2008.

[58] S. James, J. Zhu, and M. S. Anand. Lagrangian PDF transport method for simulations of axisymmetric turbulent reacting flows. In *43rd AIAA Aerospace Sciences Meeting and Exhibit*, number 156, 2005.

[59] S. B. Pope. A Monte Carlo method for the PDF equations of turbulent reactive flow. *Combustion Science and Technology*, 25:159–174, 1981.

[60] P. J. Colucci, F. A. Jaberi, and P. Givi. Filtered density function for large eddy simulation of turbulent reacting flows. *Physics of Fluids*, 10(2):499–515, 1998.

[61] V. Raman, H. Pitsch, and R. O. Fox. A consistent hybrid LES-FDF scheme for the simulation of turbulent reactive flows. *Combustion and Flame*, 143(1-2):56–78, 2005.

[62] H. Pitsch, E. Riesmeier, and N. Peters. Unsteady flamelet modeling of soot formation in turbulent diffusion flames. *Combustion science and technology*, 158:389–406, 2000.

[63] Y. Liu and R. O. Fox. Cfd predictions for chemical processing in a confined impinging-jets reactor. *AIChE Journal*, 52:731, 2006.

[64] R. O. Fox. *Computational Models for Turbulent Reacting Flows*. Cambridge University Press, Cambridge, 2003.

[65] F. A. Jaberi, P. J. Colucci, S. James, P. Givi, and S. B. Pope. Filtered mass density function for large-eddy simulation of turbulent reacting flows. *Journal of Fluid Mechanics*, 401:85–121, 1999.

[66] V. Raman and H. Pitsch. A consistent LES/filtered-density function formulation for the simulation of turbulent flames with detailed chemistry. *Proceedings Proceedings of the Combustion Institute*, 31:1711–1719, 2006.

[67] H. Pitsch. FlameMaster. A C++ computer program for 0D combustion and 1D laminar flame calculations.

[68] G. Blanquart, P. Pepiot-Desjardins, and H. Pitsch. Chemical mechanism for high temperature combustion of engine relevant fuels with emphasis on soot precursors. *Combust. Flame*, 156:588–607, 2009.

[69] K. Narayanaswamy, G. Blanquart, and H. Pitsch. A consistent chemical mechanism for oxidation of substituted aromatic species. *Combust. Flame*, 157:1879–1898, 2010.

[70] C. S. McEnally and L. D. Pfefferle. An experimental study in non-premixed flames of hydrocarbon growth processes that involve five-membered carbon rings. *Combust. Sci. Tech.*, 131:323–344, 1998.

[71] A. Laskin and A. Lifshitz. Thermal decomposition of indene: Experimental results and kinetic modeling. *Proc. Combust. Inst.*, 27:313–320, 1998.

[72] M. Frenklach, C. A. Schuetz, and J. Ping. Migration mechanism of aromatic-edge growth. *Proc. Combust. Inst.*, 30:1389–1396, 2005.

[73] R. Whitesides, D. Domin, R. Salomón-Ferrer, Jr. Lester, W. A., and M. Frenklach. Embedded-ring migration on graphene zigzag edge. *Proc. Combust. Inst.*, 32(1):577–583, 2009.

[74] X.Q. You, R. Whitesides, D. Zubarev, Jr. Lester W. A., and M. Frenklach. Bay-capping reactions: Kinetics and influence on graphene-edge growth. *Proc. Combust. Inst.*, 33:685–692, 2011.

[75] D. Y. Zubarev, N. Robertson, D. Domin, J. McClean, J. Wang, Jr. Lester, W. A., R. Whitesides, X. You, and M. Frenklach. Local electronic structure and stability of pentacene oxyradicals. *J. Phys. Chem. C*, 114:5429–5437, 2010.

[76] D. Y. Zubarev, X. You, J. McClean, Jr. Lester, W. A., and M. Frenklach. Patterns of local aromaticity in graphene oxyradicals. *J. Mater. Chem.*, 21:3404–3409, 2011.

[77] D. Y. Zubarev, X. You, J. McClean, Jr. Lester, W. A., and M. Frenklach. Delocalization effects in pristine and oxidized graphene substrates. In P. E. Hoggan, E. J. Bröndas, J. Maruani, P. Piecuch, , and G. Delgado-Barrio, editors, *Advances in the Theory of Quantum Systems in Chemistry and Physics*, pages 553–569. Springer, Dordrecht, 2012.

[78] X. You, D. Yu. Zubarev, Jr. Lester, W. A., and M. Frenklach. Thermal decomposition of pentacene oxyradicals. *J. Phys. Chem. A*, 115:14184–14190, 2011.

[79] L. R. Radovic. Active sites in graphene and the mechanism of CO2 formation in carbon oxidation. *J. Am. Chem. Soc.*, 131:17166–17175, 2009.

[80] N. Kunioshi, M. Touda, and S. Fukutani. Computational study on the formation of five-membered rings in PAH through reaction with O2. *Combust. Flame*, 128(3):292–300, 2002.

[81] C. Y. Lin and M. C. Lin. Thermal decomposition of methyl phenyl ether in shock waves: the kinetics of phenoxy radical reactions. *J. Phys. Chem.*, 90(3):425–431, 1986.

[82] P. Frank, J. Herzler, Th Just, and C. Wahl. High-temperature reactions of phenyl oxidation. *Symp. Int. Combust.*, 25:833–840, 1994.

[83] Norbert Peters. *Turbulent Combustion*. Cambridge University Press, 2000.

[84] H. Pitsch, E. Riesmeier, and N. Peters. Unsteady flamelet modeling of soot formation in turbulent diffusion flames. *Combust. Sci. Tech.*, 158:389–406, 2000.

[85] T. W. J. Peeters, P. P. J. Stroomer, J. E. de Vries, D. J. E. M. Roekaerts, and C.J. Hoogendoorn. Comparative experimental and numerical investigation of a piloted turbulent natural-gas diffusion flame. *Proc. Combust. Inst.*, 25:1241–1248, 1994.

[86] O. Desjardins, G. Blanquart, G. Balarac, and H. Pitsch. High order conservative finite difference scheme for variable density low mach number turbulent flows. *J. Comp. Phys.*, 227:7125–7159, 2008.

[87] M. Hermann, G. Blanquart, and V. Raman. A bounded QUICK scheme for preserving scalar bounds in large-eddy simulations. *AIAA J.*, 44:2879–2886, 2006.

[88] M. Germano, U. Piomelli, P. Moin, and W. H. Cabot. A dynamic subgrid-scale eddy viscosity model. *Phys. Fluids A*, 3:1760–1765, 1991.

[89] P. Moin, K. Squires, W. Cabot, and S. Lee. A dynamic subgrid-scale model for compressible turbulence and scalar transport. *Phys. Fluids A*, 3:2746–2757, 1991.

[90] D. K. Lilly. A proposed modification of the Germano subgrid-scale closure method. *Phys. Fluids A*, 4:633–635, 1992.

[91] C. Meneveau, T. S. Lund, and W. H. Cabot. A Lagrangian dynamic subgrid-scale model of turbulence. *J. Fluid Mech.*, 319:353–385, 1996.

[92] J. Réveillon and L. Vervisch. Response of the dynamic LES model to heat release induced effects. *Phys. Fluids*, 8:2248–2250, 1996.

[93] B. Merci, B. Naud, and D. Roekaerts. Flow and mixing fields for transported scalar PDF simulations of a piloted jet diffusion flame ('Delft Flame III'). *Flow Turb. Combust.*, 74:239–272, 2005.

[94] B. Merci, D. Roekaerts, and B. Naud. Study of the the performance of three micromixing models in transported scalar PDF simulations of a piloted jet diffusion flame ("Delft Flame III"). *Combust. Flame*, 144:476–493, 2006.

[95] B. Merci, B. Naud, and D. Roekaerts. Interaction between chemistry and micro-mixing modeling in transported PDF simulations of turbulent non-premixed flames. *Combust. Sci. Tech.*, 179:153–172, 2007.

[96] A. Habibi, B. Merci, and D. Roekaerts. Turbulence radiation interaction in Reynolds-averaged Navier-Stokes simulations of nonpremixed piloted turbulent laboratory-scale flames. *Combust. Flame*, 151:303–320, 2007.

[97] E. H. van Veen and D. Roekaerts. On the accuracy of temperature measurements in turbulent jet diffusion flames by Coherent Anti-Stokes-Raman spectroscopy. *Combust. Sci. Tech.*, 175:1893–1914, 2003.

[98] M. E. Mueller and H. Pitsch. LES model for sooting turbulent nonpremixed flames. *Combust. Flame*, In Press., 2012.

[99] C. M. Kaul, V. Raman, G. Balarac, and H. Pitsch. Numerical errors in the computation of subfilter scalar variance in large eddy simulations. *Physics of Fluids*, 21:055102, 2009.

[100] C. M. Kaul and V. Raman. A posteriori analysis of numerical errors in subfilter scalar variance modeling for large eddy simulation. *Physics of Fluids*, 23:035102, 2011.

List of Publications

2009

G. Blanquart, M. E. Mueller, and H. Pitsch, Modeling and Analysis of the Effects of Temperature on Soot Formation using a Joint Volume-Surface-Hydrogen Model, Comb. Flame, 156:1614–1626, 2009.

G. Blanquart, P. Pepiot-Desjardins, and H. Pitsch, Chemical Mechanism for High Temperature Combustion of Engine Relevant Fuels with Emphasis on Soot Precursors, Comb. Flame, 156:588–607, 2009.

M. E. Mueller, G. Blanquart, and H. Pitsch, Hybrid Method of Moments for Modeling Soot Formation and Growth, Comb. Flame, 156:1143–1155, 2009.

M. E. Mueller, G. Blanquart, and H. Pitsch, A Joint Volume-Surface Model of Soot Aggregation with the Method of Moments, Proc. Comb. Inst., 32:785–792, 2009.

V. Raman, M. E. Mueller, G. Blanquart, and H. Pitsch, LES/PDF modeling of soot evolution in turbulent flames, 62nd Annual Meeting of the American Physical Society Division of Fluid Dynamics, Minneapolis, MN, November 22–24, 2009.

2010

J. Wang, D. Domin, B. Austin, D. Zubarev, J. McClean, M. Frenklach, T. Cui, and W. A. Lester, Jr., A Diffusion Monte Carlo Study of the O-H Bond Dissociation of Phenol, J. Phys. Chem. A 114:9832–9835, 2010.

D. Y. Zubarev, N. Robertson, D. Domin, J. McClean, J. Wang, Jr. Lester, W. A., R. Whitesides, X. You, and M. Frenklach, Local electronic structure and stability of pentacene oxyradicals, J. Phys. Chem. C, 114:5429-5437, 2010.

M. E. Mueller and H. Pitsch, LES Subfilter Modeling of Soot–Turbulence Interactions, 63rd Annual Meeting of the American Physical Society Division of Fluid Dynamics, Long Beach, CA, November 21–23, 2010.

2011

F. Bisetti, G. Blanquart, M. E. Mueller, and H. Pitsch, On the formation and early evolution of soot in turbulent nonpremixed flames. Combust. Flame, In Press, 2011.

M. E. Mueller, G. Blanquart, and H. Pitsch, Modeling the Oxidation-induced Fragmentation of Soot Aggregates in Laminar Flames. Proc. Combust. Inst., 33:667-674, 2011.

X.Q. You, R. Whitesides, D. Zubarev, Jr. Lester W. A., and M. Frenklach, Bay-capping reactions: Kinetics and influence on graphene-edge growth, Proc. Combust. Inst., 33:685–692, 2011.

D. Y. Zubarev, X. You, J. McClean, Jr. Lester, W. A., and M. Frenklach, Patterns of local aromaticity in graphene oxyradicals, J. Mater. Chem., 21:3404-3409, 2011.

2012

D. Y. Zubarev, X. You, J. McClean, Jr. Lester, W. A., and M. Frenklach, Delocalization effects in pristine and oxidized graphene substrates. In *Advances in the Theory of Quantum Systems in Chemistry and Physics* (P. E. Hoggan, E. J. Bröndas, J. Maruani, P. Piecuch, and G. Delgado-Barrio, Eds.), pages 553–569. Springer, Dordrecht, 2012.

P. Donde, V. Raman, M. E. Mueller, and H. Pitsch, LES/PDF modeling of soot evolution in turbulent flames, Submitted to the Proceedings of the Combustion Institute as part of the 34th Combustion Symposium.

M. E. Mueller and H. Pitsch, LES model for sooting turbulent nonpremixed flames, Combustion and Flame, In Press, 2012.